THÈSE DE DOCTORAT
DE L'UNIVERSITÉ DE LILLE

LABORATOIRE DE MÉCANIQUE, MULTIPHYSIQUE ET MULTIÉCHELLE (UMR9013, CNRS)

Présentée par

XI CHEN

pour l'obtention du grade de

DOCTEUR DE L'UNIVERSITÉ DE LILLE

Domaine

MENTION GÉNIE CIVIL

Sujet de la thèse

Etude expérimentale du comportement poromécanique des argilites du Cox: Influences de l'anisotropie initiale et du chemin de chargement

(Experimental investigation of poromechanical behaviour of Cox claystone: Influences of initial anisotropy and loading path)

Soutenue le 11 décembre 2020 devant le jury composé de :

Farimah MASROURI, Professeur	Université de Lorraine	*Présidente*
Yujun CUI, Professeur	École des Ponts ParisTECH,	*Rapporteur*
Dragan GRGIC, MCF HDR	Université de Lorraine	*Rapporteur*
Gilles ARMAND, Docteur	Andra	*Examinateur*
Nathalie CONIL, Docteur	INERIS	*Examinateur*
Jianfu SHAO, Professeur	Université de Lille	*Examinateur*
Nicolas BURLION, Professeur	Université de Lille	*Directeur de thesé*

LAMCUBE - L'UNIVERSITÉ DE LILLE

Abstract

The Callovo-Oxfordian (COx) claystone has been selected as a potential host rock for underground radioactive waste repository in France. The present thesis is devoted to experimental investigation of the poro-mechanical behavior of COx claystone. The emphasis is put on the study of influences of structural anisotropy and loading path. Both instantaneous and time dependent behaviors are considered. For this purpose, a series of laboratory investigations including axial extension creep tests with different loading orientations, shear creep tests on fractured samples with gas permeability evolution measurement, tests for determination of Biot's and Skempton's coefficients, lateral decompression and axial extension tests with poroplastic cycles and oedometric tests under different drainage conditions. From the results obtained, it is found that the poromechanical behavior of COx claystone is strongly affected by structural anisotropy, loading path and water saturation degree. The time-dependent deformation is also an important property of the COx claystone. The gas permeability evolution of fractured samples is influenced by various factors including confining pressure and self-sealing ability of clayey rock.

Résumé

L'argilite du Callovo-Oxfordian (COx), est sélectionnée comme une potentielle barrière géologique pour le stockage profond des déchets radioactifs en France. La présente thèse de doctorat est consacrée à l'étude expérimentale du comportement poromécanique de cette roche. Au complément aux études antérieures, l'accent est mis sur l'étude des influences de l'anisotropie initiale et du chemin de chargement. Pour cet objectif, une série de tests en laboratoire sont réalisés, incluant des essais de fluage en extension axiale avec différentes orientations de chargement, des essais de fluage au cisaillement sur échantillons fracturés avec mesure de perméabilité au gaz, des tests de détermination des coefficients de Biot's et de Skempton, des essais de décompression latérale et d'extension axiale avec des cycles poroplastiques, et des essais oedométriques avec différentes conditions de drainage. D'après les résultats obtenus, il est observé que le comportement poromécanique de l'argilite du COx est fortement influencé par l'anisotropie structurale et le chemin de chargement. La déformation différée est une propriété importante de cette roche argileuse et elle est également influencée par l'anisotropie structurale et le chemin de chargement. L'évolution de la perméabilité au gaz des échantillons fracturés au cisaillement est affectée par de multiples facteurs comme la pression de confinement et la capacité d'auto-colmatage de la roche.

Acknowledgement

Finally, my favorite part arrives. The reason why I love this part is not only it means the end of my doctoral study, but also for my entire thesis, it is the only part which would not be severely criticized, deleted or altered, on the contrary, it's full of sincere gratitude, peace and love. As I types these words, I sincerely wish all these people I love could be as happy as me at this moment, for all future days.

I would like to thank the members of jury: Mister Rapporteurs: Yujun CUI and Dragan GRGIC, Mister Examiners: Filles ARMAND, Nathalie CONIL, Farimah MASROURI, Jianfu SHAO and my supervisor Nicolas BURLION to participate in the ceremony of my thesis defense as one most important moment in my life. It means a lot for me.

I would like to express the depth of my gratitude to Professor Jianfu SHAO for giving the opportunity to me to continue my doctoral study in France. From your patient guidance, I feel the greatest talents of a scientific researcher as well as the gentleness and elegance of an elder, I wish you good health, and that everything goes smoothly. I would like to express my thanks to Dr.Shouyi XIE, a gentle and knowledgeable teacher. Without your help and guidance in the past three years, I would not be able to successfully complete my thesis. Also, I have learned the optimism and perseverance when facing setbacks from you. I believe these qualities will accompany me throughout my whole life. I would like to express my gratitude to Professor Wei WANG. Nine years ago I first met you and six years ago I became your student. Your serious academic attitude guide me to forge ahead and your gentle and sincere lifestyle leads me step forward. How lucky I am as I have learned too much from you.

I would like to thank Professor Zaobao LIU. You are a serious and responsible guider. As my academic experience grows, I feel your excellence and kindness extremely deeper. I would like to thank Wang ZHANG for supporting in three years. Actually, I am disgusted with the coincidence of my life and work, but you seem to be an exception. You are not only my work partner, but also integrated into my life and become my lifelong fiend, I really like your rare and sincere youthfulness and hope you will always be so interesting. I wish you and Xiu LIU to have a smooth graduation as well as a lifetime of happiness. We will surely meet at somewhere in the world, all encounters are reunions after a long separation.

I would like to thank my relatives, thank my aunt Hong WANG, you have helped me

too much, materially and spiritually, since I was a child you are my idol, and I have been cherishing the goal of becoming such a gorgeous person like you and I wish someday I would. Thank my grandmother Tingmei LIU, I want to turn all my feelings from my hometown into yellow leaves flying for you and I can't wait to return back to you and never leave again, I have nothing to ask for you just hope you can live a long and healthy life, and remember me. Thank my father Bin CHEN, I write these words with guilt, I want to say "I love you. " You don't often hear these words, but you still don't stop loving me in your way. Finally, I want to dedicate all the most beautiful words I can think to my mother Ping WANG, the poem and the moon in my heart. You always worry that your son, as a homosexual, would face the dusk of life alone forever, but death is not terrible, forgetting is. Therefore, I imprint my emotions at this moment, even if hundreds of years pass, the people we love are gone and the things we cherish are turned into dust, people who see this paper will still know how much I love you.

I would like to thank Zhenyu YANG and Yixi ZHANG. You are my best friends and I am grateful for every minute of acquaintance with you as the feelings are just like fireworks in the New Year. I am incredibly happy that my friend Zhenyu Yang has got married one months ago. The hour for watching your ceremony live is one of my happiest moments in 2020. For this lovely lady, although I have never met you, but I think you must be an equally interesting and kind person. May the joy you share on your wedding day be the kind you'll share all along life's way; for Yixi ZHANG, we had many quarrels and more joys, but in the end I remember countless memories in a few words as I know that you are destined to be one of the most important parts of my life, you are just like a meteor in the night sky.

I would like to thank Xinyu LAN, my only friend in high school. We shared the moving light and shadow life for countless nights as well as intertwined a chain of images that spans time and space. I am so grateful for our thirteen years friendship. I would like to thank Jian OU, my undergraduate and postgraduate roommate. I really miss the laughing days with you so much. I knew you earlier than our friendship started, but I didn't realize how precious you are at that time. I would like to thank Tao NI and Rui ZHU, you showed me how such precious love happened on two people who are so bright as pearls, Choosing to be roommates with Ni Tao in 2017 summer was the best decision I made that year. I would like to thank Yiming CAI, For the nights of the summer end that we spent with, and the happy hours spent in Nanking, Nanchang, Rome, Florence, Helsinki and Stockholm.

I would like to thank Zhou HE, Shuhan SUN and Yuxin XIE, we have quite different personalities, but we also move forward together. We shared the pain and glory in the past life river and I also wish each of you a happy life in future days. For Mr.Yuxin XIE, who is the first one of us to get married. I wish you a world of happiness and love as all your dreams come true.

And for Gang SONG, the only close friend I know as a non-student, you are a rare friend, with gentleness and gorgeousness, you treat everyone in your life sincerely and repay the greatest kindness. You rarely hear my praise, but I must frankly say that I have been very happy for the four past years, and sometimes I really think, it's also a great thing if you can be my elder brother. Of course, I'm full of happiness and gratitude just for meeting you. As you (or Hirokazu Koreeda) said, I'm only 27 years old and I can be whoever I want to be. So I wrote this trip here as a commemoration, wishing that our friendship can continue forever, and sincerely hope that this is not your closest to science.

Thank this beautiful city Lille and its kind citizens. I will miss this place. Thank Yudan JIN, Meng WANG, Yue SUN, Zhan YU, Hailing SHI, Dongmei ZHANG, Jueliang CHEN, Siyu LIU, Liping ZHU, Yutian Ke, Wei XIE and Jianjian ZHAO. I have prepared to experience three lonely years, but I still met you all.

Thank Yifan CHEN, Liyu CHEN, Yuning ZOU, Yugan CHENG, Heqing HUANG, Lei YAN, Jing Ai, Yuwen FU, Lang GAO, Qi HU, Jinqiao CHEN, Zhulin WU, Minhui JI, Yue GU, Haonan HU, Mengyang WANG, Pengxuan XU, Shenjie LUO, Fuwan DING, Shuang SUN and Torovandarko with TOROSCOPE. The sea is not deep, missing someone is deeper than the sea.

Finally, I want to send my deepest gratitude to Mr.Xi CHEN. The successful completion of the thesis is inseparable from your efforts. You have seen those anxious and confused foggy tossing and turning, and also known the dark nights with tears. But you are also a lucky man. You are filled with love for the past twenty-seven years. The misery and discord in life have never bothered you, and the discrimination and difficulties have bypassed you. I wish you to keep this luck and love in your future life, and you can be as brilliant enough to make good use of these qualities for everyone belongs to your world.

Here comes to the end. All stories, even the ones we love, eventually come to an end.

Xi CHEN
06/11/2020

Contents

List of Figures

List of Tables

Chapter I

General Introduction

Clayey rocks are widely studied around the world in petroleum engineering, underground waste storage and mining science. For example, shale rock is usually served as the cap rock in petroleum and mining engineering, and to act as the hosted reservoir rock for shale gas development. In underground radioactive waste disposal, claystone also serves as a privilege candidate host rock for geological radioactive waste repository in many countries, in particular in France, due to its low permeability, relatively high mechanical strength and self-sealing ability. Further, swelling clay also works as an engineering material together with the waste canister to constraint the radioactive wastes in the buffer especially in the French concept.

The mechanical and physical properties of clayey rocks are complex, exhibiting initial anisotropy, strong pressure sensitivity, plastic deformation and induced damage, as well as creep deformation. They are also affected by porosity and mineralogical compositions such as clay particles, quartz, calcite etc. Therefore, it is primordial to perform a comprehensive investigation of the physical and mechanical properties of clayey rocks. For the recent decades, a series of research projects has been conducted by the French Agence National de Gestion des Dechets Radioactifs (Andra) including both experimental investigations and constitutive modeling of the Callovo-Oxfordian (COx) claystone. In addition, a large new research program is being carried out since 2016 for the operational phase of the French underground radioactive waste project. The experimental work presented in this thesis is a part of this program and the present study contributes to the series of experimental investigations of the physical and mechanical properties of the Callovo-Oxfordian stratum of MHM (Meuse/Haute-Marne) site in Eastern France.

In Chapter II , we shall first present a short summary of previous studied devoted to the characterization of mechanical behaviors of the COx claystone. The previous re-

sults have outlined some basic features of COx claystone mechanical behaviors. However, some complementary studies are still necessary, in particular on the influences of initial anisotropy and loading path on the instantaneous and time-dependent behaviors as well as on the poroelastic and poroplastic properties. The present study provides some complementary contributions to those previous works by performing a series of new laboratory tests.

More precisely, most previous laboratory tests were performed by using conventional triaxial compression (CTC) path. Very few results are available on gas permeability evolution in fractured samples. Important scatters were observed in existing results on poroelastic properties and in particular Biot's coefficient. Poroplastic behavior was so far rarely investigated. In this study, we shall complete laboratory tests with new loading paths, for instance axial extension and lateral decompression with constant mean stress. Different loading cycles will be used for the measurement of Biot's and Skempton's coefficients. Gas permeability evolution will be investigated in samples containing an initial fracture created by a direct shear test. Further, the effect of pore pressure on plastic or strength criteria will also be investigated. These new experimental studies are organized in three Chapters.

In Chapter III , a series of creep tests are performed under axial extension with constant mean stress. This loading path corresponds well to stress evolution around underground cavities due to excavation. In such tests, samples are first subjected to a hydrostatic stress state. The axial stress is then reduced while the confining pressure is increased to maintain a constant mean stress. Variations with time of creep strains are measured at different levels of deviatoric stress. In addition, in order to investigate influences of initial anisotropy on creep deformation, these tests are performed on samples with five different loading angles with respect to bedding planes of the COx claystone (0^o, 30^o, 45^o, 60^o and 90^o). The experimental results are analyzed and discussed in terms of loading orientation and stress level.

In Chapter IV , the gas permeability evolution in fractured samples is investigated. With the help of a specific device, direct shear tests are carried out during the first stage to create longitudinal fractures in cylinder samples under different values of confining pressure. The fractured samples are then subjected to different levels of prescribed shear stress during the creep stage. Variations of creep strains and gas permeability with time are measured at each step of creep. The emphasis is here put on the gas permeability evolution. The obtained results are discussed in terms of influences of creep deformation and confining pressure, as well as the self-sealing ability of fractures.

In ChapterV , we shall investigate poromechanical coupling properties of COx claystone. For this purpose, three groups of new tests are performed. In the first group, different loading paths are considered for the measuring of Biot's coefficient, which controls the poroelastic coupling. The emphasis is put on the effect of loading and unloading on the measured Biot's coefficient. In the second group, specific poroplastic coupling tests are carried out. The objective here is to verify the existence and validity of effective stress concept in plastic domain for the saturated COx claystone. In the third group, oedometric tests under different drainage conditions are realized with measurement of pore pressure evolution. This type of tests is useful for the validation of constitutive models for saturated rocks.

Finally, some general conclusions are formulated in Chapter VI , based on the main findings of the present study. Also, some perspectives on future works are given in relation with the pending issues raised throughout the present research.

Chapter II

State of Art

1 Introduction

Callovo-oxfordian (COx) claystone has low permeability properties, absence of major fractures, and high mechanical strength, and has been selected as an ideal candidate host rock in many areas worldwide, especially in France in the framework of the underground research laboratory CIGEO(ANDRA, 2005).In this chapter, we provide a short introduction regarding the motivation behind undertaking research on the mechanical behavior of COx claystone. The second part of the chapter presents a literature review on experimental tests observed with COx claystone. Finally, we introduce a brief bibliographic review of these research results.

2 Motivation

Many studies regarding deep geological radioactive waste repositories have been undertaken worldwide. Many countries (e.g., France, Switzerland, Belgium, Sweden, Canada, and Japan) consider deep geological repositories as the disposal solution for long-term radioactive waste.

In France, COx claystone has been selected as the candidate host rock for the potential repository with the French National Agency for Radioactive Waste Management (ANDRA) in charge of this project. A rock formation at approximately 500 m depth is located near Bure (FigureII .1). The claystone has chemical retaining properties towing to its clay particles, which provide a chemically stable environment with an extremely low permeability that limits the transport of radionuclides dissolved in water. High temperatures around the exothermic waste packages are avoided due to the specific design

of the repository and by the cooling phase of the waste before storing it. Furthermore, the COx claystone mechanically provides enough stability for the construction of galleries. The rock has a self-sealing ability, through which fractures, induced during excavation, partially close themselves over time. These aspects demonstrate that the COx claystone fulfills the requirements of a natural barrier.

COx claystone would be a sound barrier for long-term radioactive waste disposal (ANDRA, 2005), owing to the following abilities:

(1) Protect wastes from natural erosion and human activities at a safe location.

(2) Limit the diffusion of radionuclides emitted from the wastes.

(3) Keep these properties for long timescales by withstanding thermo-chemo-mechanical exposure, even after the concrete and metal components have deteriorated.

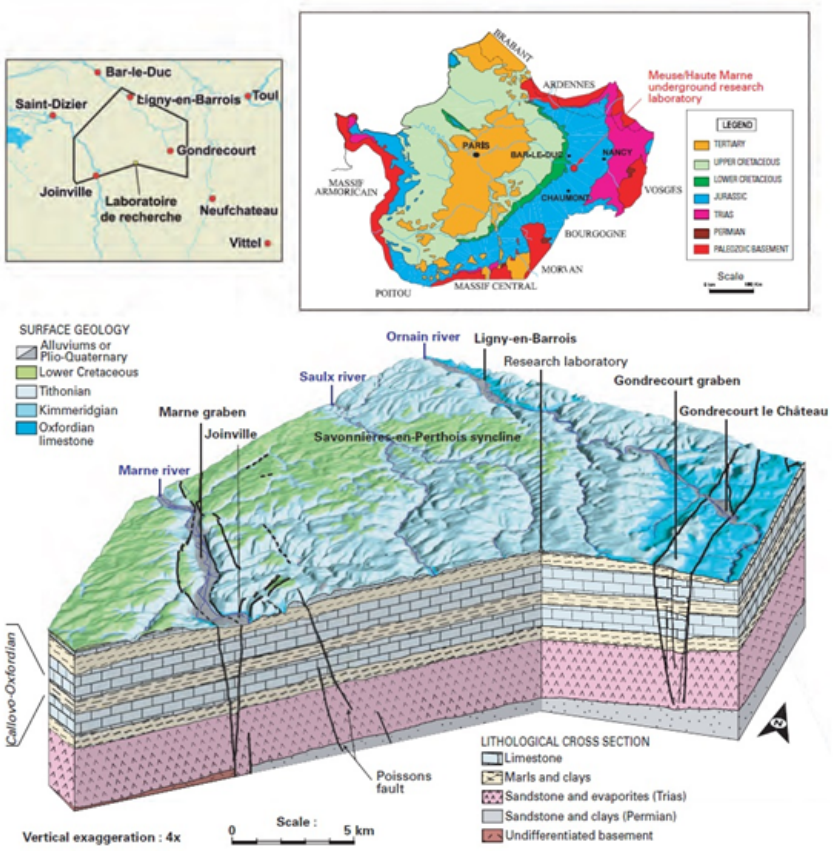

Figure II .1: Geological map of the Meuse/Haute-Marne area in eastern France, where the Callovo-Oxfordian claystone is located in a layer at around 500 m depth. The Andra underground research laboratory is found near the village of Bure (ANDRA, 2005)

The mechanical and physical properties of COx claystone are complex, exhibiting ini-

tial anisotropy, strong pressure sensitivity, plastic deformation and induced damage, and creep deformation. COx claystone is also affected by porosity and mineralogical compositions, including clay particles, quartz, and calcite. Therefore, it is crucial to perform a comprehensive investigation of the physical and mechanical properties of clayey rocks. The next section presents a summary of previous studies examining the characterization of the mechanical properties of COx claystone.

3 Mechanical properties of COx claystone

The underground research laboratory URL is located approximately 490 m deep, where the high clay fraction ranges from 40% to 60% (Armand et al., 2017b). At this level, the total vertical stress is 12.7MPa, the major horizontal stress is 14-16MPa, and the minor horizontal stress is 12.4MPa, the pore pressure is 4.5MPa, and the mean Terzaghi effective stress is 8.2-9.2MPa(Conil et al., 2012; Wileveau et al., 2007a).

These previous long-term experimental studies included various testing methods, such as uniaxial, triaxial, oedometric compression, hydrostatic, three-point, double torsion, indentation, mini-compression, micro-indentation, triaxial extension, decompression, and creep tests, and from these the primary mechanical behaviors were obtained. The mechanical properties of COx claystone are sensitive to mineral composition (including microcracks, and microstructural anisotropy), temperature, loading history, water-saturated degree, and time. This section includes an overview of the mechanical behaviors obtained from previous studies.

3.1 Basic mechanical behavior

3.1.1 Mineralogy and micro structure

Many studies have examined the basic mechanical behaviors of COx claystone microstructure. (Robinet, 2008) found that at the megascopic scale, the COx claystone was mainly composed of clay minerals, carbonate, and quartz grains. The average proportion of each constituent phase was approximately 40% (± 15%) quartz, 34% calcite and 26% clay minerals. However, the mineralogical compositions significantly varied with the depth. The clay phase composition($<2\mu$m) included 40% illite, 30% kaolinite, 5% chlorite, and 25% swelling minerals (such as smaltite and interstratified). The mineral composition of the clayey rock was measured using the X-ray diffraction technique (FigureII .2 and FigureII .3 (Robinet, 2008).).

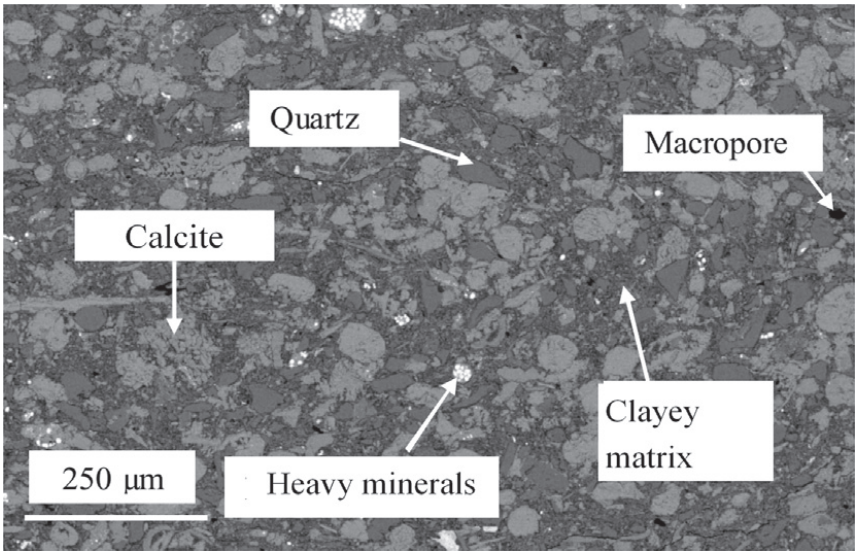

Figure II .2: Mineral composition of the COx argillite by SEM image. Picture from(Robinet, 2008)

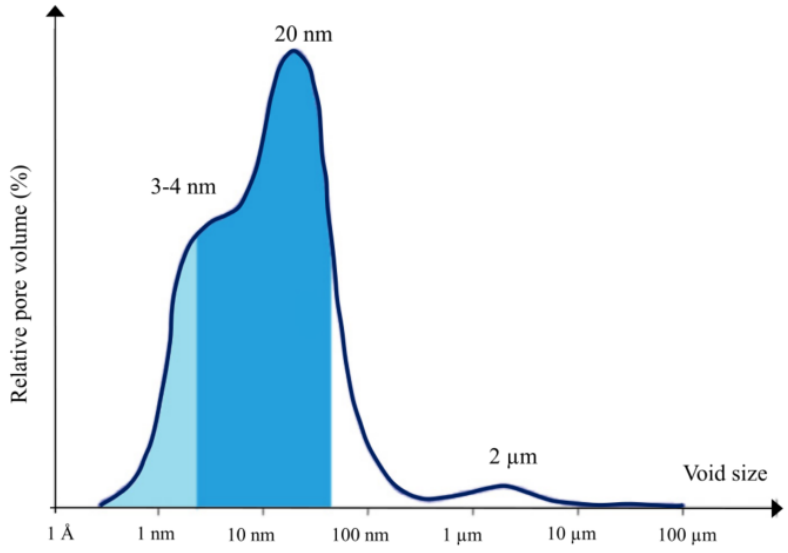

Figure II .3: Pore size distribution of the COx argillite. Data from(Robinet, 2008)

The smectite fraction is responsible for the swelling capacity of claystone(Delage et al., 2014; Mohajerani et al., 2011) and the self-sealing phenomenon (Auvray et al., 2015b; Davy et al., 2007; De La Vaissière et al., 2017; Menaceur et al., 2015; Zhang, 2013). Most of the porosity was located within the clay matrix(Robinet et al., 2015), with porosity estimates from 14 to 20%, with 18% at the URL level(Yven et al., 2007). The natural water content

was estimated with values between 5 to 8% (Armand et al., 2017b), with 8±1.2% at URL level(Giot et al., 2018).

(Chiarelli et al., 2001) applied uniaxial and triaxial compression tests to investigate the influence of mineralogy and moisture content on the mechanical behavior. The results showed that the claystone behavior became more brittle when the calcite content increased or when the clay or moisture content decreased. The influence of mineralogy on the mechanical response was less important than that of moisture content.

The structure anisotropy was measured using creep test(Liu et al., 2015b; Shi et al., 2020), unconfined compression test(Homand, 2000), odemetric test(Escoffier, 2002; Vincké et al., 1998) and gas permeability test(Harrington et al., 2017; Liu et al., 2016; Menaceur et al., 2015) considering samples drilled in parallel and perpendicular directions to the bedding planes. For these tests, COx claystone showed obvious anisotropy characteristics on strength and deformation. The test results showed that more directions such as 30°,45° and 60° could be investigated.

3.1.2 Saturation

For underground radioactive waste storage, the mechanical behavior of initially saturated COx claystone is sensitive to the water content. Studies regarding other rock types have verified that when the water content increases, the failure stress and the initial elastic modulus decreases. For COx claystone, previous studies have shown that the water content effect was related to modifying the microstructure(Bornert et al., 2010; Homand et al., 2006). In addition, the failure properties of COx claystone are influenced by the degree of saturation(Shao et al., 2005; Yang et al., 2010; Zhang and Rothfuchs, 2004). At the micro-scale, the drying-wetting cycle could change the distance between the inner clay platelets, leading to a change in the mechanical characteristics of the COx claystone(Robinet, 2008). The clay matrix plastic deformation with micro-crack and interface growth is the main deformation mechanism behavior of COx claystone(Chiarelli et al., 2003; Guéry et al., 2008).

(Zhang et al., 2012) performed micro-indentation and mini-compression tests to study the mechanical properties of COx claystone with different relative humidities. The results showed that as the relative humidity increased, the failure strength and elastic modulus decreased. For the desaturation and resaturation processes, the suction acted as an essential part because of pore sizes, generating an overall confining effect and compaction or swelling of the bedding planes.

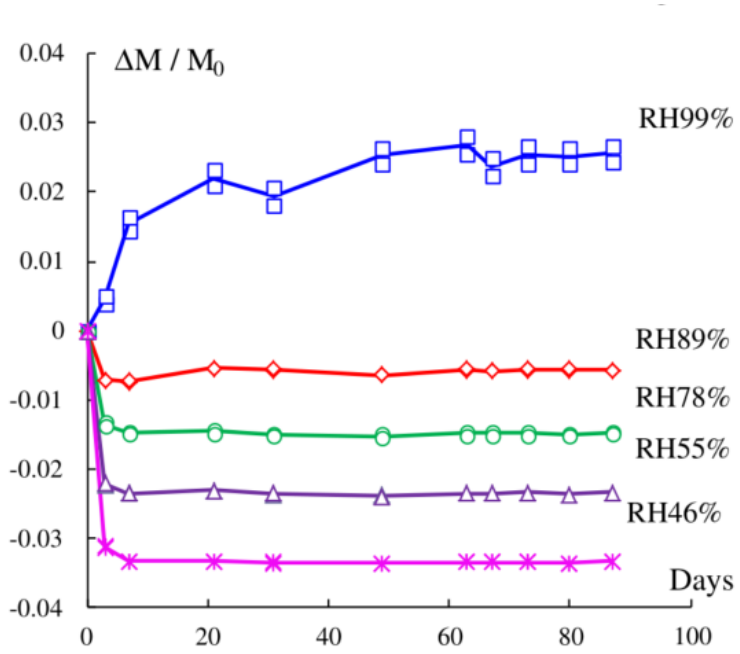

Figure II .4: Relative variation of total sample mass during resaturation and desaturation process at the room temperature(Zhang et al., 2012)

Based on the results obtained by (Zhang et al., 2012), in (Hu et al., 2014) investigated the influence of the water content and mineralogical composition on the mechanical behavior of the COx claystone with micro-indentation and mini-compression tests from samples drilled at three depths where the COx claystone formations had different mineralogical compositions. The results showed that the presence of the clay minerals increased the overall deformability of the COx claystone because of the plastic deformation of the clay matrix. The mechanical behavior became more brittle because the calcite and quartz content increased as the overall mechanical strength increased.

3.1.3 Temperature

This radioactive waste disposal barrier is heat-emitting, with the temperature inside the structure increasing to 100°C, which increases the density of the micro-cracks in COx claystone. Therefore, it is necessary to study the influence of temperature on the mechanical behavior of COx claystone.

The study by (Masri et al., 2014) showed that the thermal effect greatly influenced the mechanical properties of COx claystone. The increased temperature induced pore pressure for saturated COx claystone under undrained conditions(Mohajerani et al., 2012; Zhang

et al., 2017), with TER and TED tests showing important thermal pressurization in COx claystone formations (Armand et al., 2017a; Conil, 2012; Wileveau et al., 2007b).

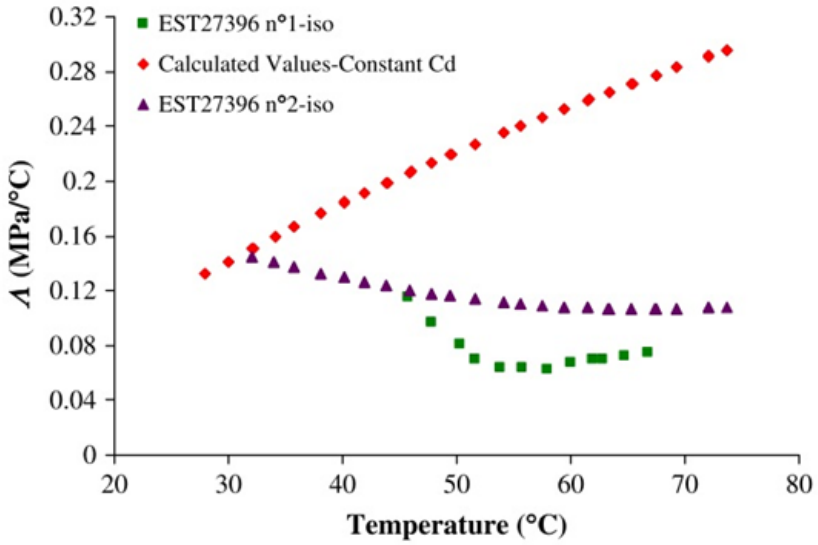

Figure II .5: Thermal pressurization coefficient: experimental values and calculated values, assuming a constant drained compressibility(Mohajerani et al., 2012)

(Blaise et al., 2014) showed the thermoplastic contraction starting at 48°C corresponded with the maximum burial temperature of the COx claystone of approximately 50°C. The drained volumetric thermoelastic expansion coefficient was determined as $0.48\times10^{-4o}C^{-1}$. Using a hollow cylinder device, (Mohajerani et al., 2014) obtained an elastic drained expansion prior to the plastic contraction of heated COx claystone and a drained thermal expansion coefficient of $0.43\times10^{-4o}C^{-1}$ was obtained from mechanical compression cycles. (Menaceur et al., 2015) sheared saturated samples under elevated temperatures of 80°C and showed that temperature had only a slight effect on mechanical behavior.

The study by (Mohajerani et al., 2012) on the thermal behavior under undrained conditions investigated two COx claystone samples in an isotropic cell. Based on this previous study, (Zhang et al., 2014a) proposed a series of triaxial compression, mini-compression, and micro-indentation tests on COx claystone under temperature-controlled conditions. The results showed that the mechanical behavior of COx claystone was affected by the temperature and relative humidity coupling, and their combined effects.

Based on the theoretical analysis of stress evolution under surrounding rocks in an underground cavity zoom during excavation, (Liu et al., 2019a) proposed a series of lateral decompression tests to investigate the mechanical behavior of COx claystone at different

temperatures from 20 to 90°C. The results showed that the temperature increase induced shear strength degradation in COx claystone. A natural logarithm function was found to provide a better fit for the degradation of shear strength with temperature increase.

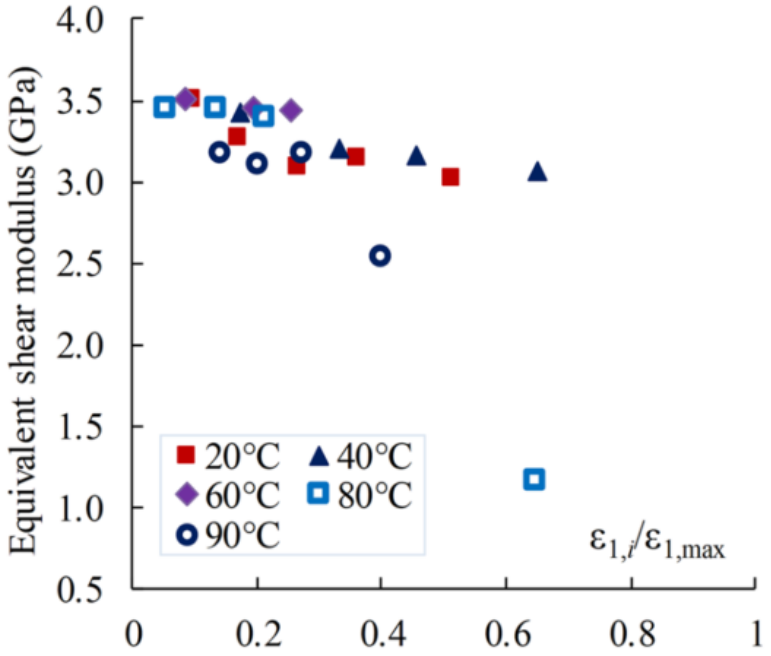

Figure II .6: variation of equivalent shear modulus during LD tests under different temperatures(Liu et al., 2019a)

3.1.4 Long-term dependent properties

Many instantaneous experimental studies have been undertaken to examine the short-term behavior of COx claystone, and several studies have looked at the time-dependent mechanical behaviors. Creep deformation is commonly observed in geological materials. As a long-term radioactive waste disposal barrier material, a description of the time-dependent behavior of COx claystone is important for long-term stability analysis. Previous tests have attempted to characterize the deformation and some generally realized for a relatively long period under other controlled environmental conditions, for example, under different temperatures and moisture content.

(Bérest, 1987) stated that if the deviatoric stress was smaller than 6MPa in the conventional compression test, there existed no obvious plastic strain. (Vales et al., 2002) proposed five indentation tests on pure COx claystone, which proved that when this rock was submitted to large deviatoric stresses (e.g., 10MPa), it would exhibit a $3\times10^{-11}s^{-1}$ to

$3\times10^{-10}s^{-1}$ of the creep strain rates. (Bérest et al., 2001) proved that when the stress was lower than 3MPa for COx claystone, the creep strain was not obvious. In contrast, (Zhang and Rothfuchs, 2007) showed that the creep capacity was significant for COx claystone under low stress. The effect of temperature and the degree of saturation for this type of rock should not be ignored. For instance, (Gasc-Barbier et al., 2004) undertook a series of creep tests involving the parameters such as diameter of the indenter, temperature, deviatoric stress and the results showed that for the 2 months creep process, the creep rate and stress had a linear relationship. This study showed that the deformation of COx claystone was sensitive to the loading degree, water-saturated degree, and temperature. Using multi-stage creep tests, (Fabre and Pellet, 2006; Yang et al., 2011) found a threshold as the deviatoric stress increased.

Based on the previous results for the creep characteristics of COx claystone, (Liu et al., 2015b) proposed a series of triaxial compressive creep tests to investigate the effects of the deviatoric stress level and structural anisotropy with the same confining pressure. The tests results showed that with the increase of deviatoric stress, the strain was enhanced, and the creep rate analysis showed the same trend as the definitive conclusions. The experimental study also showed that COx claystone was strengthened by the one-step creep test.

(Liu et al., 2018a) investigated the relative humidity effects on creep deformation with three different relative humidities (59%, 85% and 98%) under the same confining pressure. Claystone samples with different mineralogical compositions drilled from different geological units were investigated and triaxial creep tests were performed with different confining pressure under the same relative humidity. The results showed that the creep strain and rate value were enhanced by increased relative humidity and confining pressure. The clay minerals, especially smectite, played an essential role in creep deformation and increased creep strain.

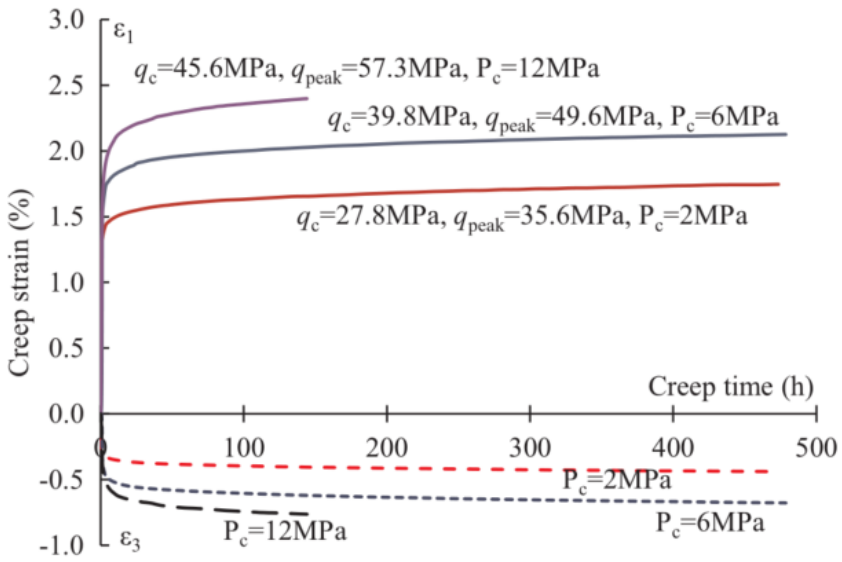

Figure II .7: Creep strains of claystone from EST44300 under three confining pressures at stress level q_c/q_{peak} =80%(Liu et al., 2018a)

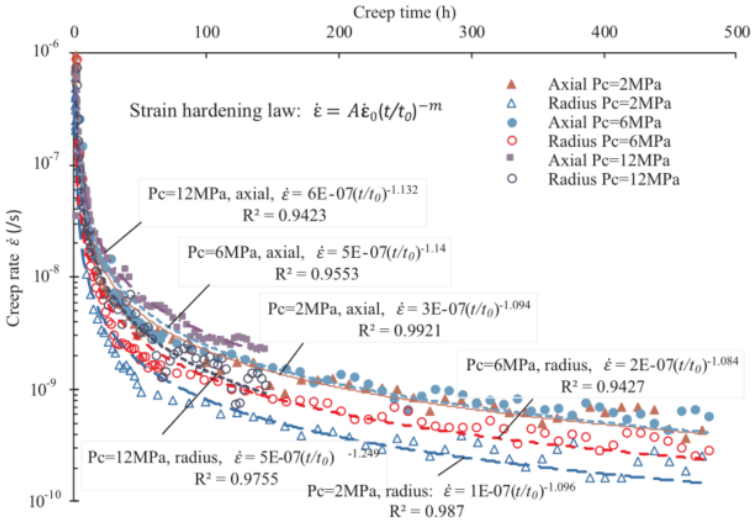

Figure II .8: Strain rate of claystone subjected to q_c/q_{peak} = 80% under different confining pressure(Liu et al., 2018a)

In the study by (Shi et al., 2020), the digital volume correlation was applied to X-ray micro-tomography images for the creep tests on COx claystone under different deviatoric stress levels to investigate the deformation relationship with the stress level and different directions to the loading orientations to examine the structural anisotropy. Digital vol-

ume correlation was also applied to compute the strain fields and global average strains for the tested samples. Because of the heterogeneous characteristics of COx claystone, the distributions of the creep strains were extremely non-uniform as there existed strain concentration zones inside the samples. At the mesoscopic scale, the anisotropy was an important part of the deformation and failure processes of this material.

3.1.5 Loading path

For the majority of previous studies, the loading path is under constant confining pressure loading that causes the mean stress to change. However, during the excavation process, with the removal of the cavity rock, the lateral stress is decreased and the axial stress is increased. For the entire process, the generalized shear stress is increased and the mean stress remains unchanged. For laboratory research, the lateral decompression test and the axial extension test better reflect the actual excavation process (FigureII .9), which has not been fully investigated in COx claystone.

(Liu et al., 2019a) proposed a series of lateral decompression tests to investigate the mechanical behavior compared with the constant confining pressure tests, and showed that the failure was characterized by the creation of a localized macro-crack and a damaged zone with many micro-cracks around the macro-crack compared with the constant confining pressure test. The natural logarithm function provided a better fit for the degradation of shear strength with the temperature increase.

COx claystone tests with axial extension loading path have not been fully investigated to date. Therefore, further studies are required to investigate more tests under different loading paths.

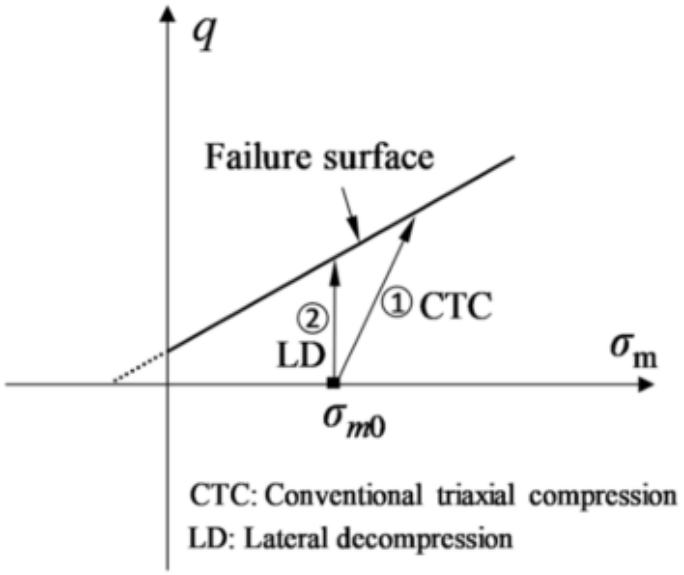

Figure II .9: Loading path of consitant confining pressure and lateral decompression test on meridian plane(Liu et al., 2019a)

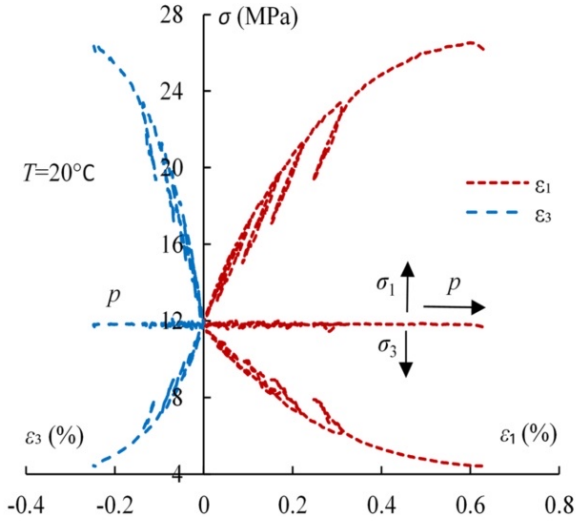

Figure II .10: Experimental results of lateral decompression test(Liu et al., 2019a)

3.2 Poromechenical behavior

The engineering structures of the radioactive waste disposal barrier build on saturated soil and rock; therefore, the inner pores are always filled with several fluid phases such as water. COx claystone is commonly taken as the sealed bulkhead layer whereby the water saturation degree can induce a capillary effect and contribute to the modification of the microstructure. Therefore, it is necessary to research the poromechanical behavior of COx claystone.

3.2.1 Elastic characteristic

Many previous studies on the elastic poromechanical behavior of porous material have focused on Biot's elastic coefficient. Studies by (Escoffier, 2002) and (Homand et al., 2006) determined that Biot's coefficient was between 0.55 and 0.95. (Homand et al., 2004) used the pulse-test and mass variation and measured Biot's coefficient as 0.75. Based on previous studies, (Cariou et al., 2012) used drained uniaxial compression tests and triaxial change in pore pressure poromechanical measurement test to recalculate Biot's coefficient for COx claystone and was found to equal 1.

(Bemer et al., 2004) used water as the injected fluid to saturate COx claystone and proposed a series of tests to obtain Biot's coefficient for different directions, which was measured as 1 in the parallel direction to bedding and 0.9 in the perpendicular direction to bedding. (Yuan et al., 2017) proposed a complete poromechanical study for COx claystone to measure Biot's coefficient for samples under different relative humidities with a new technique using gas injection to avoid the difficulty of controlling the water. The results showed that Biot's coefficient was isotropic, and was equal or greater than 1 for partially saturated and dry samples.

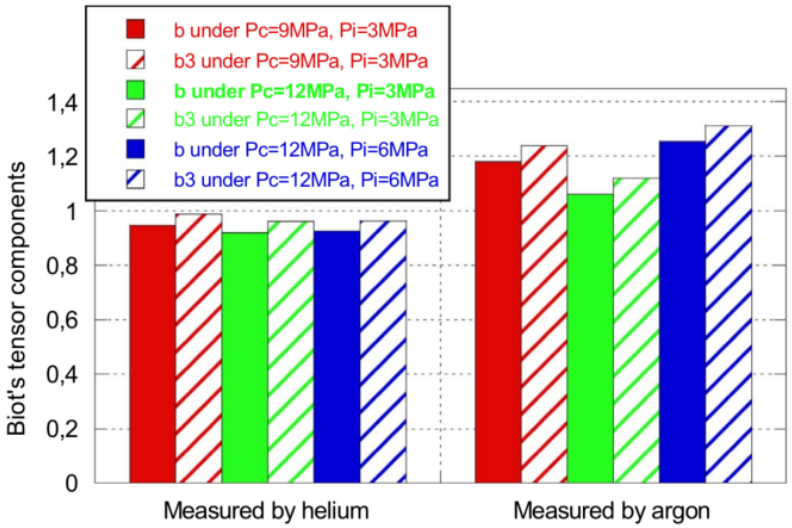

Figure II .11: Biot's tensor components of the sample from EST51446 'T cell' measured by helium and argon(Yuan et al., 2017)

Therefore, Biot's coefficient values obtained from previous experimental studies are dispersed, and it is hard to gain an accurate value because during the test process, each stage involves a time-consuming procedure and is hard to control. Thus, it is necessary to redetermine Biot's coefficient to better validate the effective stress concept for COx claystone, which is a part of the research undertaken in the present thesis.

3.2.2 Plastic characteristic

For the plastic domain, (Chiarelli, 2000) conducted many triaxial tests with saturated samples, under varying confining stresses. (Belmokhtar et al., 2018) proposed two drained triaxial tests for saturated samples that confirmed the loading rate. (Belmokhtar et al., 2017) measured the K_d on two samples tested at two different stress levels. (Mohajerani et al., 2011) examined three samples under the same stress states using loading-unloading cycles under undrained conditions to measure the undrained bulk modulus and Skempton coefficient. These authors found that the measured parameters were not the same for the inner sides of the samples.

(Escoffier, 2002) performed a series of oedometric tests on saturated conditions for different stress levels with 3MPa effective lateral stress. For the first nine tests, axial stress was changed under constant pore pressure. For the next nine tests, constant axial stress was maintained with a changing pore pressure. Then, nine groups of oedometric moduli and Biot's coefficient were obtained. Saturated samples with water vapor were

tested under different drainage conditions by (Bemer et al., 2004), who hypothesized that the unconfined samples swelled during resaturation. Using oedometric swelling tests, (Liu, 2016) found that the material swollen under vertical stresses was greater than the in situ stress.

For these tests, the basic poromechanical behavior of COx claystone was obtained; however, due to the uncertainty and discreteness of the tests with pore pressure, further studies are required. In this thesis, specific poroplastic coupling tests with poromechanical cycles and oedometric tests under different drainage conditions were proposed to investigate and verify the existence and validity of the effective stress concept in the plastic domain for saturated COx claystone.

3.3 Permeability evolution

It is important to study gas permeability evolution because large amounts of gas are produced during nuclear waste storage. The porosity and creep response of COx claystone is also revealed by gas permeability tests during creep tests. Gas permeability evolution is extremely sensitive in reflecting the deformation process in COx claystone creep tests and can be used as a good indicator of reflecting micro-cracks and inner pores changes under hydrostatic conditions and in triaxial tests (Billiotte et al., 2008; Zhang and Rothfuchs, 2008).

(De La Vaissière et al., 2017) obtained a mean permeability of $4.18\times10^{-}20m^2$ from 399 tests. For the URL, the value is $4.89\times10^{-}20m^2$. (Davy et al., 2007) obtained a lower permeability value as $10^{-}21m^2$ and the value measured by (Mohajerani et al., 2011) was $0.6\times10^{-}21m^2$, which was similar to the value measured by (Harrington et al., 2017). By comparing different measuring techniques, (Giot et al., 2018) obtained a constant permeability of $4.2\times10^{-}21m^2$ during steady state flow. With the basic value obtained, the gas permeability can be used as a parameter reflecting the change in the inner mechanism and the evolution of deformation for claystone.

Applying the gas permeability test with resaturated and desaturated COx claystone samples under different degrees of saturation, (Yang et al., 2010) obtained the gas permeability value under 5MPa confining stress as $10^{-}19m^2$ and there was no significant permeability increase during the axial stress loading process.

(Liu et al., 2015a) used the transient pulse decay method to perform a triaxial compressive creep test to examine the gas permeability evolution of COx claystone during the creep process. The results showed that when the deviatoric stress was loaded at the initial stage, the gas permeability decreased, and then it moved to a constant steady stage

with stable deformation, and had a slight increase when the creep deformation was large as cracks were created. Scanning electron microscope (SEM) results found that the gas permeability did not increase if the inner pores were not connected. Thus, the gas permeability evolution in the creep test showed three clear stages: decreasing, stable, and increasing stages. The relationship between gas permeability and micro-cracks was also discussed.

(Song et al., 2016) analyzed six COx claystone samples imaged using focused ion beam (FIB)/SEM to predict the macroscopic gas breakthrough pressure with micrometric volumes located in COx claystone. The gas breakthrough in the claystone samples occurred by capillary digitation and the micro-cracks and inner pores were the breakthrough gas pathways. In the claystone, the gas breakthrough pressure was 7-14MPa under normal conditions. (Desbois et al., 2017) used a combination of SEM with broad ion beam (BIB) polishing to study the microstructure evolution of COx claystone and used digital image correlation to measure the inner field of the COx claystone for BIB-SEM analysis.

(Liu et al., 2016) proposed multi-step creep tests under different lateral stresses examine the gas permeability evolution with confining pressure changes. These authors performed one-step creep tests to minimize the effects of the deviatoric stress to obtain complete characterization of the gas permeability evolution with time-dependent deformation of COx claystone. The results showed that the gas permeability decreased with an increase in the confining pressure. Compared with the results of (Liu et al., 2015a), the gas permeability evolution was divided into four stages: rapid decrease, gentle decrease, gentle increase, and rapid increase stages, which were more obvious and had a linear correlation with the volume strains. An accurate deviator level was shown as 88% of the peak stress where the gas permeability turned from decreasing to increasing.

In the study by (Liu et al., 2018b), multi-step triaxial compressive creep tests were performed to investigate the permeability evolution with 5 degrees of deviatoric stresses and three different confining pressures of 2MPa, 6MPa, and 12MPa for COx claystone using the transient pulse delay method. This study showed that both deviatoric stress and confining pressure had effects on creep deformation and gas permeability evolution, the range of gas permeability was negatively correlated with the confining pressure, the gas permeability was stable when the deviatoric stress was lower than 69% of peak stress, and it moved from decreasing to increasing at 88% of the peak stress. The gas permeability evolution in these tests was related to the closure degree of pre-existing micro-cracks and the compaction voids.

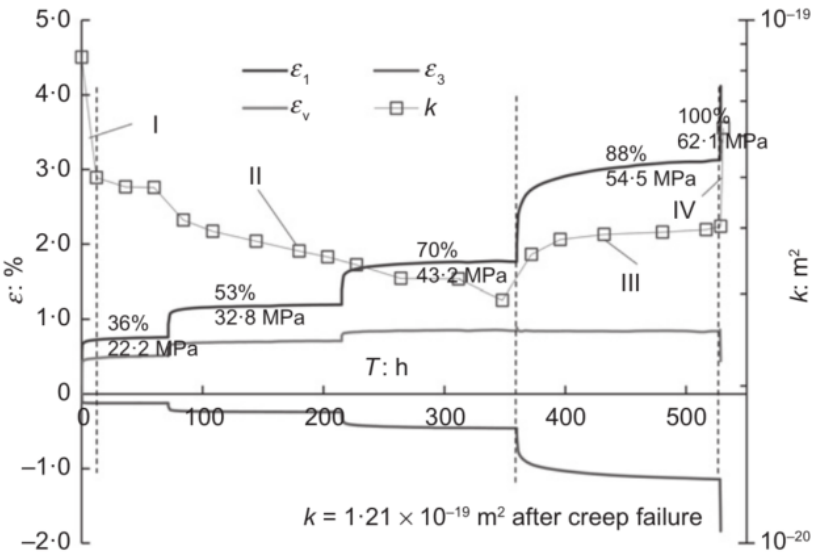

Figure II .12: Creep strains and permeability evolution in triaxial creep test of samples at Pc=12MPa(Liu et al., 2018b)

These results show that the gas permeability evolution for intact and fractured samples should be investigated further.

4 Concluding remarks

A short summary has been provided in this chapter regarding the characterization of the mechanical behaviors of COx claystone. Previous results have outlined the basic features of COx claystone mechanical behaviors. However, further studies are required, especially on the influences of the initial anisotropy and loading path on the instantaneous and time-dependent behaviors and on the poroelastic and poroplastic properties. Gas permeability evolution should also be investigated in fractured samples. These new experimental studies are discussed in greater detail in the next three chapters.

Chapter III

Anisotropic Time-Dependent Behaviors of COx Claystone under Axial Extension

1 Introduction

The excavation and ventilation of underground drifts can induce an unsaturated zone in the claystone formation and a damage zone around the galleries. The existence of such a damaged zone may affect both short- and long-term hydromechanical behaviors of claystone. To date, many studies have been undertaken on the short-term behaviors of COx claystone. However, long-term mechanical behaviors require further investigation because long-term safety analysis is important for geological radioactive waste barrier engineering, and it is necessary to propose a complete investigation of time-dependent mechanical behaviors of COx claystone.

The long-term mechanical behavior of COx claystone has been widely studied under various environmental conditions using different testing methods. A series of CTC creep tests have been used to investigate the effects of the deviatoric stress level and structural anisotropy on creep deformation (Liu et al., 2015b) and to investigate gas permeability evolution mechanism during creep deformation(Auvray et al., 2015a; Bérest, 1987; Fabre and Pellet, 2006; Liu et al., 2016). Unloading and reloading cycles were performed to characterize the variation of elastic modulus during the triaxial creep process(Liu et al., 2017). These results created a reference base for the understanding of time-dependent mechanical behavior. However, these tests were mainly CTC tests, which were undertaken at a constant lateral stress level during deviatoric loading, but the stress path of an un-

derground cavity excavation process is more complicated. In most engineering situations, the lateral stress at the surrounding rock is decreased due to removing the cavity rock, whereas the tangential stress is increased. For this situation, the mean stress remains almost unchanged. Compared with the CTC test, the lateral decompression test where the axial stress increases and the lateral stress decreases, and the axial extension test where the axial stress increases and the lateral stress decreases better reflect the actual excavation situation. A series of lateral decompression tests have been performed to evaluate the effect of temperature on the mechanical strength of COx claystone(Liu et al., 2019a); however, the axial extension loading path has not been investigated to date, although there have been some discussions regarding similar claystones(Bellwald, 1993). In the present study, we undertook laboratory tests on COx claystone using the axial extension loading path.

COx claystone is believed to be a typical anisotropic material with structural bedding planes. Structural anisotropy affects mechanical responses in mini-compression and micro-indentation tests(Zhang et al., 2012). The material anisotropy has an important influence on the mechanical properties (Masri et al., 2014). Previous studies have mainly focused on the influence of anisotropy on the mechanical strength of the rock, and there have been limited studies on the influence of anisotropy on rock deformation. Therefore, the influence of anisotropy on the mechanical deformation properties was examined using creep tests in the present study.

In this chapter, we designed an axial extension creep test with constant mean stress to investigate the mechanical deformation of COx claystone under two stress levels. To investigate the influences of initial anisotropy on creep deformation, these tests were performed on samples under five different loading angles regarding the bedding planes of COx claystone (0^o, 30^o, 45^o, 60^o and 90^o). The experimental results were analyzed and summarized concerning loading orientation and stress level.

2 Sample Preparation and Equipment

2.1 Sample Preparation and Production

The samples used in this thesis are drilled from original rock cores, which are taken from the sedimentary layer Callovo-Oxfordian in area Meuse/Hault-Marne where the French nuclear waste underground laboratory located(see FigureIII .1). The original rock core is 300 mm in length and 78.5 mm in diameter. The samples tested are drilled from the core in laboratory in its natural saturation degree to minimize the impact of water content

during sample preparation.

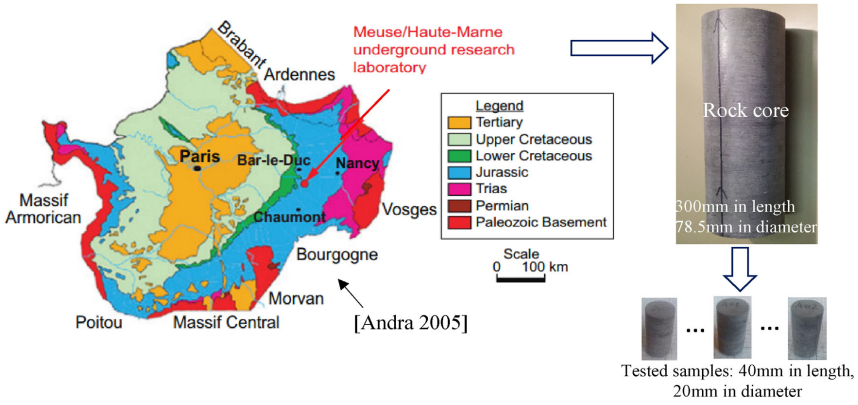

Figure III .1: Overview of the sample location and preparation(Liu et al., 2016)

In this chapter, No.55522, No.58123, No.60710 and No.60788 rock cores are selected. The cylindrical samples, with 30-40mm in length and 20mm in diameter, are drilled from these rock cores. In order to investigate structure anisotropy affect on deformation behavior, samples are also drilled as five angles with respect to bedding planes of the COx claystone (0^o, 30^o, 45^o, 60^o and 90^o). Also, the two sides of each sample are carefully polished to obtain smooth and well parallel surfaces.

When drilling samples from the original core, two or three small samples are chosen to measure its moisture content ω. Two or three pieces of rocks are made from received core to obtain the initial water content of the samples. Immediately after their manufacture, the masses of the pieces are weighed on a precision balance at 0.001g. Then they are respectively placed in an oven drying at 105 ° C. When the sample variation between 2 successive weighings at 24h interval is less than 0.1%, it is possible to calculate the initial water content with the following relationship by comparing the masses of a sample before and after drying process.

$$\omega(\text{initial})_{20^\circ\text{C}} = \frac{m(\text{initial})_{20^\circ\text{C}} - m(\text{sec})_{105^\circ\text{C}}}{m(\text{sec})_{105^\circ\text{C}}} \times 100\% \qquad \text{(III .1)}$$

$\omega(\text{initial})_{20^oC}$ is the initial water content at room temperature, $\text{m(initial)}_{20^oC}$ is the initial sample mass at room temperature and m(sec)_{105^oC} is the reference dry sample mass(drying at 105^o C).

In order to minimize the water loss, after drilling process, the cored samples should be stored in a vacuum plastic bag and placed in a chamber at a pressure of 0.1MPa. Because the test uses strain gauge to measure axial and lateral strain, so before formal test, the

sample should be taken out to be attached two pairs of strain gauges at middle height. The steps are showed in FigureIII .2.

Figure III .2: Steps of attach two pairs of strain gauge to the sample

To prevent water loss, all steps for the sample must be completed quickly, and plastic films are used to minimize sample desaturation. As long as the preparation steps are finished, the samples should be resealed carefully. And the water content has not been re-measured, considering that the shelf life is quite short.

2.2 Testing Equipment and Method

The tests are carried out in the Lamcube laboratory(Laboratoire de Mécanique, Multiphysique, Multiéchelle) of the University of Lille. The testing system is a new triaxial direct tension (TDT) apparatus developed to do the tensile tests on COx claystone(Liu et al., 2019b). The main components of the apparatus are the same as those of conventional triaxial compression(CTC) testing device that has been proven to have a good performance in rock triaxial compressive testing(Han et al., 2019, 2016; Liu et al., 2018a). The modifications from the CTC apparatus include the tension chamber and the axial pulling components with the accessories. The loading piston is devised to be able to apply either a compressive or a tensile stress in the axial direction, by controlling the pressures in the two chambers separated by the ring of the piston. Screwing connections are used between the steel components such as the pull rod as well as the supporting head. Cement connection is used between rock specimen and its supports. Cement is critical important in the sample preparation to adapt the rock property surface dry and clean. The centralization of all the pieces is another important point in the tension apparatus. Thanks

to the fabrication technology, centralization of steel components nowadays has become easier. The key controlling procedure is thus the centralization of specimen with the steel components. The sketch of the TDT apparatus is shown in FigureIII .3.

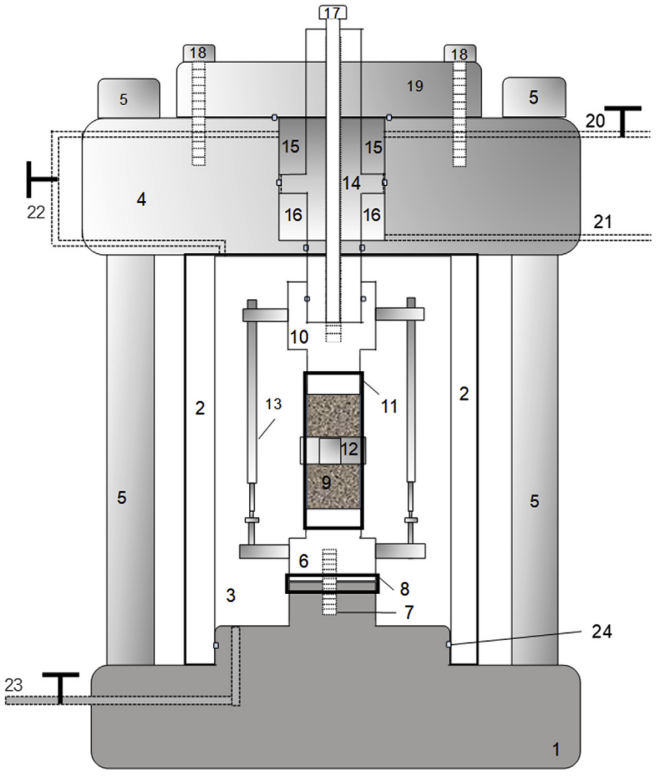

1-device base 2-triaxial cell chamber wall 3-triaxial chamber 4-chamber cap 5-pull rod with screw into 2
6-specimen supporting base 7-connecting screw 8-sealing jacket 9-specimen
10-specimen supporting head for pulling 11-specimen sealing jacket 12-ring for radius strain measurement
13-LVDT for axial strain measurement 14-loading piston 15-autocompensated chamber
16-tension force production chamber 17-pull rod with screw into 10 18-screwing rod
19-sealing cap of chamber 15 20-tube with valve between chamber 15 and the outside
21-tube with valve between chamber 16 and a hydro-servo pump for direct tension loads
22-tube with a valve between chamber 3 and 15
23-tube connecting to a hydro-servo pump for confining pressure loading

Figure III .3: Sketch of TDT apparatus

In the developed TDT apparatus, the pressure, stress, displacement, and strain are measured by sensors. Two syringe pumps are used in this equipment. One is for applying the confining pressure, the other for tension force. The pumps can apply a pressure up to 60MPa with a precision of 0.1bars; in addition, the pumps can also control the inject flow rate from 0.0005ml/min to 5ml/min. In this test, the axial and lateral strains are measured with two pairs of strain gauges. As another option, the axial strains could be measured by a pair of LVDTs and radius strain could be measured by a special circumferential ring, which would be used in other tests.

In axial extension tests, the mean stress is maintained as a constant value. In loading phase, when lateral stress increases, axial stress decreases with the relation below:

$$\Delta q = \Delta\sigma_a - \Delta\sigma_r < 0, \Delta\sigma_m = (\Delta\sigma_a + 2\Delta\sigma_r)/3 = 0 \quad \text{(III .2)}$$

Δq is deviatoric stress increment; $\Delta\sigma_a$ is axial stress increment; $\Delta\sigma_r$ is lateral stress increment; $\Delta\sigma_m$ is mean stress increment.

So, the axial extension creep tests are designed with 12.5MPa constant mean stress, the mean stress value is determined by the actual mean stress on the project site. Two stress state levels are loaded in these tests, the initial state σ_a=σ_r=12.5MPa is set as 0% stress stage.When the axial stress is 0MPa, that is, the stress state is σ_a=0MPa and σ_r=18.75MPa. For simplicity, we assume that this state is the 100% stress loading stage. And the two stress state levels are respectively set as 50% stage(σ_a=6.3MPa, σ_r=15.6MPa) and 90% stage(σ_a=1.3MPa, σ_r=18.1MPa). At first, samples are subjected to 12.5MPa hydrostatic stress state, secondly axial stress is then reduced while lateral stress is increased to maintain a constant mean stress. The Variations in the axial and lateral strains over time are measured at two different stress levels. In addition, in order to consider initial anisotropy effect, six samples C1–C6 as 0°, 30°, 45°, 60° and 90° are selected to do the tests.

Also, all tests are conducted in a thermally insulated room at constant temperature (20± 0.5°C) maintained by an air-conditioner in order to avoid temperature influence.

TableIII .1 shows sample parameters as well as loading process details.

Table III .1: Sample geometry, testing conditions and results of testing program

Samples number	Moisture Content ω	Diameter mm	Length mm	50% Degree Day	90% Degree Day
EST55522 C1 0°	6.40%	19.50	39.67	50	120
EST60788 C2 30°	5.60%	19.88	34.71	20	20
EST55522 C3 45°	6.40%	19.80	33.40	16	40
EST60710 C4 60°	6.20%	19.80	26.20	26	20
EST55522 C5 90°	6.40%	19.87	40.28	18	115
EST58123 C6 90°	7.02%	19.74	32.34	12	

3 Axial extension creep tests

In these tests, five angles samples are proposed with two stress state levels, which is shown in FigureIII .4. The 50% and 90% stage would be respectively last for 280–1200 hours (12–50 days) and 480–2880 hours (20–120 days). The strain-time curves with five angles during creep process are shown in FigureIII .5.

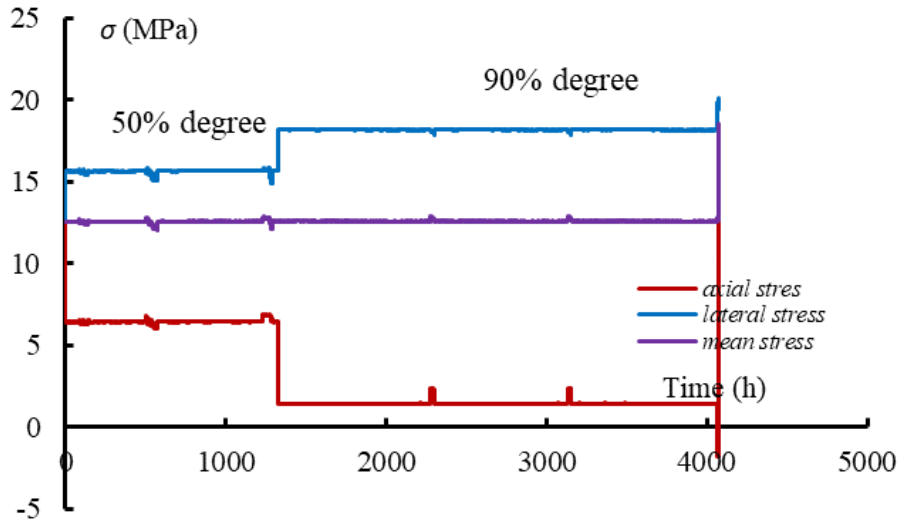

Figure III .4: Stress-time curve of Sample C1

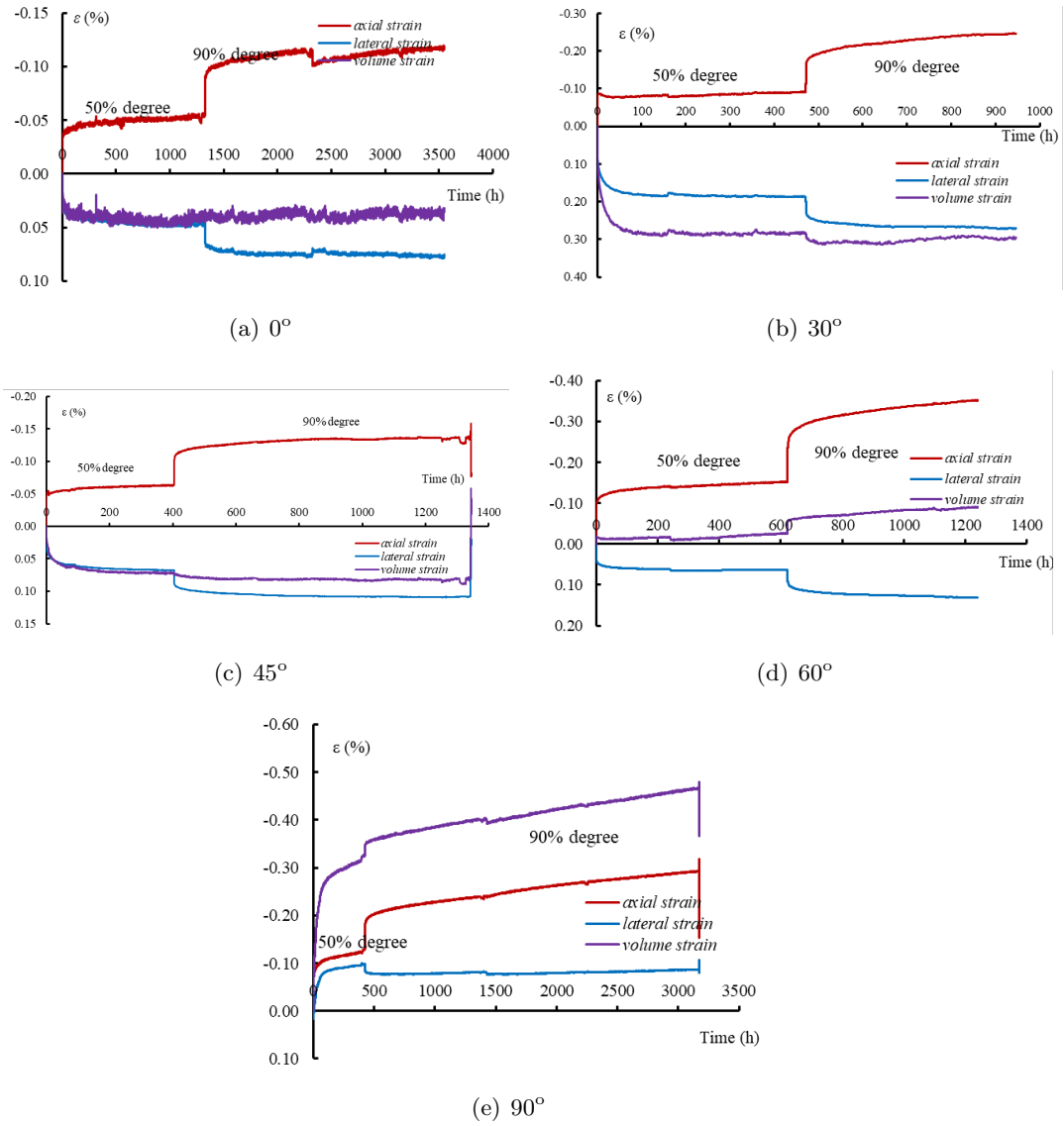

(a) 0° (b) 30°

(c) 45° (d) 60°

(e) 90°

Figure III .5: Strain-time curve evolution for axial extension tests

From FigureIII .4 we could see, as stress state loaded, the lateral stress increases and axial stress decreases. Throughout the thesis, the positive sign is attributed to compressive stresses and strains, and the negative sign is attributed to tensile stresses and strains. Take deformation evolution of 0° sample C1 in FigureIII .5(a) as example, when stress level loaded to 50% stage, the lateral direction is compressed and lateral strain turns to be stable after 300 hours, the axial direction is dilated and axial strain turns to be stable after 500 hours. When stress level loaded to 90% stage, lateral strain continues to increase and axial strain continues to decrease. After stress state keeps stable, the creep process is continuing and after 1000 hours the deformation turns to be stable. It can be seen from

FigureIII .5 that the stress level have a greater impact on creep deformation degree. At 50% stage, the creep deformation is within a small range and quickly remains stable. At 90% stage, the stabilization time is longer. For other three tests of 30°, 45° and 60°, the results showed the same trend.

For 90° sample C5, its axial deformation trend at 50% and 90% stage and lateral deformation trend at 90% stage seems to be similar to other four angles, but at 50% stage, its lateral strain is decreased, which means that the sample is dilated in both axial and lateral direction at 50% stage. This phenomenon seems unreasonable. It may be attributed to the operation mistakes produced during the experiment.

Therefore, in order to re-verify the lateral deformation of 90° sample at 50% stage, sample C6 of 90° is prepared for repeating the test at 50% stage. FigureIII .6 shows the strain-time curve of sample C6. The curve shows, at 50% stage, the axial strain is decreased and lateral strain is increased, the trend seems to be reasonable. When loaded to 90% stage, the sample turns to lateral compression failure, this may due to its inner structure defects and cracks. The axial strain increment is 0.116% at 50% stage, the value is very close to the 0.109% axial strain increment of sample C5. And when samples C5 and C6 are loaded to 90% stage, the volume strains both start to turn from compression to dilatation. Therefore, according to these similar aspects, the two tests are both thought to be representative for reflecting mechanical properties of 90° angle.

And for 90° sample C5, if we just consider the strain increment at 90% stage, as FigureIII .7 shows, we could see when sample is loaded from 50% to 90% stage, the lateral strain increases and axial strain decreases, it seems to be reasonable consistent with the other four samples.

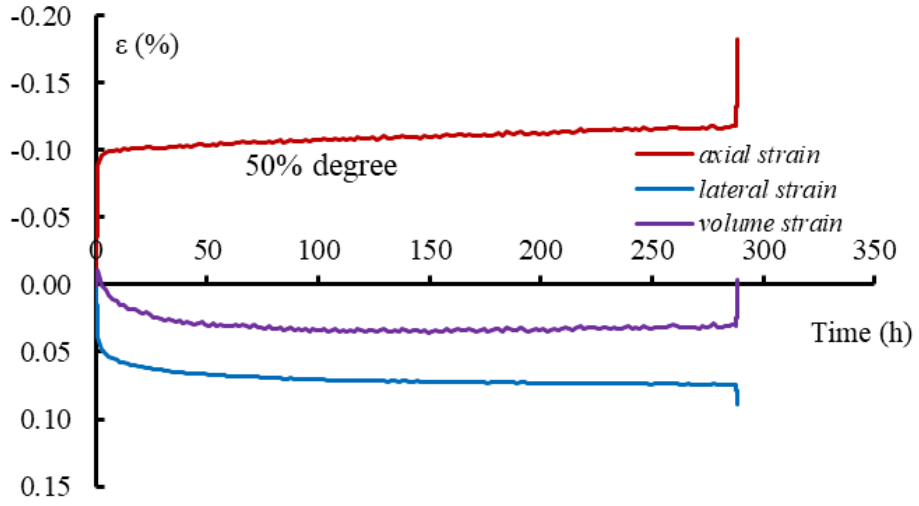

Figure III .6: Strain-time curve evolution for axial extension test of C6 sample of 90° direction

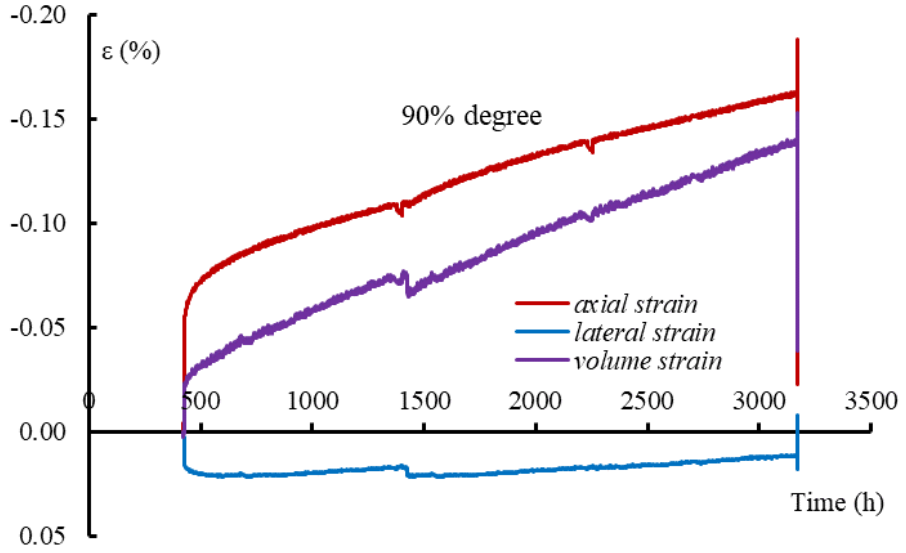

Figure III .7: Strain increment-time curve evolution for axial extension test of C5 sample of 90° direction from the 90% loading stage

4 Creep response of claystone in parallel direction

As shown in TableIII .1, we finally realized six axial extension creep tests on different angle samples(including one test on perpendicular sample for verifying strain on 50% loading stress). Among these tests, the creep response of 0° parallel sample is first to be analyzed.

The axial strain evolutions during the creep process of the two step creep tests on parallel sample are shown in FigureIII .5(a). It is evident that the extension loading level has an important enhancing effect on the amount of axial creep strain of the claystone during the primary and steady creep.

The higher the extension stress level, the greater the axial strain. Also, the axial strain curves indicate that, the augmentation of the axial strain induced by the increase of extension creep stress from 50% to 90% extension stress levels is more important than that from 12MPa hydrostatic stress state to 50% extension creep stress level. Moreover, it can be roughly concluded from the creep strain curves that:

(i) The claystone axial creep strain trends to be steady after 10days of creep with 50% extension creep stress;

(ii) The claystone lateral creep strain trends to be steady after 20days of creep with 90% extension creep stress;

(iii)The corresponding lateral strain is also given in FigureIII .5(a) for 0^o parallel sample. The trend revealed by the lateral strain is mainly consistent with that of the axial strain.

(iv)The total lateral strain is almost the same value as the axial strain with 50% extension creep stress, and the value of the total lateral strain increment is about half of the total axial strain increment from 50% to 90% extension creep stress. Thus, during all the creep tests performed here, the claystone deformation is always compressive and almost unchanged during two loading stages as indicated by the volume strain shown in FigureIII .5(a).

In order to well present the creep behaviors due to the applied different extension stress levels, the axial and lateral creep strain rates are calculated by

$$\dot{\varepsilon}_T = \frac{\varepsilon_{T+1} - \varepsilon_T}{\Delta \mathrm{T}} \tag{III .3}$$

$\dot{\varepsilon}_T$ means the creep rate at time T. ε_{T+1} and ε_T are respectively the creep strains at adjacent moments T+1 and T.

The results for five angles are shown in FigureIII .8-III .12. The axial and lateral creep rates significantly decrease at initial creep stage and trend to be stable at the steady creep stage. Moreover, the creep rates increase slightly with the applied level of extension stress. For both extension loading stages, the axial and lateral creep strain rates at the initial creep stage range from 10^{-10}/s to 10^{-11}/s, and the steady creep rates range about 10^{-11}/s. But for 90^o sample, at 90% stress state, the axial steady creep rate is 2×10^{-10}/s. The axial creep deformation continues to increase at steady stage as shown in FigureIII

.5(e).

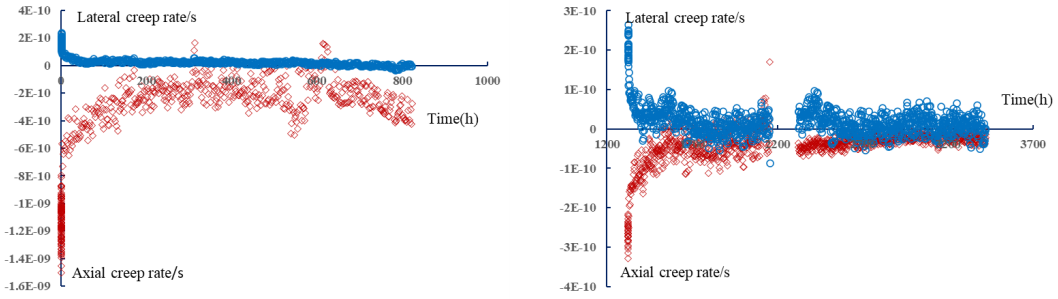

(a) 50% (b) 90%

Figure III .8: Creep rate of 0° sample

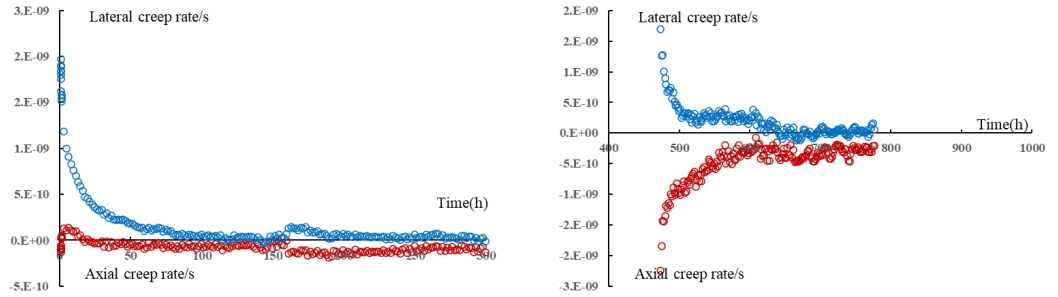

(a) 50% (b) 90%

Figure III .9: Creep rate of 30° sample

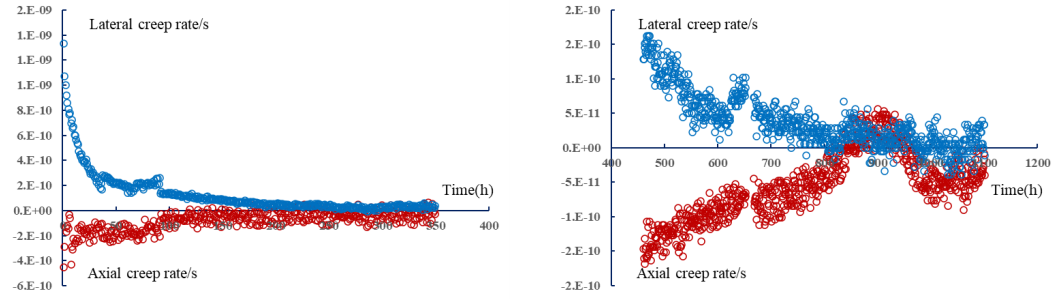

(a) 50% (b) 90%

Figure III .10: Creep rate of 45° sample

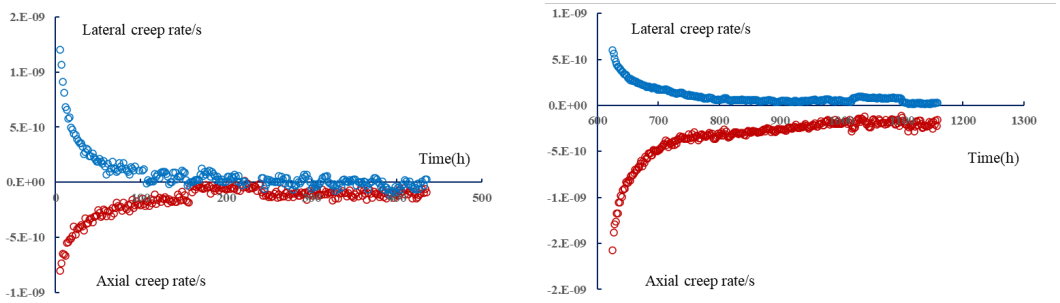

(a) 50% (b) 90%

Figure III .11: Creep rate of 60° sample

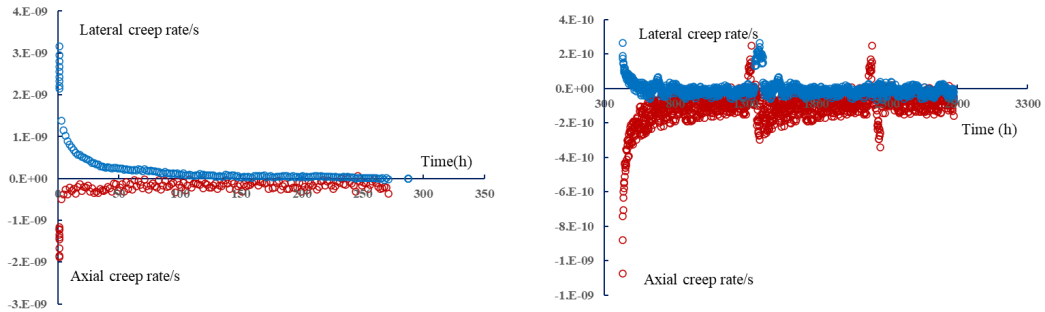

(a) 50% (b) 90%

Figure III .12: Creep rate of 90° sample

5 Anisotropy effects on extension creep strains

From FigureIII .5 we could see that stress state level has great impact on axial and lateral strains. Compared to the 50% loading stage, when the stress state is loaded to 90% stage, the axial and lateral strains are developed more important and the creep strains need more time to stabilize.

By comparing five angles tests we can see when stress state keeps constant, both axial and lateral strains shows difference due to structure anisotropy of COx claystone. This is because the interior of COx claystone is heterogeneous and filled with discontinuous surfaces formed by the accumulation of various strata, where surfaces are often stacked in a direction parallel to the strata. So the direction and magnitude of stress and strain on the internal discontinuity surface of each sample are also different. Thus, for each angle different degrees of slippage, misalignment, and tensile damage will occur.

Therefore, in order to better reflect the influence of stress degree and anisotropy on

sample deformation, TableIII .2 shows the axial, lateral and volume deformation increment of sample C1–C6 at 50% and 90% stress stages. These deformation increments are plotted in FigureIII .13 to better analyze the deformation trend. Which should be noted that for sample C5, only the strain increment at 90% stage is taken, and for sample C6, only the strain increment at 50% stage is taken.

Table III .2: Increasement of sample deformation

Samples number	$\Delta\varepsilon_a$ % 50% Stage	$\Delta\varepsilon_a$ % 90% Stage	$\Delta\varepsilon_r$ % 50% Stage	$\Delta\varepsilon_r$ % 90% Stage	$\Delta\varepsilon_v$ % 50% Stage	$\Delta\varepsilon_v$ % 90% Stage
C1 0°	-0.057	-0.063	0.045	0.034	0.034	0.004
C2 30°	-0.090	-0.156	0.187	0.084	0.285	0.010
C3 45°	-0.045	-0.041	0.067	0.041	0.090	0.041
C4 60°	-0.149	-0.203	0.064	0.067	-0.022	-0.067
C5 90°	-0.109	-0.157		0.013		-0.131
C6 90°	-0.116		0.074		0.032	

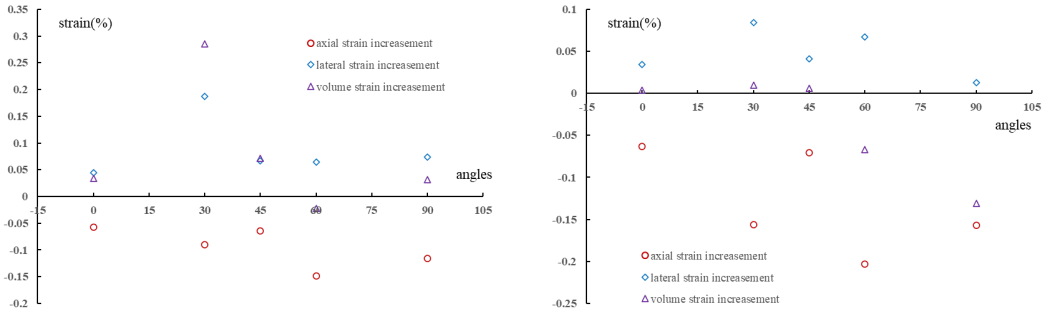

(a) 50% stage (b) 90% stage

Figure III .13: Strain increase evolution with five different angles

From FigureIII .13, for axial strain increments, by comparing two stress states, except for the 45° sample, we could see the increment at 90% stage is larger than it at 50% stage. By comparing five angles, we could see in both two stress state levels, axial increment of 30°,60° and 90° is larger. For 30° and 60° samples, the deformation mainly comes from

the shear slip of the discontinuous surface of the formation inside the sample, and the shear slip is more conducive, thus showing a more obvious trend. For 90° sample, since the axial direction is perpendicular to the bedding planes, the axial strain increment is greater than that of 0° sample.

For lateral strain increments, except for the 60° sample, the increment at 90% stage is smaller than it at 50% stage, Because when the stress level increases to the 50% stage, the sample is almost compacted in lateral direction, so even if the sample is loaded to a higher stress state level, the lateral strain increment cannot increase continuously. By comparing five angles, we could see for two stress state levels, lateral increment of 30° and 60° is larger for the same reason. The lateral deformation of 90° sample is smallest, because for 90° sample lateral direction is parallel to bedding planes. For the 0° sample, the lateral strain is smaller, because the axial direction of sample is parallel to the bedding planes, in the hydrostatic load stage, the lateral strain has been greatly compacted, which leads to a smaller lateral strain in axial extension creep stages.

For volume strain increments, at 50% stage, except for the 60° sample, the volume strain evolutions of 0°, 30° ,45° and 90° samples show that samples are compressed. These results show that at 50% stage, the sample is compressed or slightly delated. And at 90% stage, for 0°, 30°, and 45° samples, the volume deformation keeps constant in compression zone, and the values are close to 0, which means that at 90% stage the volume deformations of these samples are almost unchanged. But for the 60° and 90° samples the volume strains show clearly dilatation.

6 Concluding remarks

From the axial extension creep tests results and analysis of this chapter, the following conclusions can be drawn:

(1) In the axial extension loading path, with axial stress decrease and lateral stress increase, the axial deformation was dilated and lateral deformation was compressed. At the 50% stress level, the creep deformation remained stable over 10 days. At the 90% stress level, the creep rate was accelerated and the stabilization time was 20 days. The results showed that under a higher stress state, the creep steady time took longer. Different from the low creep rates of 10^{-11}/s in the creep steady stage at the 90% stress state, the 90° sample creep rate was 2×10^{-10}/s. Therefore, for the 90° sample, the axial creep deformation continued to increase during the steady stage.

(2) By analyzing the strain increments between the two stress state levels, for axial

deformation, the increment at the 90% stage was greater than that at the 50% stage, and for lateral deformation, the increment at the 90% stage was smaller than that at the 50% stage.

(3) By analyzing the deformation (axial and lateral) characteristics of the five loading angles, the deformation of the 30°, 60° and 90° samples was significantly large. For the 30° and 60° samples, this was because the deformation mainly arose from the shear slip of the discontinuous surface. Depending on the 30° and 60° angles, the shear slip was more conducive. For the 90° sample, because the axial direction was perpendicular to the bedding planes, the axial strain was greater than the lateral strain, and was greater than the axial strain of the 0°, 30° and 45° samples. For the 0° sample, the axial and lateral strains were the smallest because the axial direction was parallel to the bedding planes, which affected the axial strain. The sample was compacted during the hydrostatic loading stage, leading to smaller lateral strain during the creep stage.

(4) By analyzing volume deformation characteristics of of five angles. We can see at 50% stage, for 0°, 30°, 45° and 90° samples the volume deformation shows to be compressed. For 60° sample, the volume deformation shows to be delated slightly. At 90% stage, for small angles 0°, 30°, and 45° samples, the volume deformation are still in compression zone and almost unchanged. For large angles 60° and 90° samples, the volume strains shows significant creep expansion.

(4) By analyzing the volume deformation characteristics of the five angles, at the 50% stage, for 0°, 30°, 45° and 90° samples, the volume deformation was compressed. For the 60° sample, the volume deformation was delated slightly. At the 90% stage, for the 0°, 30°, and 45° samples samples, the volume deformation was still in the compression zone and was almost unchanged. For the larger angles of 60° and 90° samples, the volume strains had significant creep expansion.

Chapter IV

Gas Permeability Evolution of COx Claystone under Shear Creep Stress

1 Introduction

Over the long-term, gases accumulate in large quantities in the underground radioactive waste repository due to the erosion of metallic wastes, anaerobic microbial activity, degradation of cellulosic materials and other organic materials in the waste, and gas released from small living organisms in the barrier rock formation (Liu et al., 2017; Voinis et al., 1992; Yang et al., 2010). The release of these gases from the barrier rock induces leakage of nuclide in the life cycle, which will cause severe consequences. Further, gas permeability is more sensitive than water permeability to microstructure changes of rocks such as the growth of micro-cracks. Thus, it is vital to characterize the gas permeability evolution of the barrier rocks, especially the excavation damaged zone for sealing property over the long-term.

The gas permeability evolution of COx claystone has been investigated previously using many different techniques. Gas permeability has been used as a good indicator for detecting the induced damage and sealing capacity of intact COx claystone using gas injection in hydrostatic or triaxial shear tests (Billiotte et al., 2008; Zhang and Rothfuchs, 2008). The gas permeability of intact COx claystone under high level deviatoric creep stress has been observed with a decreasing phase (Liu et al., 2015a) and permeability evolution in triaxial creep process was closely related to microstructural evolution, including the closure of pre-existing micro-cracks, compaction of voids, and coalescence of micro-cracks(Liu et al.,

2018b). The mechanism of the gas permeability evolution during creep deformation has been investigated and the gas permeability in multi-step creep tests exhibited a four-stage evolution with a progressive increase of the deviatoric stress level, which was composed of a rapid decrease, a gentle decrease, a gentle increase, and a rapid increase (Liu et al., 2016).

These previous studies confirmed the mechanical behavior of the intact COx claystone due to compressive stresses; however, the complete characterization of the transport properties under shear failure conditions in low-permeable COx claystone in concurrence with the time-dependent deformation has still not been resolved. In real engineering excavation processes, the rock mass is usually not intact; the initiation, propagation, enclosure, and healing of macroscopic fractures can significantly affect the short- and long-term behavior of COx claystone; and the description of the penetration mechanism of the fractured zone with cracks over the long-term is more complicated, and requires further investigation.

Despite many studies already being undertaken, a crucial issue to be addressed is the evolution of the transport properties with the fracture surface in rock samples, particularly water and gas permeability to reflect seepage and deformation characteristics of the rock fracture zone during the engineering excavation process. Such experimental data are mandatory for a better understanding of transport properties in COx claystone in this chapter. Therefore, we aimed to undertake a series of direct shear creep tests with the permeability measurement to investigate the creep deformation evolution of intact and fractured samples and gas permeability evolution. In particular, the influence of the stress level was investigated.

In this chapter, with the help of a specific device, three direct shear tests were undertaken during the first stage to create longitudinal fractures in cylinder samples under different confining pressure values. The fractured samples were then subjected to different levels of prescribed shear stress during the creep stage. Variations of creep strains and gas permeability with time were measured at each step of creep. Finally, a test was performed to investigate gas permeability evolution induced by hydrostatic stress compaction and to inject gas pressure. Emphasis was placed on the gas permeability evolution. The obtained results are discussed concerning the influences of creep deformation and confining pressure, and the self-sealing ability of fractures.

2 Experimental apparatus and method

For previous studies, the Lamcube has developed an experimental device allowing to generate a diametral fracture in a cylindrical sample, and then to perform normal compression and direct shear tests on intact and fractured samples in short and long term (FigureIV .1). It is also possible to perform hydromechanical tests by injecting gas into the fracture and to evaluate the gas permeability evolution as a function of the fracture deformation. The testing system is consisting of three independent components for hydromechanical loading, deviator stress loading (which could be used as shear stress loading) as well as interstitial pressure generation and monitoring, which are all assembled independently in triaxial cell. Also, there is a data acquisition center to record the test parameter such as pressure, flow rate and deformation. The Nitrogen gas is chosen as the inject gas because of its applicability as well as chemical stability with respect to the minerals constituting COx claystone. And all the tests are carried out in a thermally isolated small room where the temperature is maintained as 23 °C by a central air-conditioner in order to exclude the temperature fluctuations influence. The axial strain ε_a and lateral strains ε_r are measured respectively by linear variable differential transducers (LVDT) and collier ring in series of tests.

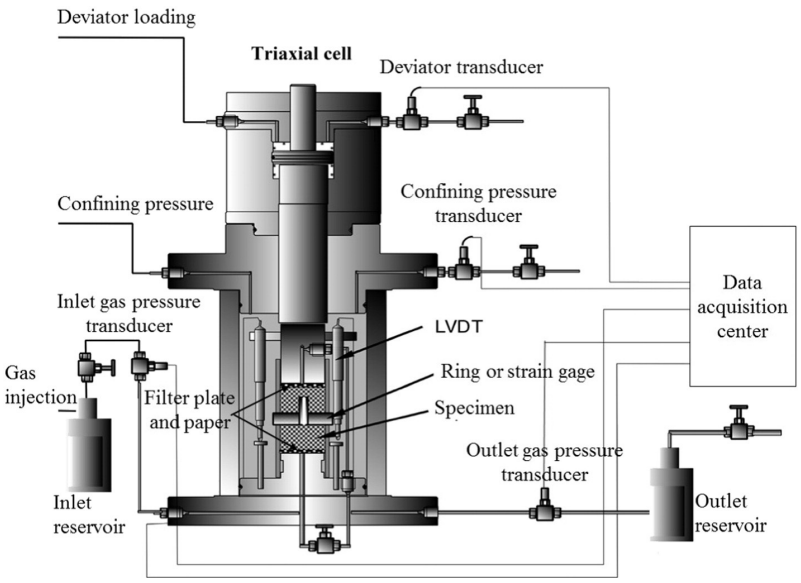

Figure IV .1: Sketch of experimental apparatus for sheer tests

Also a planar fracture should be created for shearing process. A special device is used to change the deviator stress to shear stress(Yang et al., 2017). FigureIV .2 shows the device

structure. This device contains two cylindrical shearing discs with the same diameter as the sample. Each disc is consists of two half-discs which consists of two different materials (A and B). The two half-discs are placed in opposite positions at both top sides as well as bottom sides. Due to a deviator stress loaded, an axial displacement generated by the cell piston creates a shear stress along the diameter plane of the sample, leading to a planar fracture, and then the shear stress is applied along the fracture. Note that a rotation force can be generated before the creation of a fracture due to the difference of forces applied to two half-discs. After a series of preliminary tests, it is found that the effect of such a rotation force is very small, and no sample rotation is observed.

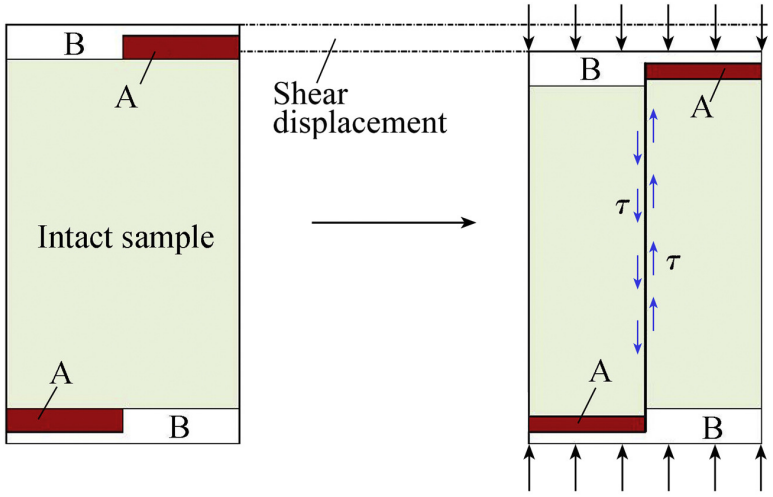

Figure IV .2: Sketch of the device to create shear stress(Yang et al., 2017)

The samples used in the experimental program is EST58123 rock core, the sample preparation program is almost the same with it shows in ChapterIII which is cored to specified size from the original core to obtain a well-mannered mechanical behavior. Samples are drilled in perpendicular direction of bedding planes of COx claystone stratum. The drilled cylindrical samples are about 34 mm in length and 37 mm in diameter. Once drilled, each sample end is polished to be perpendicular to the sample axis as ChapterIII showed.

In these tests, steady state flow permeability method is used to calculated gas permeability k as Darcy's law, which can be directly applied to derive k from imposed flow rate or pressure conditions. A brief test method summary is showed below.

A pressure sensor is set in gas inject reservoir to record the inject gas pressure P_{in}

and the downstream valve is open so the output gas pressure P_{out} is equal to atmospheric pressure as 0.1MPa. The instantaneous flow is also record by a flow meter so Q_v could be obtained. Then the gas permeability k could be obtained as:

$$k = 2P_{out}Q_v\mu L/At(P_{in}^2 - {P_{out}}^2) \quad \text{(IV .1)}$$

k is the apparent gas permeability in m^2; L(m)and A(m) are respectively the length and the cross sectional area of the sample; μ is the dynamic viscosity of the Nitrogen gas as 17.484×10^5 Pa·s. $Q_v(m^3)$ is respectively the gas volume flow from the outlet reservoirs in a period of time t. P_{in} and P_{out}(Pa) means the gas pressure of the inlet and outlet reservoirs.

So the whole test is divided into five phrase. Phrase 1 is at hydrostatic state with gas pressure loading to verify the breakthrough gas pressure. Phrase 2 is the shear creep loading section with gas permeability evolution for intact sample, this phrase contains 50% of assumed peak shear stress loading stage(stage 1) and 90% of assumed peak shear stress loading stage(stage 2). Phrase 3 contains shear failure stage(stage 3). Phrase 4 is the shear creep loading section with gas permeability evolution for fractured sample, this phrase contains 50% of the actual peak shear stress loading stage(stage 4) and 90% of the actual peak shear stress loading stage(stage 5). Phrase 5 is hydrostatic loading stage with fractured sample to verify the relationship between gas permeability with hydrostatic pressure and inject gas pressure.

The tests are executed mainly in following steps:

(a) Check each part of the testing system and make sure it functions well.

(b) Install the sample at the right position with a filter paper, a filter plate and a cylindrical shearing disc at each sample end, then seal the sample in a plastic jacket from the pressure chamber of the triaxial cell.

(c) Apply the confining pressure with the rate 0.05MPa/min to a given level such as σ_r=6MPa and maintain it.

(d) Inject the inert Nitrogen gas to keep the pressure as a suitable value, and let the downstream valve open, then wait until the gas started to flow out from the downstream reservoir to verify the gas breakthrough pressure.

(e) Load the shear stress to stage 1 as 50% of the assumed peak shear stress and keep the stress state at least for two weeks until the deformation keeps stable.

(f) Load the shear stress to stage 2 as 90% of the assumed peak shear stress and keep the stress state at least for three weeks until the deformation keeps stable.

(g) Load the shear stress until sample starts to be shear broken at stage 3. Record the

actual peak stress. Then reload shear stress to Stage 4 as 50% of the actual peak strength at least for two weeks until the deformation keeps stable.

(h) Load the shear stress to Stage 5 as 90% of the actual peak strength at least for three weeks until the deformation keeps stable or the deformation becomes unstable and accelerates.

For the shear creep tests in this chapter, three COx claystone samples C15, C16 and C17 of EST58123 are selected. The specific experimental parameters and process details are shown in TableIV .1 and TableIV .2

Table IV .1: Sample geometry and testing condition of sheer creep test

Samples number	Moisture Content ω	Diameter mm	Lenth mm	Confining Pressure MPa	Pore Pressure MPa	Stage 3 Peak Strength MPa
EST58123 C15 90°	7.10%	37.02	34.40	6	1.5	$\tau_{peak} = 7.13$
EST58123 C16 90°	7.10%	36.58	32.25	12	1.5	$\tau_{peak} = 8.90$
EST58123 C17 90°	7.10%	36.80	34.65	12	5.5	$\tau_{peak} = 9.06$

Table IV .2: Test result parameters of sheer creep test

Samples	Stage 1	Stage 2	Stage 4	Stage 5
number	Percent of peak stress	Percent of peak stress	Percent of peak stress	Percent of peak stress
C15	33.1% $\tau = 2.35$MPa	60.0% $\tau = 4.28$MPa	50.2% $\tau = 3.58$MPa	
C16	37.6% $\tau = 3.35$MPa	64.0% $\tau = 5.38$MPa	51.7% $\tau = 4.60$MPa	
C17	38.6% $\tau = 3.50$MPa	70.2% $\tau = 6.36$MPa	50.8% $\tau = 4.60$MPa	78.4% $\tau = 7.10$MPa

3 Permeability and strain evolution in shearing creep tests

3.1 Determination of gas breakthrough pressure

Before formal test, it is necessary to determine gas breakthrough pressure. Take shear creep test under 12MPa confining pressure with sample C17 as example, FigureIV .3 shows

the method.

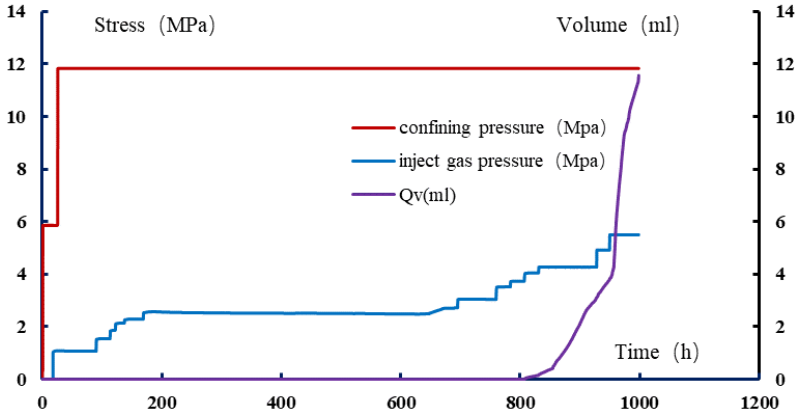

Figure IV .3: Confining pressure, inject gas pressure and gas volume evolution with time at initial stage with sample C17

We can see from FigureIV .3 at initial stage, when the injection pressure is small, gas flow rate value shows 0, the result indicates that when injection pressure is smaller than breakthrough pressure, the gas cannot penetrate through the sample. As the inject gas pressure continues to increase, when it reaches 3.7MPa, the flow meter monitors the gas flow as a small value. Then, the inject gas pressure continues to increase, and the gas flow rate also shows an upward trend. When the injection pressure reaches to 5.5MPa, obvious outgassing can be detected in the gas outlet end of the instrument. Therefore, for this test, the breakthrough pressure is determined as 5.5MPa, and the inject pressure is maintained at 5.5MPa for whole test process. For shear creep tests under 6MPa confining pressure with sample C15 and 12MPa confining pressure with sample 16, the breakthrough pressures are both determined as 1.5MPa.

3.2 Permeability measurement under shear creep stress

3.2.1 Permeability measurement with confining pressure of 6MPa

For shear creep test under 6MPa confining pressure with sample C15, 4 stages are carried out, stage 1 is loaded 33.1% peak stress with intact sample, stage 2 is loaded 60.0% peak stress with intact sample, then the test enters shear failure stage as stage 3, and stage 4 is loaded 50.2% peak stress with fractured sample. Peak shear strength is 7.13MPa. FigureIV .4 shows the evolution relationship between shear stress and strain. FigureIV .5 shows the evolutions of confining pressure, shear stress, deformation, injection pressure, and gas permeability with time.

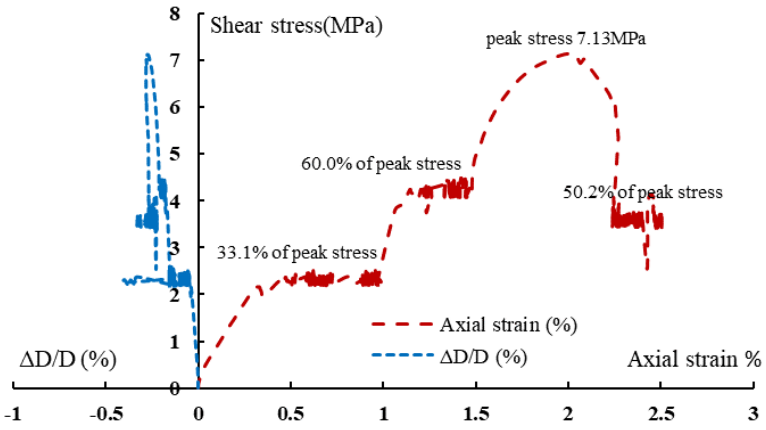

Figure IV .4: The evolution relationship between shear stress and deformation of shear creep test under confining pressure of 6MPa with sample C15

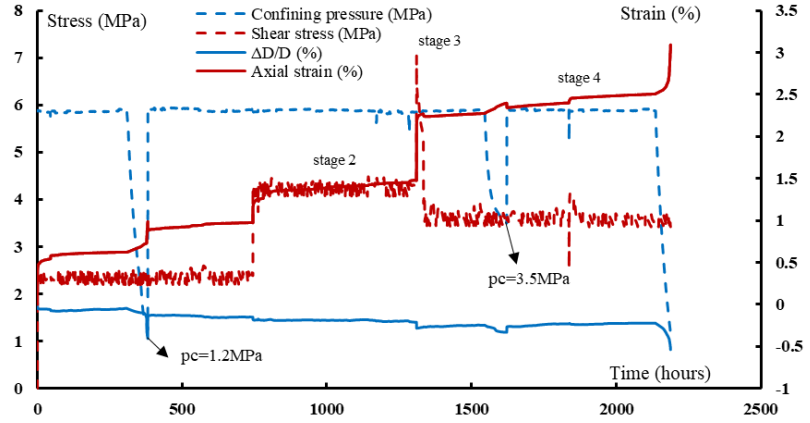

(a) the evolution relationship between shear stress, confining pressure and deformation with time

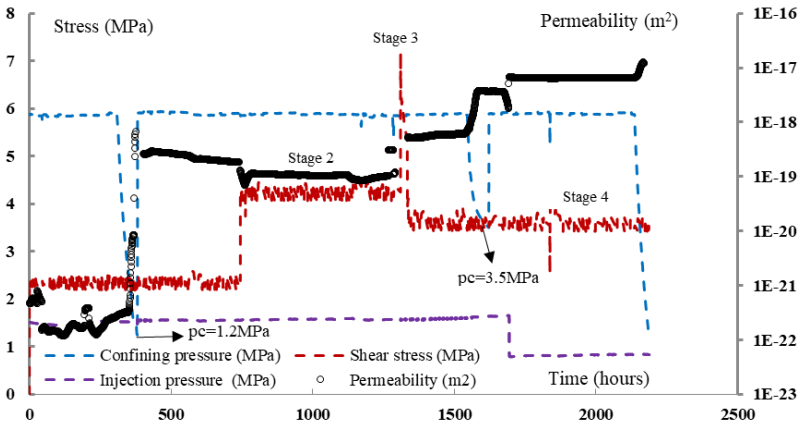

(b) the evolution relationship between shear stress, confining pressure, inject pressure and gas permeability with time

Figure IV .5: The evolution relationship of 6MPa shear creep test with sample C15

We could see there are two confining pressure drop points respectively at stage 1 and stage 4. FigureIV .6 and FigureIV .7 are partial enlarged view of FigureIV .5 for the two confining pressure decrease points. We can see at first confining pressure decrease point in FigureIV .6, the strain deformation change occurs later than confining pressure change which indicated before the confining pressure drops to 2MPa, a small amount of sheer deformation occurs, the internal pores are reopened, and the closed cracks are delated, but the sample structure remains intact, and the gas permeability increases slightly. When confining pressure continues to decrease, the sample occurs structural damage, a large number of new cracks are generated and penetrated, the gas permeability increases largely. At second confining pressure decrease point in FigureIV .7, there is no similar trend,

because the sample has been shear broken and the confining pressure decrease is not as large as the former point. No new cracks are generated, so at second point after as confining pressure is reloaded to 6MPa, most of the cracks closed again.

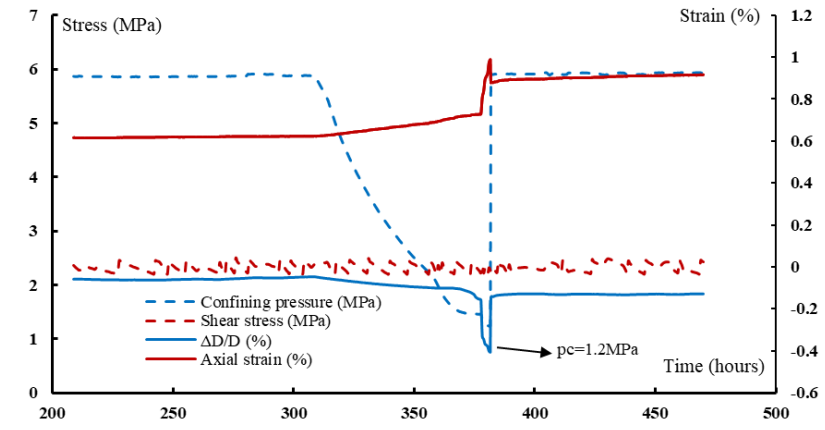

(a)

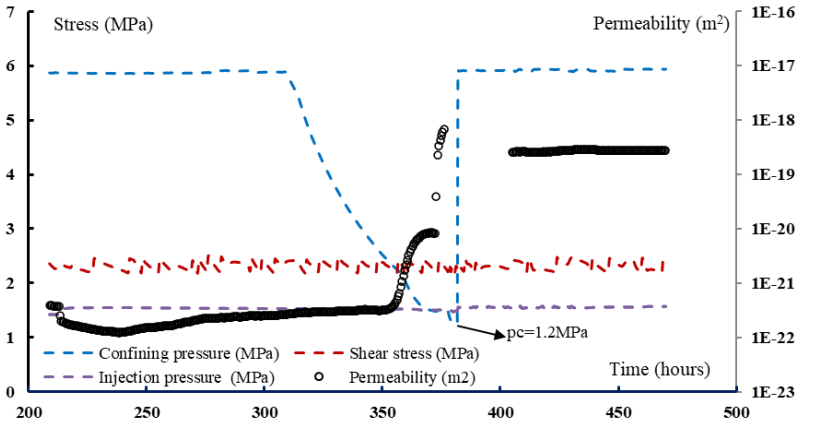

(b)

Figure IV .6: The partial enlarged view for first confining pressure decrease at stage 1

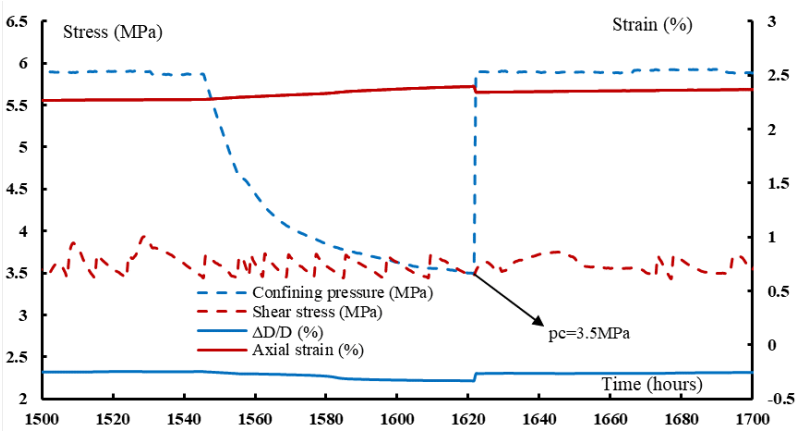

(a)

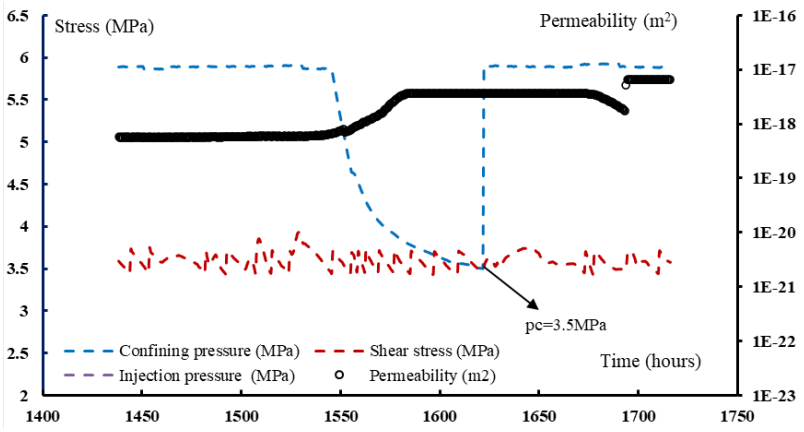

(b)

Figure IV .7: The partial enlarged view for second confining pressure decrease at stage 3

At initial stage, under 6MPa confining pressure, 2.38MPa shear stress(33.1% of peak stress) and 1.5MPa gas breakthrough pressure, gas permeability keeps as $1.2\times10^{-22}m^2$, then with the confining pressure drops to 1.2MPa, gas permeability increases to $2.53\times10^{-19}m^2$, then after confining pressure reloaded back to 6MPa, it slightly decreases. Even when shear stress loaded to 4MPa (60% of peak stress), this decrease trend continues, it indicates that the sample is compacted under 6MPa confining pressure. When sample turns to shear failure stage, gas permeability shows an obvious increase from $1.08\times10^{-19}m^2$ to $5.28\times10^{-19}m^2$, which indicates the sample is completely sheared broken. With shear stress unloaded to 3.55MPa (50.2% of peak stress), gas permeability slightly increases, and shows an obvious increase from $6.01\times10^{-19}m^2$ to $2.93\times10^{-18}m^2$ with confining pressure

drops to 3.5MPa. When confining pressure reloaded to 6MPa, gas permeability decreases to 1.73 X10-18 m2. Then with inject gas pressure decreases from 1.5MPa to 0.8MPa, gas permeability increases to 6.31×10^{-18}m^2, and it contains stable until test finishing.

3.2.2 Permeability measurement with confining pressure of 12MPa

For first shear creep test under 12MPa confining pressure with sample C16, the breakthrough pressure is 1.5MPa. For COx claystone samples, under higher confining pressure, the cracks and pores inside the sample are more constrained and closed. Therefore, the breakthrough pressure should be larger with confining pressure increases. However, for this sample, the breakthrough pressure is still 1.5MPa. And at initial stage, the gas permeability of C16 is even larger than it of C15. The permeability differences could probably be attributed to the initial structure difference, since gas permeability is sensitive to reflect the internal micro-cracks devolvement degrees. And sample C16 may have more inner micro-cracks.

FigureIV .8 shows the evolution relationship between shear stress and strain. The test is also divided into 4 stages, stage 1 is loaded 37.6% peak stress with intact sample, stage 2 is loaded 64.0% peak stress with intact sample, then the test enters shear failure stage as stage 3, and stage 4 is loaded 51.7% peak stress with fractured sample. Peak shear strength is 8.90MPa. FigureIV .9 shows the evolution of confining pressure, shear stress, deformation, injection pressure, and gas permeability with time.

For whole test, confining pressure is kept as 12MPa, at initial stage, under 12MPa confining pressure, 3.44MPa shear stress (37.6% of peak stress) and 1.5MPa gas breakthrough pressure, gas permeability shows an increase from 6.42×10^{-22}m^2 to 1.69×10^{-21}m^2, then it keeps constant for a short while, and decreases to 3.16×10^{-22}m^2. With shear stress loaded to 5.32MPa (64.0% of peak stress), gas permeability increases to 1.63×10^{-21}m^2, and it keeps slightly increase to 3.19×10^{-21}m^2 in this stage, then when sample is shear broken, gas permeability decreases to 2.40×10^{-21}m^2. When shear stress unloaded to 4.55MPa (51.7% of peak stress), gas permeability first slightly decreases to 1.66×10^{-21}m^2, then keeps constant. Then, with gas pressure increased from 1.5MPa to 5.5MPa step by step, gas permeability decreases to 2.78×10^{-22}m^2 m2, finally it shows a small increase to 4.82×10^{-22}m^2 and keeps constant until test finishing.

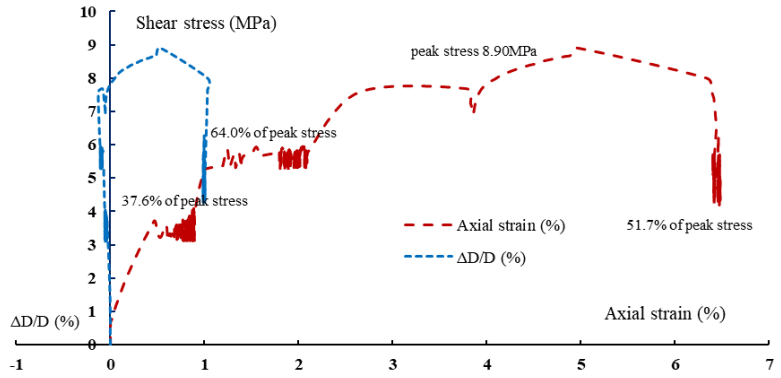

Figure IV .8: The evolution relationship between shear stress and deformation of shear creep test under confining pressure of 12MPa with sample C16

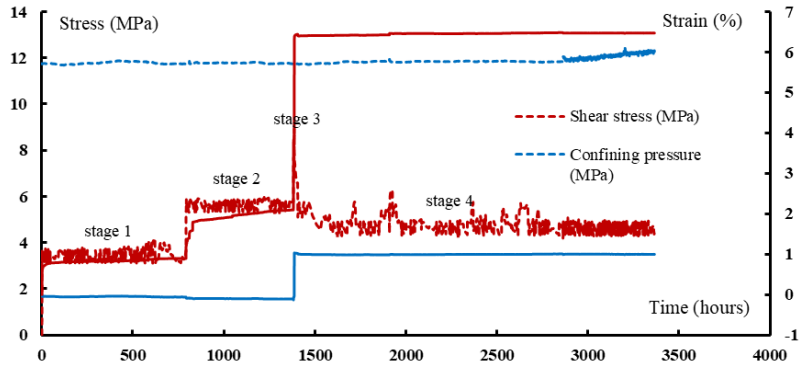

(a) the evolution relationship between shear stress, confining pressure and deformation with time

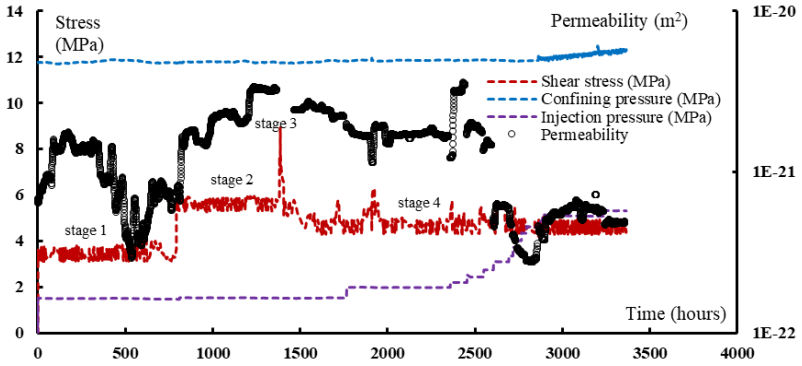

(b) The evolution relationship between shear stress, confining pressure, inject pressure and gas permeability with time

Figure IV .9: The evolution relationship of 12MPa shear creep test with sample C16

3.2.3 Verification test of Permeability measurement with confining pressure of 12MPa

For first 12MPa shear creep test with the C16 sample, its breakthrough pressure is small which seems to be attribute to its defects. In order to re-verify the above results, sample C17 is selected for second shear creep test under 12MPa confining pressure and the breakthrough gas pressure is determined as 5.5MPa. The test is carried out in a total of 5 stages, stage 1 is loaded 38.6% peak stress with intact sample, stage 2 is loaded 70.2% peak stress with intact sample, then the test enters shear failure stage as stage 3, and stage 4 is loaded 50.8% peak stress with fractured sample, stage 5 is loaded 78.4% peak stress with fractured sample, finally because the sample occurs large deformation, the shear stress is turned back to the stress state of stage 4. FigureIV .10 is the evolution relationship between shear stress and strain. The shear strength of sample C17 is 9.06MPa.

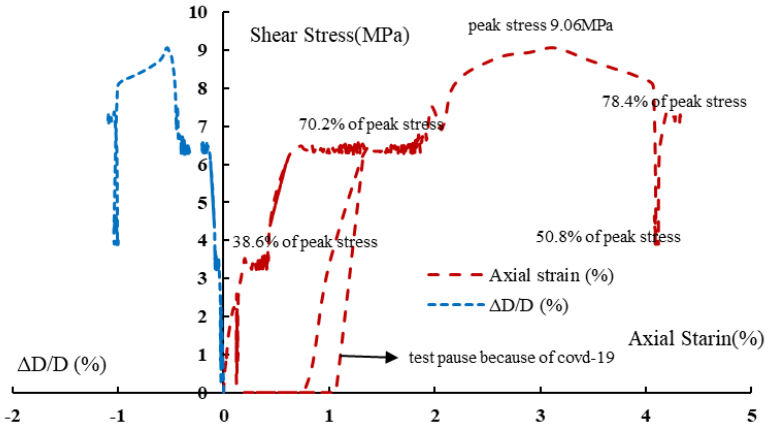

Figure IV .10: The evolution relationship between shear stress and deformation under confining pressure of 12MPa with sample C17

When the test progressed to stage 2, the laboratory is closed for 2 months because of the influence of Covid-19. In those 2 months, the collection system is closed, the shear stress is reduced to 0MPa and the confining pressure is reduced to 8.5MPa, and the injection air pressure is kept as 5.5MPa. When the laboratory is reopened, the confining pressure is restored to 12MPa. The shear stress is restored to 6.36MPa, and data collection is resumed. The pause has been marked in FigureIV .10.

For whole test, confining pressure and inject gas pressure is kept as 12MPa and 5.5MPa, respectively. At initial stage, under 12MPa confining pressure, 3.52MPa shear stress (38.6% of peak stress) and 5.5MPa gas breakthrough pressure, gas permeability keeps constant as $10^{-22}m^2$, when shear stress is loaded to 6.29MPa (70.2% of peak stress), gas

permeability decreases to $4.14\times10^{-23}m^2$, and keeps constant, from the figure we can see the pause induced by Covid-19 does not affect gas permeability evolution. When shear stress increases and sample occurs shear failure, the shear stress is unloaded to 3.94MPa (50.8% of peak stress), gas permeability shows a large increase from $2.79\times10^{-23}m^2$ to $1.81\times10^{-22}m^2$. When shear stress is increased to 7.07MPa (78.4% of peak stress), it continues to increase to $3.02\times10^{-22}m^2$ and quickly decreased to $1.71\times10^{-22}m^2$ as shear stress unloaded to 6.30MPa. Finally shear stress is unloaded back to 3.94MPa (50.8% of peak stress), and gas permeability shows almost constant, as a value ranging from $10^{-22}m^2$ to $3\times10^{-22}m^2$ until test finishing.

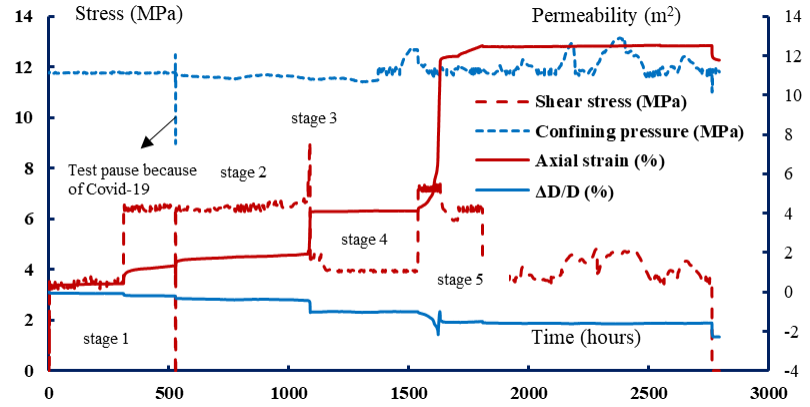

(a) the evolution relationship between shear stress, confining pressure and deformation with time

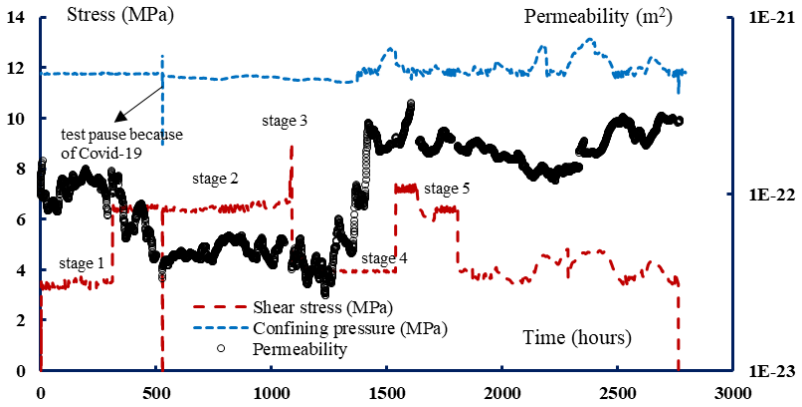

(b) the evolution relationship between shear stress, confining pressure, inject pressure and gas permeability with time

Figure IV .11: The evolution relationship of 12MPa shear creep test with sample C17

3.3 Experimental remarks

FigureIV .11 shows the evolution of the confining pressure, shear stress, gas permeability, axial deformation, and lateral deformation with time. The breakthrough gas pressure is 5.5MPa. By comparing the two samples C16 and C17 under same 12MPa confining pressure. We can find at initial stage, gas permeability of C16 is $6.42\times10^{-22}\mathrm{m}^2$ with 1.5MPa gas breakthrough pressure and C17 is $1\times10^{-22}\mathrm{m}^2$ with 5.5MPa gas breakthrough pressure. And for C16 the peak shear strength is 8.9MPa under 11.2MPa effective confining pressure(1.5MPa at the inlet end and 0.1MPa at the outlet end, so the average pore pressure is 0.8MPa), for C17 it is 9.06MPa under 9.2MPa effective confining pressure. Those results show that sample C17 is denser than sample C16, so even under sample stress condition, gas permeability evolutions in two tests are different.

4 Interpretation of results

4.1 Mechanical behaviour

4.1.1 Evolution of creep deformation

This study is divided into two parts to study the shear creep behaviours of COx claystone, including the creep behaviors of the intact specimen under shear stress (noted as stage 1 and stage 2 in the text) and the creep behaviours of the fractured specimen after shear failure (noted as stage 4 and stage 5).

For intact samples, from the test results showed in FigureIV .12, FigureIV .13 and FigureIV .14, the shear creep strains increase with the increase of the applied shear stress, and the values of axial and lateral strains the stage 2 are both higher than those of the stage 1. According to the shear strengths, the largest shear stress in stage 2 was only 70% of the strength among the three tests. Due to the low levels of applied shear stress, all the samples showed a stable creep tendency.

It was noted that there was a gradual decrease in the confining pressure in the first shear creep stage for the test under 6MPa confining pressure as FigureIV .12 shows, and that the confining pressure decreases to 1.2MPa, which results in significant shear strain and lateral dilatation of the sample. When confining pressure was reloaded to 6MPa, the shear deformation showed a smaller recovery, while the lateral strain showed obvious compressive deformation. This may be explained that the increase of confining pressure causes the dilated cracks formed to close under low confining pressure. However, the creep tendency of the 'failed' sample remained unchanged after the confining pressure was

reloaded to 6MPa.

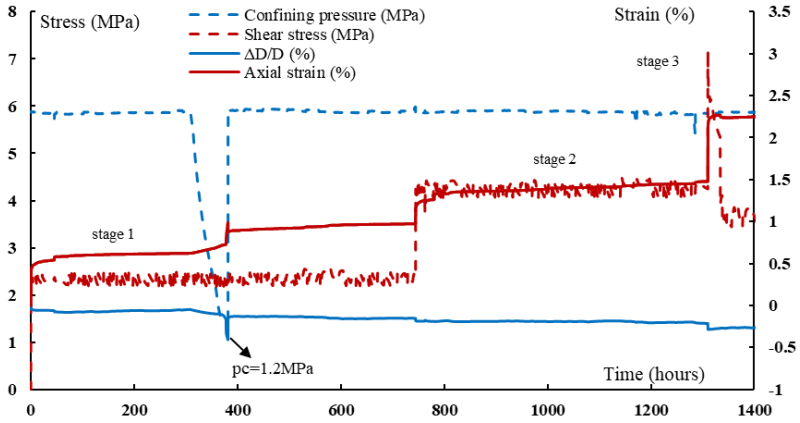

Figure IV .12: The former half part of evolution relationship between shear stress, confining pressure and deformation with time of C15

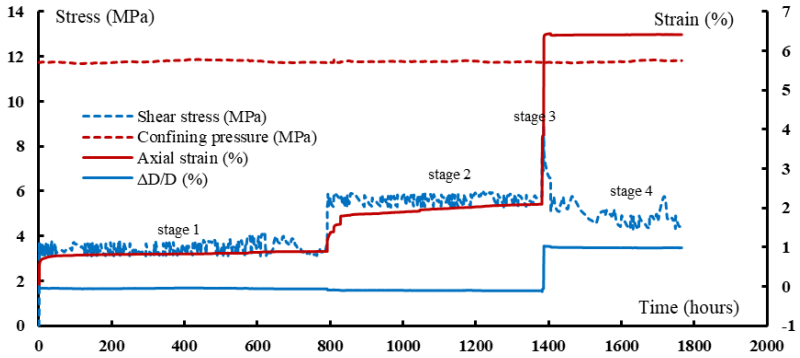

Figure IV .13: The former half part of evolution relationship between shear stress, confining pressure and deformation with time of C16

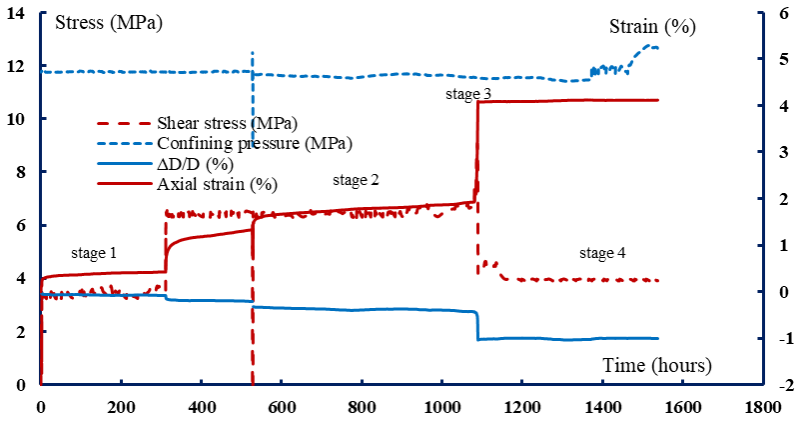

Figure IV .14: The former half part of evolution relationship between shear stress, confining pressure and deformation with time of C17

For fractured samples, from the test results showed in FigureIV .15, FigureIV .16 and FigureIV .17, when the specimen is shearing fractured, the shear stress was then reduced to 50% of the peak strength. The shear creep test (stage 4 and/or stage 5) was then carried out on fractured claystone. At the stage 4 of shear creep tests, both shear and lateral deformation were in a stable stage. Only in the stage 5 of the shear creep test under confining pressure of 12MPa (the verification test of sample C17 with confining pressure of 12MPa), the shear stress was 80% of the peak value. The sample showed significant shear and lateral creep strains. In order to ensure that the subsequent measurement could be continued, the shear stress was then reduced to 70%. From the test results, it can be seen that no significant creep strains (axial and lateral) can be observed on fractured samples when the applied shear stress is about 50% of peak shear strength. However, when the shear stress is increased to a level of 70% of the peak strength, large and unstable shear creep deformation will occur.

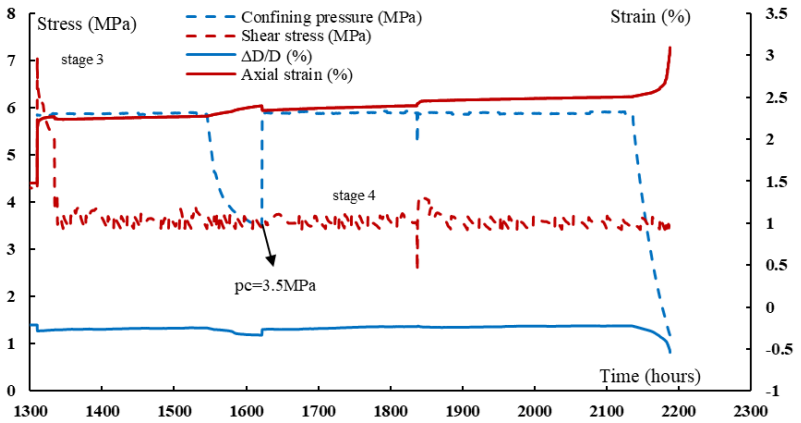

Figure IV .15: The latter half part of evolution relationship between shear stress, confining pressure and deformation with time of C15

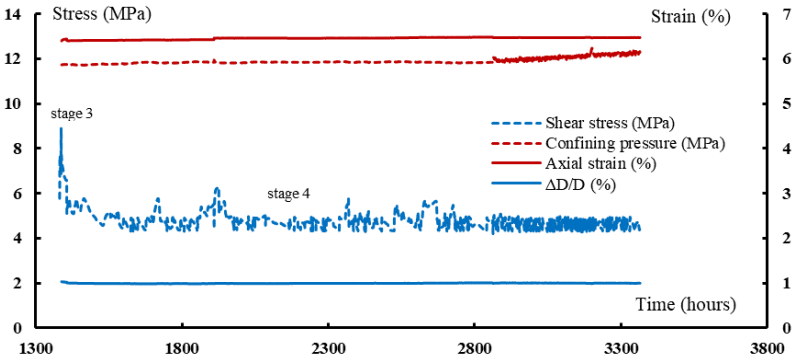

Figure IV .16: The latter half part of evolution relationship between shear stress, confining pressure and deformation with time of C16

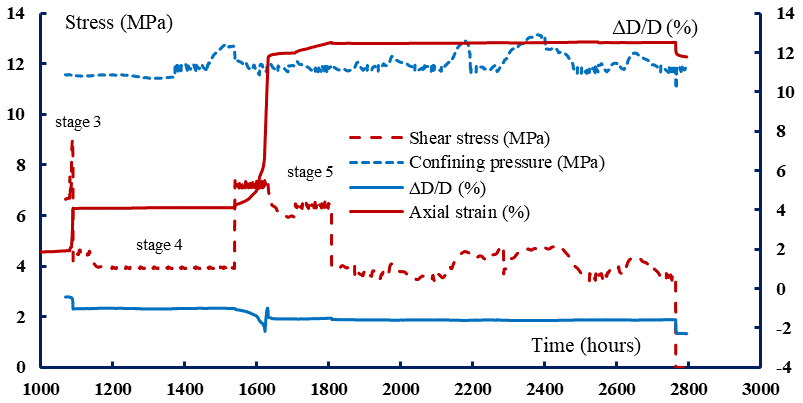

Figure IV .17: The latter half part of evolution relationship between shear stress, confining pressure and deformation with time of C17

4.1.2 Shear strength

As mentioned above, there was a confining pressure reduction process in the first stage of shear creep test under the confining pressure of 6MPa, which leaded to the failure of the sample. So, the applied shear stress can be taken as a value of shear strength at the lowest value of confining pressure. According to the effective stress concept, the shear failure strength are calculated and listed in the TableIV .3. In order to show the relationship between shear strength and confining pressure more intuitively, the relationship between them was drawn in the FigureIV .18. A linear relationship is clearly observed from the figure. It should be noted that the strength of the C16 sample is slightly lower than the fitted line, indicating that C16 has relatively low shear strength among the three samples. Even if the sample C15 failed due to reduction of confining pressure at stage 1, the strength value under confining pressure of 6MPa of C15 is still higher over the fitted line. At the same time, it is also observed that C16 has abnormal compression in the lateral deformation during shear failure. This phenomenon is difficult to give a convincing explanation, which requires more experimental observations.

*Note: the minimum value during decreasing stage of confining pressure.

Table IV .3: The shear failure strength with pressures parameters

Samples number	Confining Pressure (MPa)	Gas inject Pressure (MPa)	Effective confining Pressure (MPa)	Shear Strength (MPa)
C15	6	1.5	5.25	6.8
	1.2*	1.5	0.45	2.38
C16	12	1.5	11.25	8.92
C17	12	5.5	9.25	9.08

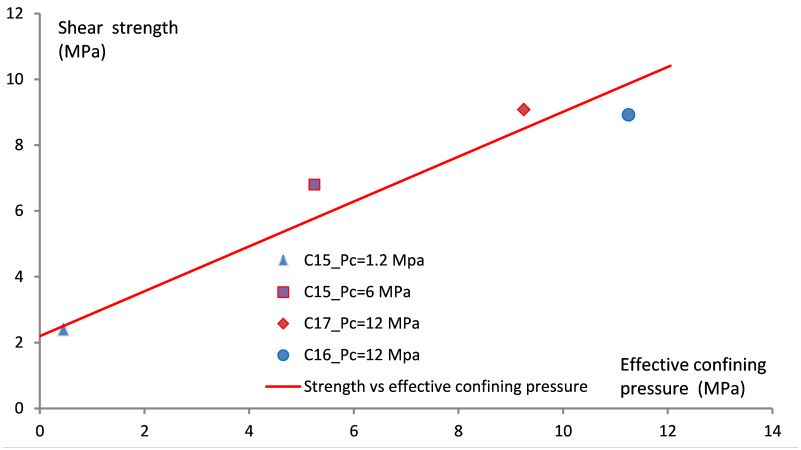

Figure IV .18: The relationship between failure strength and effective confining pressure

4.2 Evolution of permeability of claystone during shear creep

During the tests, the evolution of permeability is related to the applied shear stress, confining pressure and gas injection pressure, but its characteristics are far more complex than the evolution of deformation, and it exhibits greater dispersion.

4.2.1 Permeability evolution of intact sample

For the intact sample, from the test results showed in FigureIV .19, FigureIV .20 and FigureIV .21, the initial permeability of the sample at the stage 1 of shear creep loading is $1.2\times10^{-22}m^2$ for sample C15, $6.42\times10^{-22}m^2$ for sample C16 and $1.0\times10^{-22}m^2$ for sample C17. The results show that the permeability of sample C16 is the largest in three tested

samples, while the permeability for samples C15 and C17 are almost the same.

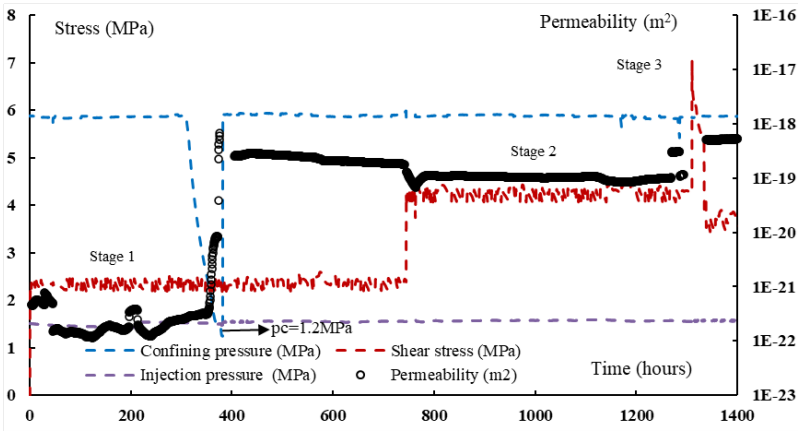

Figure IV .19: The former half part of evolution relationship between shear stress, confining pressure and deformation with time of C15

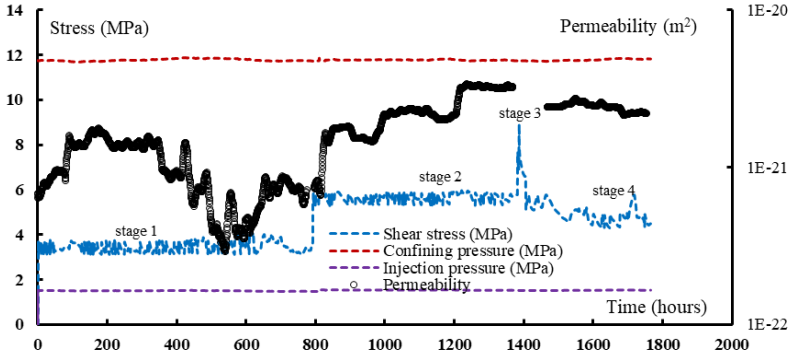

Figure IV .20: The former half part of evolution relationship between shear stress, confining pressure and deformation with time of C16

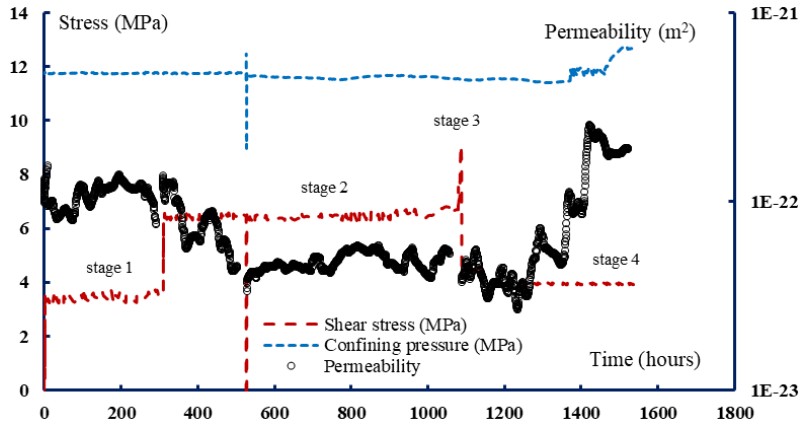

Figure IV .21: The former half part of evolution relationship between shear stress, confining pressure and deformation with time of C17

In stage 1, the permeability changes with time all fluctuated within its initial value range, and no obvious change trend was observed. The main explanation is that the samples were in the elastic state and that no obvious shear cracks were generated at stage 1, so the permeability was in a stable state.

As for the permeability evolution of the stage 2, the two tested samples under the confining pressure of 12MPa show opposite trends. Sample C16 showed a gradual increase trend in permeability, while sample C17 showed a significant decline in the beginning of stage 2, and then remained almost stable. However, for sample C15, the confining pressure decreased in the stage 1 of shear creep test, which leaded to shear failure of the sample under extremely low effective confining pressure. The fractured sample showed a sharp increase in permeability due to the shear failure and cracks dilatation. Even after the confining pressure was reloaded to 6MPa, the permeability showed a clear trend of decreasing with time, but the decrease in permeability was very small compared with the increase of permeability produced by shear failure due to the decrease of confining pressure.

Even in the stage 2 of shear creep test, the increase in shear stress did not change its tendency to continue to decrease slowly. Under the condition of higher confining pressure, for the permeability of fractured claystone damaged by shearing under extremely low confining pressure, the increase in permeability caused by the increase in confining pressure is more significant than the decrease in permeability caused by the increase in shear stress.

4.2.2 Permeability evolution of fractured sample

For the fractured sample, from the test results showed in FigureIV .22, FigureIV .23 and FigureIV .24, when the sample was failed by shear loading, the applied shear stress was reduced to 50% of the peak strength to perform permeability measurement under shear creep test. The permeability evolution in this stage (stage 4) for the two samples under the confining pressure of 12MPa shows an opposite trend. The permeability of fractured sample C16 was lower than that of intact sample in the stage 2 of shear creep test, and showed a trend of gradual decrease due to significant lateral compression; while the permeability of fractured sample C17 showed a stable trend in the beginning of stage 4, and then showed a significant increase. These seem to be consistent with their lateral deformation changes. But it needs to be emphasized that the permeability of fractured sample C16 at this stage is generally an order of magnitude higher than that of fractured sample C17. As for the fractured sample C17, when the shear stress increased to 80% of shear strength, the permeability increased significantly, and the evolutions of permeability and deformation were in good agreement. At this time, the sample showed obvious axial shear and lateral dilatation, which caused a significant increase in permeability. For the sample C15, after the confining pressure was reloading to 6MPa from the reduced value in creep stage 1, the permeability of sample C15 did not increase again until the shear failure under the confining pressure of 6MPa. When the creep shear stress was applied with the value of 50% of shear strength, the permeability of fractured sample C15 appears to be stable. When the confining pressure reduced, lateral dilatation was observed clearly, which resulted in a significant increase in permeability again. These all reveal the permeability sensitivity of fractured sample to confining pressure.

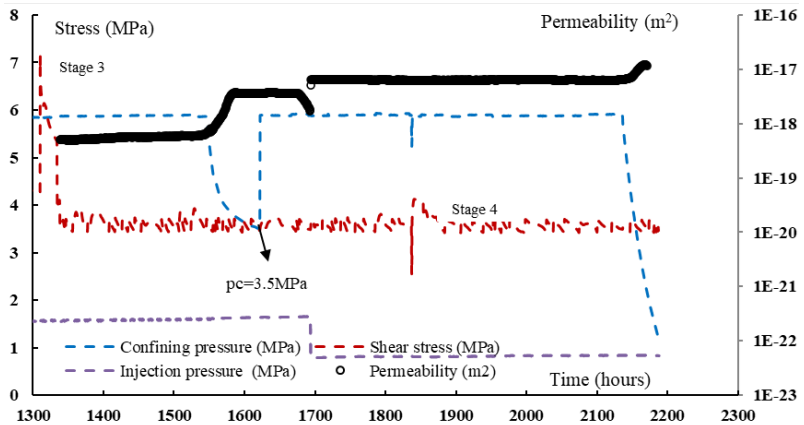

Figure IV .22: The latter half part of evolution relationship between shear stress, confining pressure and deformation with time of C15

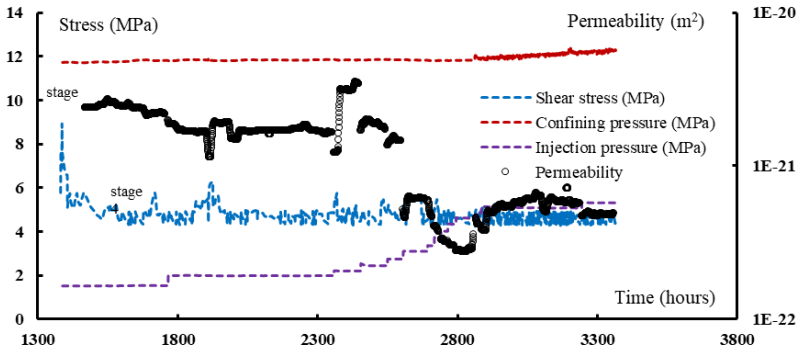

Figure IV .23: The latter half part of evolution relationship between shear stress, confining pressure and deformation with time of C16

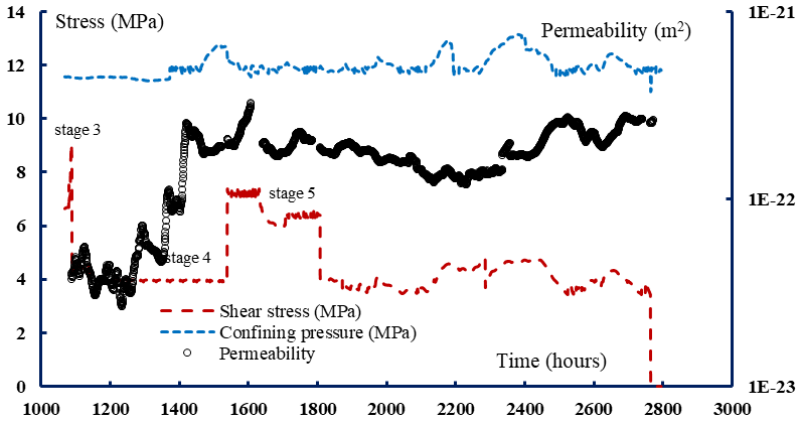

Figure IV .24: The latter half part of evolution relationship between shear stress, confining pressure and deformation with time of C17

4.3 Effects of confining pressure on the permeability of fractured sample

In this study, the permeability evolutions of two fractured samples, which were fractured by shear stress under confining pressure of 12MPa, were studied with the change of confining pressure. For the fractured samples C16 and C17, at first, the shear stress is completely unloaded, until the deformation becomes stable under the hydrostatic pressure of 12MPa. Then, the confining pressure is gradually reduced, and the gas permeability and/or lateral deformation (ΔD/D) are measured simultaneously. For the fractured sample C17, the permeability evolution with the confining pressure increase was also studied. The effect of confining pressure on the permeability of fractured claystone is generally shown as the increase of confining pressure causes the cracks to be compressed and closed, as a result, leads to partial closure or gas permeation channels reduce, thereby reduces the

permeability of the fractured claystone; in contrary to the increase of confining pressure, the decrease of confining pressure causes cracks to dilate and open, leads to partial connection of gas permeation channels, which leads to an increase in permeability of fractured claystone.

The test results reveal that the confining pressure has a significant effect on the permeability of the fractured claystone, and the relationship between them is not linear. FigureIV .25 shows the permeability evolution of the fractured sample C16 during the decrease of confining pressure. The results show that as the confining pressure decreases, the permeability gradually increases. Under higher confining pressure, the permeability increases slightly with decrease of confining pressure, while under lower confining pressure, the permeability increases clearly. The main reason is that under higher confining pressure, the crack dilatation is restrained, but under the condition of lower confining pressure, the crack is easy to dilate. In FigureIV .26, the lateral deformation is in good agreement with the permeability evolution. From a mechanism point of view, the permeability change is mainly affected by the lateral deformation.

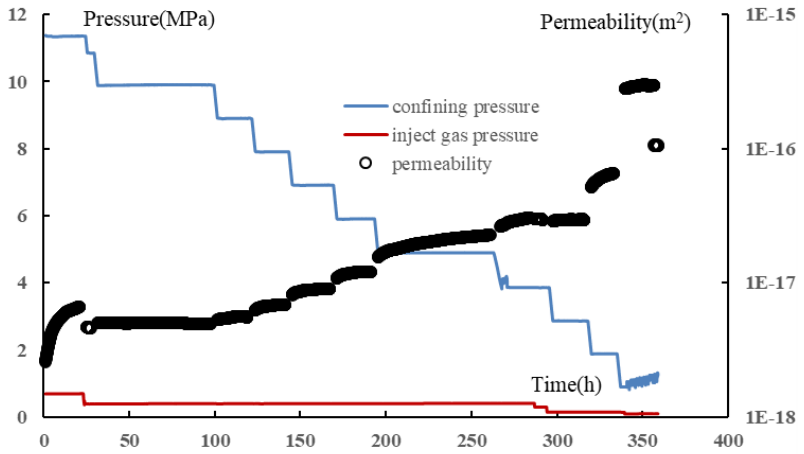

Figure IV .25: Evolution of gas permeability, confining pressure and gas pressure with time for fractured sample C16

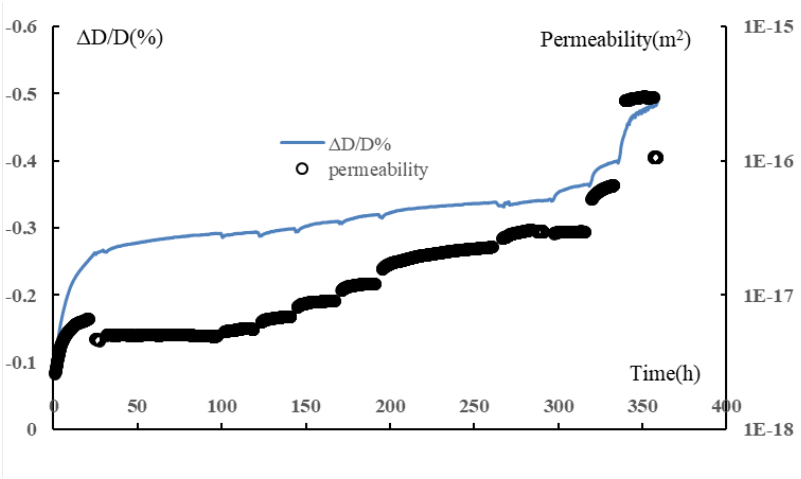

Figure IV .26: Evolution of gas permeability and ΔD/D% with time for fractured sample C16

As shown in FigureIV .27, for the fractured sample C17, as the confining pressure decreases, the permeability of fractured sample gradually increases. But the non-linear relationship between them is more significant by comparing with that of fractured sample C16. The increase in permeability is very small until the confining pressure drops to 6.5MPa, and then there is a significant increase.

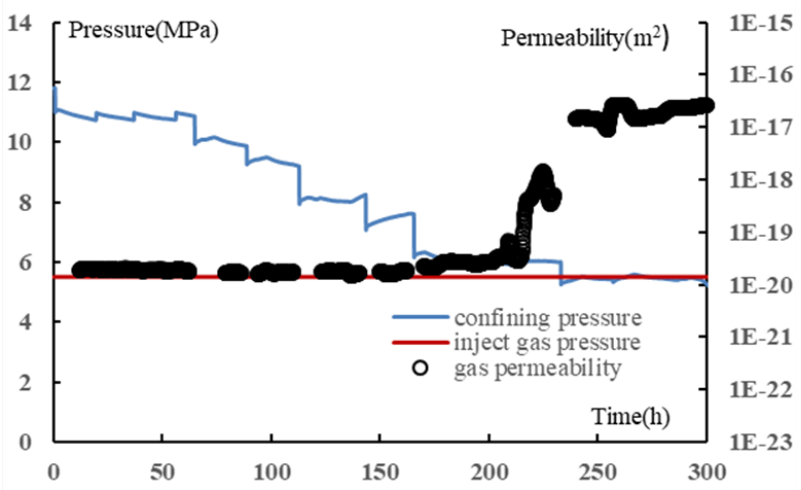

Figure IV .27: Evolution of gas permeability, confining pressure and gas pressure with time in unloading process for fractured sample C17

At the same time, this experiment also studied the permeability evolution of fractured sample C17 during the increase of confining pressure, as shown in FigureIV .28. The test results reveal that when the injection pressure is 1.5MPa and the confining pressure is

increased from 2MPa to 8MPa, the increase of confining pressure significantly reduces the permeability of the fractured sample under relatively low confining pressure. At a confining pressure of 8MPa, when the injection pressure increases from 1.5MPa to 5.5MPa, the increase in injection pressure causes an increase in permeability. This can be explained from two aspects. One is that the increase in injection pressure causes a decrease in term of effective confining pressure. The decrease of effective confining pressure causes the permeability to increase; and the other is due to the increase in injection pressure, which causes the measured permeability to decrease according to the Klinkenberg effect. In this stage, the permeability increases clearly, indicating that the combined effect of these two aspects is controlled by the effect of effective confining pressure. This study is not interested in the Klinkenberg effect, but in the permeability evolution under higher confining pressure.

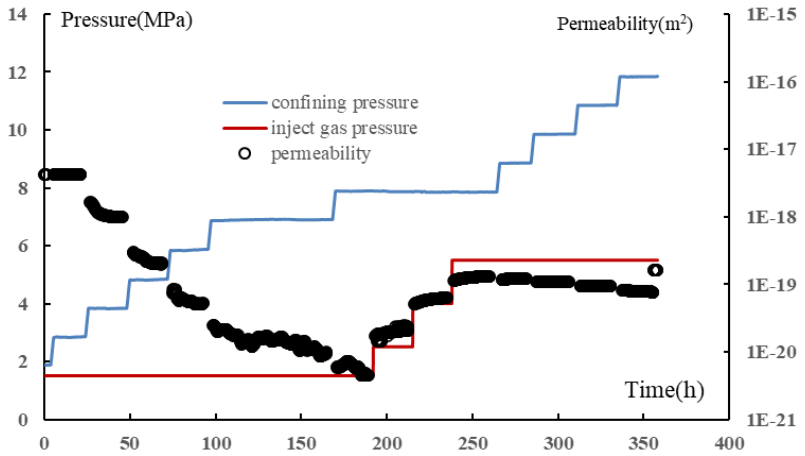

Figure IV .28: Evolution of gas permeability, confining pressure and gas pressure with time in loading process for fractured sample C17

In FigureIV .28, it can be found that when the injection pressure is 5.5MPa and the confining pressure increases from 8MPa to 12MPa, the increase of confining pressure only slightly reduces the permeability of the fractured sample. The effective stress description can better illustrate this trend, as shown in FigureIV .29. Since the lateral deformation ring exceeds the measurement range during this stage, the relationship between lateral strain and permeability cannot be given, but it can be reasonably deduced as being consistent with the result obtained by C16.

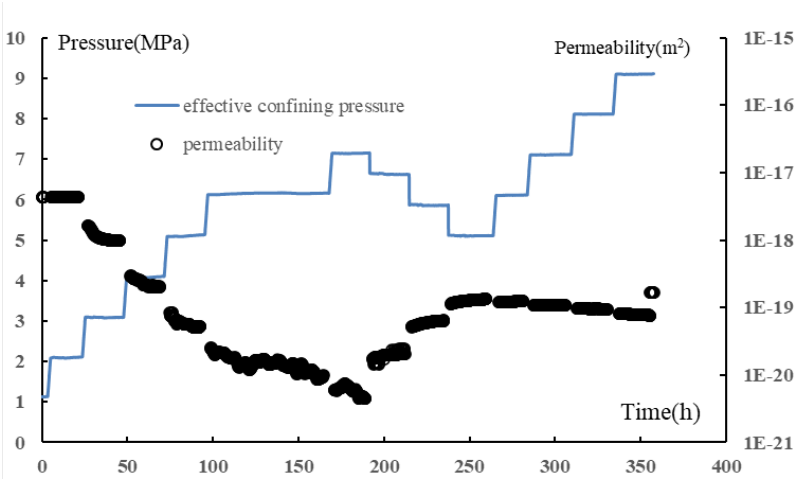

Figure IV .29: Evolution of gas permeability and effective confining pressure with time in loading process for fractured sample C17

So from FigureIV .25, FigureIV .28 and FigureIV .29, the effective confining pressure-gas permeability as well as inject gas pressure curves could be obtained, which showed in FigureIV .30,FigureIV .31 and FigureIV .32, respectively.

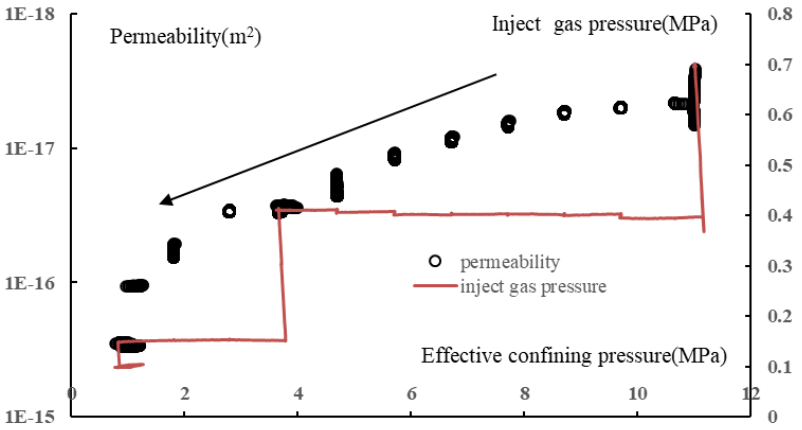

Figure IV .30: Effective confining pressure-gas permeability as well as inject gas pressure curves for fractured sample C16

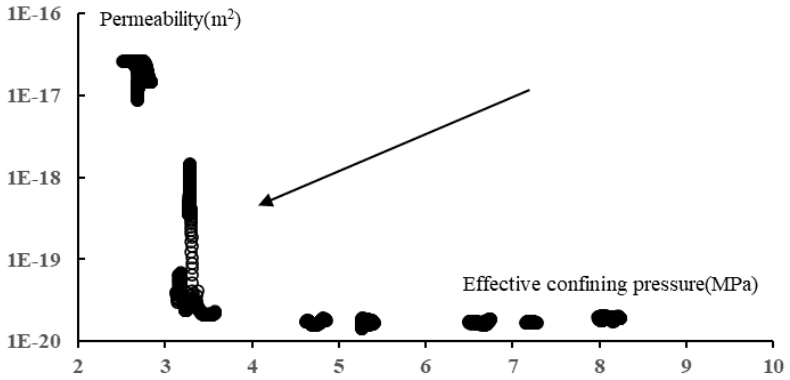

Figure IV .31: Effective confining pressure-gas permeability curves with unloading process for fractured sample C17 with constant inject gas pressure 5.5MPa

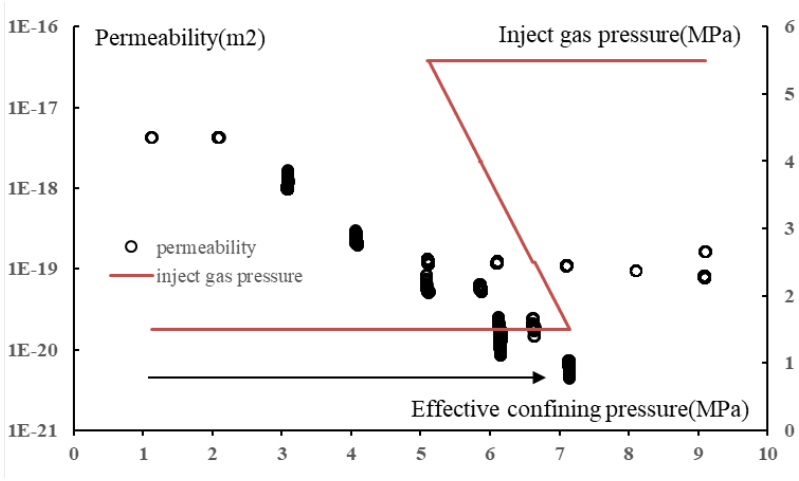

Figure IV .32: Effective confining pressure-gas permeability as well as inject gas pressure curves with reloading process for fractured sample C17

From FigureIV .30 and FigureIV .31 we could see when confining pressure decreases, gas permeability firstly increased slightly. When effective confining pressure is smaller than 4MPa, there exists an obvious permeability increase. It seems 3-4MPa is a sensitive state for confining pressure. When confining pressure is larger than it, the pre-existing cracks are closed and COx claystone shows self-sealing ability. When confining pressure is smaller than it, the cracks are reopened and it induces a large permutability increase.

From FigureIV .32 we could see when confining pressure increases, there shows an obvious decrease for gas permeability with 4MPa effective confining pressure, and when effective confining pressure is larger than 8MPa, gas permeability decreases slightly. Thus, for these results, we could obtain that the 4MPa confining pressure seems to be a sensitive

stress state for cracks open and closed, when confining pressure is larger than 8MPa, the micro cracks are closed completely and COx claystone shows self-sealing ability.

5 Concluding remarks

The following conclusions were obtained from the tests performed in this chapter:

(1) For rock mechanical properties, when shear stress increased, the rock compressed axially and dilated laterally, and the sample deformation (axial and lateral) increased with shear stress increase and confining pressure decrease. For intact samples, due to the low levels of applied shear stress, all samples showed a stable creep tendency. For fractured samples, no significant creep strains (axial and lateral) were observed for the fractured samples when the applied shear stress was approximately 50% of peak shear strength. However, when the shear stress was increased to 70% of peak strength, large and unstable shear creep deformation occurred. The shear failure strength was enhanced as the confining pressure increased. When the shear stress was kept constant, the decrease of the confining pressure caused plastic shear deformation. The strength of the C16 sample was slightly lower than the fitted line, indicating that C16 had relatively low shear strength among the three samples. In addition, C16 had abnormal compression in the lateral deformation during shear failure. This phenomenon was difficult to explain, and further studies are required.

(2) Gas permeability evolution was related to the applied shear stress, confining pressure, and gas injection pressure, but its characteristics were more complex than the evolution of deformation, and exhibited greater dispersion. For gas permeability evolution with intact samples, as the internal pores and cracks of the sample were closed under high confining pressure, the gas found it harder to break through the sample. The gas permeability decreased as the confining pressure increased. For samples with obvious internal micro-cracks, the increase in shear stress led to a larger gas permeability trend. For denser samples, the increase in shear stress led to a smaller gas permeability trend. The reason for this phenomenon might be caused by the microstructure of the two samples. However, the experimental results did not fully support this hypothesis.

(3) For gas permeability evolution with fractured sample, the gas permeability evolution after the shear failure stage were consistent with their lateral deformation changes. For the permeability of fractured claystone damaged by shearing under extremely low confining pressures, the increase in permeability caused by the increase in confining pressure was more significant than the decrease in permeability caused by the increase in

shear stress. In the gas permeability evolution with confining pressure under hydrostatic state with fractured sample, we found that as the effective confining pressure increased, gas permeability decreased as the cracks were compressed and closed, which led to partial closure or reduction in the gas permeation channels. The decrease of the confining pressure caused the cracks to dilate and open, which led to a partial connection of gas permeation channels, and an increase in the permeability of fractured claystone. The relationship between gas permeability and effective confining pressure was not linear. Under higher confining pressure, the permeability increased slightly with a decrease of confining pressure, whereas under lower confining pressure, the permeability increased, and the lateral deformation was in good agreement with the permeability evolution. Therefore, the permeability change was mainly affected by the lateral deformation.

Chapter V

Poromechanical Behaviors of COx claystone

1 Introduction

COx claystone contains complex networks of pores that are saturated by different interstitial fluids and subjected to significant changes of fluid pressure in natural rock structures. Inside the rock, the pores are filled with one or several fluid phases and the rocks are commonly taken as the sealed bulkhead layer. Water saturation induces a capillary effect and contributes to the modification of the microstructure. In the short-term, water saturation decreases the yield stress and the failure strength of the equivalent solid matrix due to the decrease of the capillary force in the liquid contact. In the long-term, water saturation enhances the dissolution process of the cemented contact and emphasizes the time-dependent strains. The macroscopic elastic and plastic deformations are influenced by variation in the interstitial pressures. Therefore, the safety requirements for underground disposal require an extensive investigation of the poromechanical behavior of the host rocks .

For elastic porous materials, the pioneer works by(Biot, 1941, 1973) founded the fundamental theory of poroelasticity. This theory has been reformulated in the thermodynamics framework of open systems by (Coussy, 1995, 2004). The poroelastic theory has been largely used in engineering applications and extended to anisotropic materials (Cheng, 1997; Lydzba and Shao, 2000; Shao, 1998). Recently, several experimental investigations have been performed for various clayey rocks under different satu-rated conditions (Bemer et al., 2004; Charlier et al., 2013; Fityus and Buzzi, 2009; Hoxha et al., 2007; Hu et al., 2014; Liu, 2016; Zhang and Rothfuchs, 2004; Zhang et al., 2014b) . These previous studies

have shown that the macroscopic failure stress decreases and the clayey rocks become more ductile when water increases, such as the elastic modulus and failure properties. Further, the mechanical behavior of COx claystone is highly sensitive to pore fluid. Water saturation could induce pore collapse and substantial plastic deformation. Similar studies have examined the influence of water content on the mechanical behaviors of other types of rock materials, such as shale rocks (Eseme et al., 2006; Valès et al., 2004), clay-bearing sandstone (Soe et al., 2010), and chalk (Hellmann et al., 2002; Schroeder, 2007; Xie and Shao, 2006).

With increasing depth beneath the soil, the mineralogical composition and pore properties of clayey rocks are different, which have been confirmed via experimental investigations in the laboratory to have a significant influence on mechanical behaviors (Bornert et al., 2010; Robinet et al., 2012; Zhang, 2011). The results showed that to understand the correlation between macroscopic behaviors and microstructure, it was necessary to investigate the poromechanical and hydromechanical properties to recognize the deformation mechanism.

However, differences were noted in the existing results on poroelastic properties and poroplastic behavior has rarely been investigated to date. There remains great uncertainty regarding the variation in pore pressure, and the analysis of COx claystone requires consideration of coupling between rock deformation and interstitial pressure variation because the effective pressure variation could be a key factor for the COx claystone cracking mechanism under coupled stresses. Thus, as part of their new research program, Lamcube proposes to undertake experimental studies to investigate the poromechanical coupling properties of COx claystone. The topic of the present chapter was to verify the existence and validity of the effective stress principle in elastic and plastic domain for saturated COx claystone.

In the elastic domain, the effective stress concept of saturated soil was proposed by Terzaghi, namely:

$$\sigma' = \sigma - p \tag{V .1}$$

Where, σ' is the effective stress and p is the pore pressure.

In rock mechanic studies, Biot's elastic pore theory framework was proposed to study the physical and mechanical changes of rocks caused by rock pore deformation during the seepage-stress coupling process (Skempton, 1954). The theoretical framework for the mechanical saturated porous media was founded by Biot's theory in studying three-dimensional soil consolidation (Biot, 1973). The constitutive models for saturated media

were then extended to partially saturated media using Bishop's effective stress principle (Bishop and Blight, 1963). Biot, Skempton, and Bishop improved the effective stress formula based on Terzaghi's research (Biot, 1956, 1962; Bishop, 1959; Skempton, 1984). Under the current theoretical framework of porous media elasticity, the effective stress can be expressed as follows:

$$\sigma' = \sigma - bp \tag{V .2}$$

Where, b is Biot's coefficient.

Biot's coefficient is an important parameter in pore elastic properties, reflecting the influence of the internal pore structure on the overall properties of rocks. For rock material, Biot's coefficient is mainly determined by the material pore structure and changes with the expansion, extension and penetration of pore cracks. The effective stress concept is used in hydro-mechanic coupling studies, where it is difficult to determine Biot's coefficient.

Thus, several studies have been conducted to determine Biot's coefficient. (Charlez and Heugas, 1992) used the bulk modulus drained and undrained sandstone conditions to determine Biot's coefficient. The study showed that Biot's coefficient of the Voges sandstone was in the range of 0.6-0.9, and found that the method of calculating coefficients was reliable only when the modulus difference was large enough. In (Murphy et al., 1993)'s study, the volume modulus of the pore fluid of pure quartz sandstone was obtained via acoustic wave velocity inversion and Biot's coefficient was determined from the volume frame modulus and shear frame modulus. The study found that Biot's coefficient of the pure quartz sandstone changed in the range of 0.5-0.8. In addition, the temperature effect on the pore elastic parameters of the sandstone was studied by the triaxial compression test (Hassanzadegan et al., 2012). The study showed that Biot's sandstone coefficient changed within the range of 0.5-0.9 and decreased with an increase in the effective stress and temperature. (Shao, 1998) established a relationship between the anisotropic Biot's coefficient and the damage variable. Based on (Shao, 1998)'s Biot's coefficient calculation method, (Hu et al., 2009) measured and calculated the axial and lateral Biot's coefficient during the failure stage of marble and obtained the evolution law of axial and lateral Biot's coefficient with deformation under different confining pressures with deformation.

For COx claystone, (Escoffier, 2002) and (Homand et al., 2006) found Biot's coefficient was determined as 0.55-0.95. (Homand et al., 2004) used pulse-tests and sample variation and measured Biot's coefficient value as 0.75. Based on previous studies, (Cariou et al., 2012) used drained uniaxial compression tests and triaxial change in pore pressure poromechanical measurement test to recalculate Biot's coefficient for COx claystone. From his

test results, Biot's coefficient value equaled 1. (Bemer et al., 2004) used water as the injected fluid to saturate the COx claystone and proposed a series of tests to obtain Biot's coefficients for different directions, which was measured as 1 in the parallel direction to bedding and 0.9 in the perpendicular direction to bedding. (Yuan et al., 2017) proposed a complete poromechanical study for COx claystone to determine Biot's coefficient for samples under different relative humidities with a new gas injection technique to avoid water control difficulties and Biot's coefficient value was determined to be greater than 1.

Therefore, Biot's coefficient determined by previous studies has shown an exceptionally large range. The Biot's coefficient measured test for COx claystone, as a low permeability material, is extremely difficult under a fully saturated condition and a stable deformation environment. Therefore, to study the reduction of effective stress by pore pressure inside saturated COx claystone, it is necessary to redetermine Biot's coefficient of COx claystone using a more sophisticated method.

Skempton coefficient is also measured, and is defined as the ratio of the pore pressure change to the mean stress change under undrained conditions. It is an important pore fluid parameter and the bridge between contact pressure and mean stress.

Specific poroplastic coupling tests with poromechanical cycles were undertaken using lateral decompression and axial extension loading path, the mechanism of which has been elaborated in ChapterIII . The objective was to verify the existence and validity of the effective stress principle in the plastic domain for the saturated COx claystone.

Oedometric tests under different drainage conditions were proposed with the measurement of pore pressure evolution. The oedometric test is a type of geotechnical investigation performed in geotechnical engineering that measures the consolidation properties of soil and rock. Oedometric tests were performed by applying different loads to a sample and measuring the deformation response. The results from these tests were used to predict how a soil or rock in the field will deform in response to a change in effective stress, and can also be applied to measure the poroelastic parameters. For COx claystone, (Vincké et al., 1998) performed many oedometric tests with loading-unloading cycles under drained conditions at a constant pore pressure. (Bemer et al., 2004) calculated the oedometric modulus as 1-5GPa with an effective axial stress from 5 to 25MPa. Using a series of oedometric drained tests, (Homand et al., 2006) obtained the oedometric modulus as 1.4-6GPa with an axial stress of 2-24MPa. All these values obtained from these tests were under the condition of axial stress below 25MPa and the results showed discreteness attributes to various facts such as the natural structural anisotropy, saturated degree, and experimental condition. In this chapter, an oedometric test was proposed as this type of test is useful

for the validation of constitutive models for saturated rocks.

Therefore, in this chapter, we investigated the poromechanical coupling properties of COx claystone. Three groups of new tests were performed. First, different loading paths were considered to measure Biot's and Skempton coefficients. Second, specific poroplastic coupling tests with poromechanical cycles were performed to verify the existence and validity of effective stress principle in plastic domain. Third, oedometric tests under different drainage conditions were undertaken to measure pore pressure evolution.

2 Material and experimental program

In this chapter's tests, samples are drilled from number EST55522, EST58123, EST60710 and EST60788 rock cores. The steps are almost same with those in ChapterIII . In total, seven samples are finally prepared with different lengths and diameters as given in TableV .1. For all samples in this chapter, the saturation process is essential before tests.

The apparatus used in axial extension test with poromechenical cycles is the same apparatus used in creep tests in ChapterIII . For Biot and Skempton coefficient measuring tests, lateral decompression test with poromechanical cycles and oedometric tests, autonomous and auto compensated hydromechanical coupling system (FigureV .1) designed at the Laboratory of Mechanics of Lille (LML) is used. The testing system consists of four components, three for deviator stress loading, confining pressure application and interstitial pressure generation, these three components are assembled around the triaxial cell, and the fourth thermal loading component is independent of the former three ones and is assured by a regulated oven located in a room for which the temperature is regulated at 20 ± 0.5^{o}C by an air conditioner. An inner force sensor is incorporated in the cell to measure the axial load acting on the sample to eliminate the friction effect of loading piston on the calculation of axial stress. The pressure sensors are placed outside the heating oven to avoid temperature interference.

The axial and lateral strains of samples are measured by two pairs of strain gages. Furthermore, they can also be measured by two axial LVDTs and a radial strain ring. The pore fluid drainage circuit is connected to the outside of the heating oven by steel tubes of 1.5mm in inner diameter and about 2m in length. For additional information, the measurement range of all components used in tests is checked and suitable for the quantity's studies. The force sensor has a measurement range of 6kN and an accuracy of $\pm$6N; the pressure sensor has a measurement range of 20MPa and an accuracy of $\pm$0.02MPa;

the LVDT has a measurement range of ±3 mm and an accuracy of ±0.01mm; the strain gage has a measurement range of $\pm 2.10^{-2}$ and an accuracy of $\pm 2.10^{-6}$. All those data are recorded by a data acquisition center. All tests are carried out in a thermally isolated small room with the constant temperature maintained throughout the experiments.

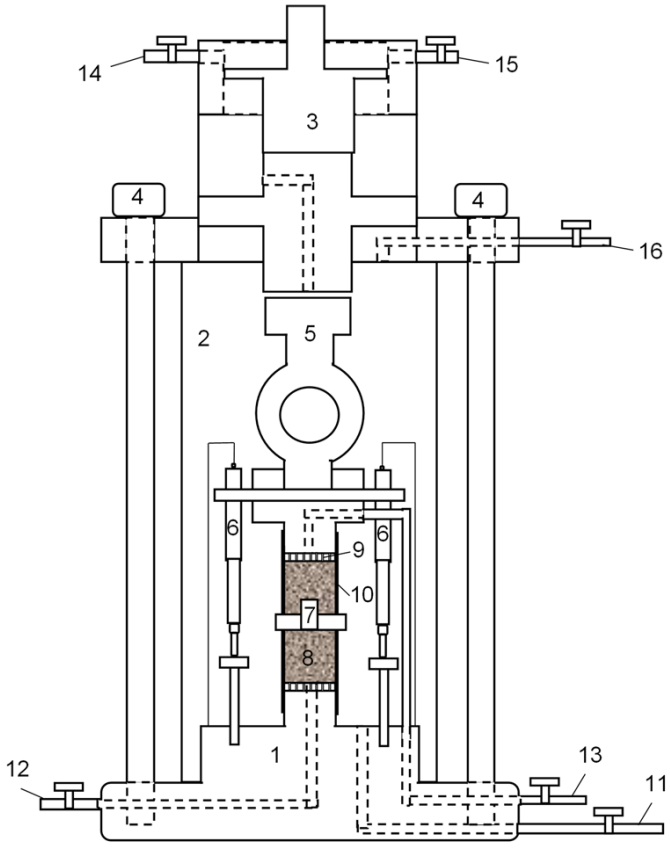

1-Device base; 2-Confining pressure chamber; 3- Axial loading component; 4-Strap; 5-Internal force sensor; 6-LVDT; 7-Ring; 8-Specimen; 9-Drainage disc; 10-Plastic seal; 11-Confining pressure application pipe; 12-Pore pressure injection pipe; 13-Back pressure injection pipe; 14-Axial force loading pipe; 15-Axial pressure sensor; 16-Confining pressure sensor

Figure V .1: Sketch of experimental apparatus

It should be noted that, for Biot's and Skempton coefficient measurement tests as well as oedometric tests, the the axial and lateral strains are measured by strain gages. For lateral decompression and axial extension tests, the LVDTs and a radial strain ring are used to measure the axial and lateral strains.

Also, for all tests mentioned in ChapterV the saturation step is necessary. Before formal test, the sample is applied 10MPa confining pressure and injected synthetic formation water of Andra, which is used to prevent structural property change. The inject pore

pressure is 2MPa and the whole process would be contained for four weeks. Then open both pore pressure pipes to exclude the remaining gas inside the sample, then close the pipes and increase pore pressure to 2MPa again. Then contain the stress state for at least two days until the deformation turns to be stable. After all these steps the samples are thought to be fully saturated. The chemical composition of synthetic formation water is shown in TableV .2.

Table V .1: Sample geometry and testing condition

Samples number	Moisture Content ω	Diameter mm	Lenth mm	Loading Rate MPa/min	Test Style
EST55522 C7 90°	6.40%	19.87	19.60	0.02	Biot Coefficient Measure
EST58123 C8 90°	7.12%	34.55	24.87	0.02	Skempteon Coefficient Measure
EST60788 C9 90°	7.02%	37.01	34.22	0.01	Lateral Decompression
EST55522 C10 90°	6.40%	37.21	29.17	0.01	Axial Extension
EST60710 C11 90°	6.20%	36.20	32.02	0.01	Axial Extension
EST58123 C12 90°	7.12%	36.59	30.32	0.01	Oedometric Drained
EST58123 C13 90°	7.12%	34.55	24.87	0.01	Oedometric Undrained

Table V .2: Chemical composition of synthetic formation water of Andra

Compound	NaCl	$NaHCO_3$	KCl	$CaSO_4,2H_2O$	$MgSO_4,7H_2O$	$CaCl_2,2H_2O$	Na_2SO_4
g/L	1.950	0.130	0.035	0.630	1.020	0.080	0.700

3 Determination of Biot's coefficient and Skempton coefficient

3.1 Determination of Biot's coefficient

In (Nur and Byerlee, 1971) Biot's coefficient is measured as below:

$$b = 1 - \frac{K_b}{K_s} \tag{V .3}$$

Here, b is Biot's coefficient; K_s is the solid matrix bulk modulus and K_b is the skeleton bulk modulus.

Through this method, the confining pressure should be loaded at a constant rate under drainage conditions, and K_b is calculated by the slope of the stress-strain curve, then the confining pressure should be loaded at the same rate under undrained conditions, K_s is calculated by the slope of the stress-strain curve to obtain Biot's coefficient. However, the drainage method based on the triaxial compression experiment cannot measure Biot's coefficient of low-porosity and low-permeability rock, and COx claystone is a low permeability, high self–closing property, and poor seepage capacity material, so this method is not suitable for COx claystone. Therefore, we uses the hierarchical loading method to measure Biot's coefficient according to (Sibai, 1990; Tennis and Jennings, 2000). The formula is:

$$b = K_b/H = \frac{\Delta\sigma/\Delta\varepsilon_v}{\Delta P_i/\Delta\varepsilon_{vp}} \tag{V .4}$$

$\Delta\sigma$ is stress increment, ΔP_i is pore pressure increment, $\Delta\varepsilon_v$ is volume strain increment caused by $\Delta\sigma$, $\Delta\varepsilon_{vp}$ is volume strain increment caused by ΔP_i.

The experimental scheme is as follows:

(a). Load sample and perform saturation step during 6-8 weeks, then load confining pressure to 14MPa and pore pressure to 4.5MPa.

(b). When the deformation keeps stable, keep confining pressure constant, slowly increase pore pressure to 7.5MPa with the rate of 0.02MPa/min and keep the stress state constant for at least three days until the deformation is stable. Then reduce pore pressure to 4.5MPa slowly with the rate of 0.02MPa/min, and keep the stress state constant for at least three days until the deformation is stable.

(c). Keep pore pressure constant, slowly reduce confining pressure to 11MPa with the rate of 0.02MPa/min and keep the pressure constant. Then keep the stress state for at least three days until the deformation is stable. Then increase confining pressure to 14MPa

with the same rate, keep the stress state for at least three days until the deformation is stable; then determine Biot's coefficient through step(b)-(c).

(d). When the deformation keeps stable, then keep the confining pressure constant, slowly decrease pore pressure to 1.5MPa with the rate of 0.2Bar/min and keep the stress state constant for at least three days until the deformation is stable. Then increase pore pressure back to 4.5MPa slowly with the same rate of 0.02MPa/min, and keep the stress state constant for at least three days until the deformation is stable.

(e). Keep pore pressure constant, slowly increase the confining pressure to 17MPa with the rate of 0.02MPa/min and keep the pressure constant. Then keep the stress state for at least three days until the deformation is stable. Then decrease confining pressure to 14MPa with the same rate, keep the stress state for at least three days until the deformation is stable; then determine Biot's coefficient through step(d)–(e).

(f). Increase the confining pressure to 22MPa and select a new starting point after it stabilizes, then repeat steps(b)–(e) and determine Biot's coefficient.

Through the specific steps we could found the confining pressure increment is equal to pore pressure increment, $\Delta\sigma$=ΔP_i. Therefore, FormulaV .4 is simplified to:

$$b = \Delta\varepsilon_{vp}/\Delta\varepsilon_v \tag{V .5}$$

Thus, two loading paths are considered for Biot's coefficient measuring test. One path for effective pressure reduced(steps(b)–(c)) and another for effective pressure increased(steps(d)–(e)). Each path could obtain two Biot's coefficient value respectively for loading cycle and unloading cycle.

FigureV .2 is simplified flowchart to help better understand the steps.

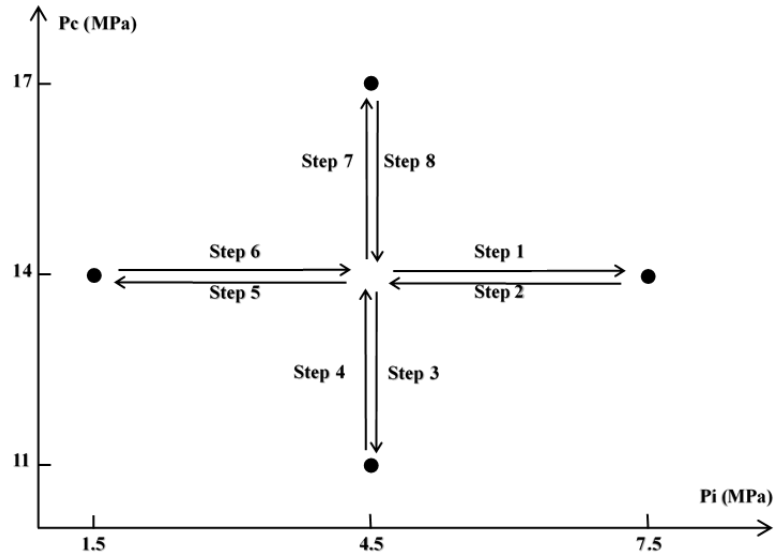

Figure V .2: simplified flowchart for Biot's coefficient measurement test under the confining pressure of 14MPa

Stress and strain evolution with time in the test is showed in FigureV .3 and FigureV .4. It can be seen from FigureV .3, take first step as example, at initial stage, the sample is under 14MPa confining pressure and 4.5MPa pore pressure. First, the confining pressure is kept constant, pore pressure is increases to 7.5Mpa(step1). And after deformation stabilizes, pore pressure is decreased back to 4.5Mpa(step2). Through those steps, the effective stress has also experienced a decrease from 9.5Mpa to 6.5Mpa and then an increase from 6.5MPa to 9.5MPa. Then, pore pressure is kept constant as 4.5MPa and the confining pressure is decreased to 11Mpa(step3), after the deformation stabilizes, it increases back to 14MPa(step4). Therefore, the effective stress repeats the above process that experiences a decrease from 9.5Mpa to 6.5Mpa and then an increase from 6.5MPa to 9.5MPa. Through the two cycles, Biot's coefficient could be obtained by the ratio of two volume strain increment respectively caused by pore pressure and confining pressure change.

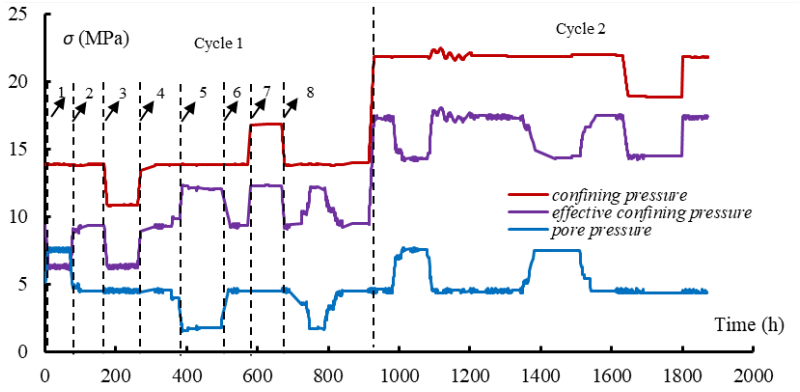

Figure V .3: Stress–time evolution in Biot's coefficient measurement test

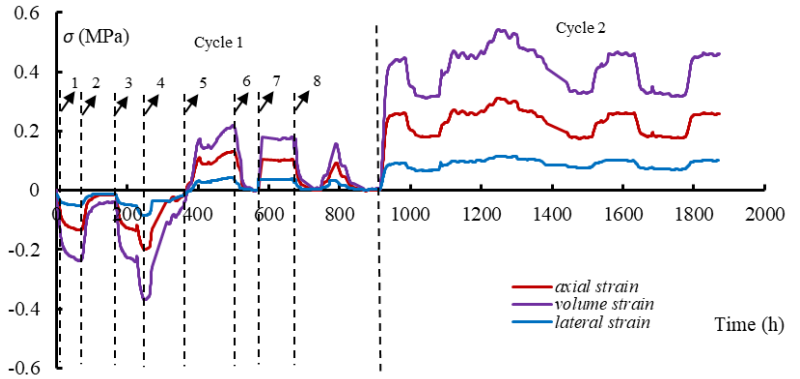

Figure V .4: Strain-time evolution in Biot's coefficient measurement test

It is worth to note that the increase and decrease of the pore stress are not instantaneous, so it is necessary to wait long enough to ensure that deformation caused by pore pressure is stable. In this test, each step takes at least for three days to ensure the deformation is stable. As we mentioned above, Biot's coefficient is determined by two loading paths, the effective stress decreases(step1-4), and effective stress increases(step5-8) which showed in FigureV .3. And we could see in FigureV .4, between step3 and step4, there is a volume deformation expansion under constant stress state as σ_r=11MPa,P_i=4.5MPa, the effective confining pressure is 6.5MPa, the result shows the 6.5MPa effective confining pressure does not seem to be able to limit the expansion of saturated COx claystone well. So for cycle 1, Biot's coefficient is determined by effective stress increases loading path(step5-8) and the value is 0.96. Then at 22MPa confining pressure point, under high effective confining pressure, Biot's coefficient is determined by effective stress decreases loading path(step1-4) and the value is 0.91. The two loading paths are both seems

applicable for Biot's coefficient measuring test.

By comparing two Biot's coefficient value, Biot's coefficient value decreases slightly with confining pressure increased. In general, the decrease trend of Biot's coefficient value can be attributed to the closure of micro-cracks under high hydrostatic pressure.

In this test, the measured Biot's coefficient values are both slightly less than but very close to 1, the result indicates that under hydrostatic stage, the rock skeleton almost bears all pore stress, and effective stress concept is applicable for saturated COx claystone in elastic domain.

3.2 Determination of Skempton coefficient

Meanwhile, Skempton coefficient is determined. It is an important pore-fluid parameter, and it is a bridge connecting pore pressure and the mean stress. Skempton coefficient is affected by many factors and even for the same rock or soils, the value is not constant, and it is related to initial stress state, the stress path, and changes non-linearly with deviatoric stress change. Skempton coefficient is determined as the ratio of pore pressure change to mean stress change under undrained condition. The formula to calculate Skempton coefficient is as below:

$$A = \frac{\Delta P_i}{\Delta \sigma_m} \tag{V .6}$$

$\Delta\sigma_m$ is mean stress increment, $\Delta \mathrm{P}_i$ is pore pressure increment, and under hydrostatic stage mean stress is equal to the confining pressure. So the experimental steps are shown as below:

(a). Perform saturation step, then load confining pressure to 14MPa and pore pressure to 4.5MPa.

(b). When the deformation keeps stable, select and note the strain value as start point. Then close both pore pressure injection pipes, the test is under undrained condition, slowly load confining pressure to 22MPa with the rate of 0.8MPa/h and record pore pressure change through the sensor.

(c). When the deformation keeps stable, unload the confining pressure slowly from 22MPa to 14MPa with the same rate, record pore pressure change through the sensor. Finally compare pore pressure change value with confining pressure change value to determine Skempton coefficient.

Test result and revolution could be shown in FigureV .5 that Skempton coefficient value is 0.86 in loading stage and 0.72 in unloading stage.

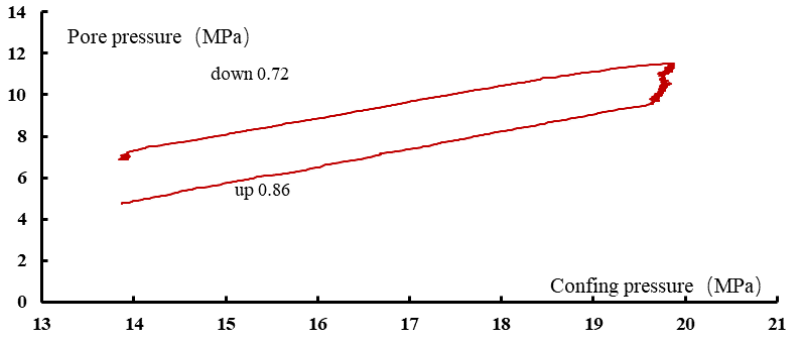

Figure V .5: Pore pressure–stress evolution in Skempton coefficient measurement test

4 Lateral decompression and axial extension test with poromechanical cycles

The above content has verified the validity of effective stress concept in elastic domain. And in this section the existence and validity of effective stress concept in plastic domain for the saturated COx claystone should be verified. (De Buhan and Dormieux, 1996, 1999) showed that the failure criterion of saturated porous materials can be expressed by effective stress concept, and the form of the effective stress tensor depends on the failure mechanical properties of solid matrix material. For initial elastic threshold of saturated porous materials, (Lydzba and Shao, 2000) obtained similar results which were carried out under two specific loading conditions. A more general study on this issue is completed which confirms the applicability of effective stress concept in plastic strengthening domain (Lydzba and Shao, 2002). In addition a model has been proposed for the description of plastic behavior of a porous chalk, including creep deformation and water saturation effect to study the mechanism and application of effective stress concept in plastic domain for chalk (Xie and Shao, 2006).

An experimental study is completed on pore plastic mechanical properties of porous chalk which verified the effective stress concept by comparing the deformation of two samples under the same stress state (the effective stress is the same) with different loading paths (Kherbouche et al., 1995). Inspired by similar method, in this section, specific poroplastic coupling tests with axial extension and lateral decompression loading paths are carried out. The two loading paths are composed of a series of poromechanical cycles to verify the existence and validity of effective stress concept in plastic domain for saturated COx claystone.

Test method is illustrated in FigureV .6. A poromechanical loading cycle from a

reference state in plastic domain is proposed, by alternating the variation of the interstitial pressure as well as axial and lateral stresses, while the effective stresses are kept as the same value. The aim is to check whether the points at different values of pressure and stresses (but the same values in effective stresses) (points 2 and 4 on FigureV .6) are actually on same deformation condition, which obtained by two different loading path as lateral compression and axial extension paths.

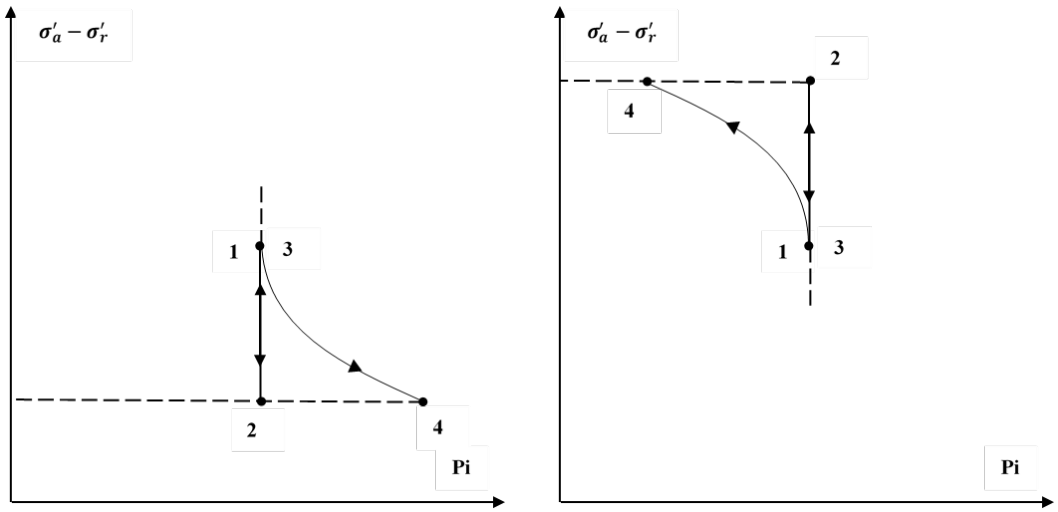

(a) principle of lateral decompression test (b) principle of axial extension test

Figure V .6: Poromechanical test method with constant mean stress

4.1 Lateral decompression test

4.1.1 test method

For lateral decompression tests, as FigureV .6(a) shows, the experimental steps are set as follows:

(a). Load sample and perform saturation step, then load hydrostatic pressure to 16.5MPa and pore pressure to 4.5MPa.

(b). At initial stage, axial stress and lateral stress are both 16.5MPa, pore pressure is 4.5MPa, set this stress state as start point of 0% stage. According to previous test experience and considering water weakening effect, the assumed rock failure point is set as effective lateral stress equals to 7MPa and the effective axial stress equals to 22MPa, while effective mean stress is maintained as 12MPa,so pore pressure is 4.5MPa, axial stress is 26.5MPa and lateral stress is 11.5MPa. Set this stress state as end point of 100% stage, and sequentially each stress state is divided from 0-100% stage.

(c). Load axial stress with the rate of 0.01MPa/min. While axial stress increases, decrease lateral stress and keep pore pressure constant with constant effective mean stress. Increase stress state to assumed 50% stage, as lateral stress reaches 14MPa, pore pressure keeps 4.5MPa, and axial stress reaches 21.5MPa, then keep stress state constant until deformation is stable.

(d). Increase lateral stress, decrease axial stress and keep pore pressure constant with same rate to assumed 25% stage, as lateral stress reaches 15.25MPa, pore pressure keeps 4.5MPa, and axial stress reaches 19MPa, then keep stress state constant until deformation is stable.

(e). Increase pore pressure, increase axial stress and keep lateral stress constant with same rate to assumed 50% stage, as lateral stress keeps 15.25MPa, pore pressure reaches 5.75MPa, and axial stress reaches 22.75MPa, then keep stress state constant until deformation is stable.

(f). Compare the deformation increment in step(c) with it in step(e), for these two steps, effective axial and lateral stresses at end phases are the same value, so by comparing volume strain increments the effective stress concept could be verified intuitively.

(g). Decrease pore pressure, lateral stress, and axial stress with same rate back to initial assumed 50% stage, as lateral stress reaches 14MPa, pore pressure reaches 4.5MPa, and axial stress reaches 21.5MPa, then keep stress state constant until deformation is stable.

(h). Keep pore pressure constant, increase axial stress and decrease lateral stress with same rate to assumed 75% stage, then keep stress state constant until deformation is stable, and repeat steps(c)–(g).

(i). Keep pore pressure constant, increase axial stress and decrease lateral stress with same rate to assumed 90% stage, then keep stress state constant until deformation is stable, and repeat steps(c)–(g).

(j). Keep pore pressure constant, increase axial stress and decrease lateral stress with same rate until sample broken.

4.1.2 Lateral decompression test results

FigureV .7 shows experimental procedure flowcharts of lateral decompression test, from this figure the evolution of lateral stress, axial stress and pore pressure with time are showed. It starts from a reference state (point 1) in plastic domain, first increase axial stress and decrease lateral stress to point 2 and keep pore pressure constant, then unload axial stress and increase lateral stress to point 3. From this point, keep lateral stress

constant, increase pore pressure and axial stress to point 4. For the test, the effective stress is respectively determined at points 2 and 4. The axial stress, lateral stress and pore pressure values are different between these two points. Point 4 and point 2 are on same plastic loading surface. These two points have same effective stress value, but are obtained through two stress loading paths. The following axial extension test is the same method with different loading path.

It should be noted that, as COx claystone is a low-permeability material, for both two kinds of tests, each step is last for 8 hours and time between each step should be last for one day for deformation stabilization.

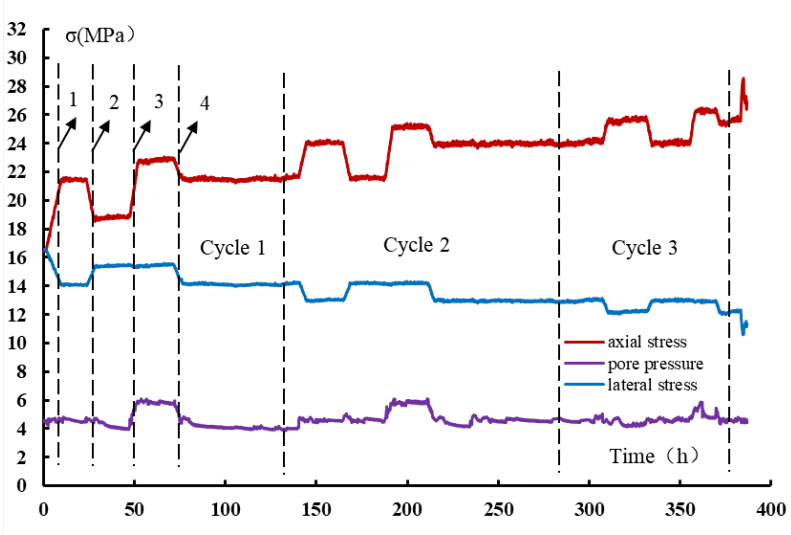

Figure V .7: Stress evolution with time in lateral decompression test

FigureV .8 reflects the relationship between effective stress and strain in lateral decompression test. From this figure, we can see that sample is actually undergoing an unloading-loading poromechanical cycle. The peak strength of sample C9 is σ_a=28.55Pa,σ_r=10.64MPa,P_i=4.5MPa as effective axial stress is 24.05MPa and effective lateral stress is 6.14MPa. Due to the complex mechanical property of COx claystone, it is very difficult to control exactly the stress loading level in advance even though we have kept many factors constant in our tests, the COx claystone mechanical resistance is weakened, so the stress degree at each state is also corrected.

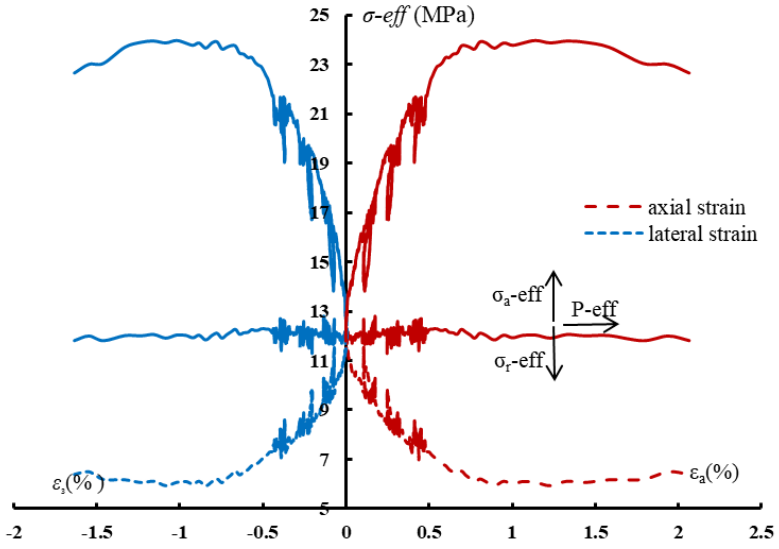

Figure V .8: Effective stress-strain evolution in lateral decompression test

4.2 Axial extension test

4.2.1 test method

For axial extension test, the steps are similar to lateral decompression tests. First, at initial stage, axial stress and lateral stress are both 16.5MPa, pore pressure is 4.5MPa, this stress state is set as start point of 0% stage. As ChapterIII mentioned the effective axial stress reaches 0MPa and the effective lateral pressure reaches 18MPa, this stress state is set as 100% stage. So, in this chapter, when axial stress reaches 4.5MPa, lateral stress reaches 22.5MPa and pore pressure reaches 4.5MPa, this stress state is set as end point of 100% degree. And sequentially each stress state is divided from 0-100% stage. However, for first test, the sample occurs creep failure when it reaches to assumed 75% stage, as axial stress reached 7.5MPa, lateral stress reaches 21MPa and pore pressure reaches 4.5MPa, as FigureV .6(b) showed. The result indicates that the strength of COx claystone is weaken under saturation state. So for second sample the assumed 100% point is set as first test creep failure point, and the 50%, 75% and 90% stress state level are reset as well. The experimental steps are set as follows:

(a). Load sample and perform saturation step, then load hydrostatic pressure to 16.5MPa and pore pressure to 4.5MPa.

(b). As mentioned above, this stress state is set as start point of 0% stage. The stress state that axial stress reaches 3MPa, lateral stress reaches 21MPa and pore pressure

reaches 4.5MPa is set as end point of 100% stage.

(c). Reload axial stress with the rate of 0.01MPa/min. While axial stress decreases, increase lateral stress and keep pore pressure constant to keep effective mean stress constant. Increase stress state to assumed 50% stage, as lateral stress reaches 18.75MPa, pore pressure keeps 4.5MPa, and axial stress reaches 12MPa, then keep stress state constant until deformation is stable.

(d). Decrease lateral stress, increase axial stress and keep pore pressure constant with same rate to assumed 25% stage, as lateral stress reaches 17.625MPa, pore pressure keeps 4.5MPa, and axial stress reaches 14.25MPa, then keep stress state constant until deformation is stable.

(e). Increase pore pressure, decrease axial stress and keep lateral stress constant with same rate to assumed 50% stage, as lateral stress keeps 17.625MPa, pore pressure reaches 3.375MPa, and axial stress reaches 13.125MPa, then keep stress state constant until deformation is stable.

(f). Compare the deformation increment in step(c) with it in step(e), for these two steps, effective axial and lateral stresses at end phases are the same value, so by comparing volume strain increments the effective stress concept could be verified intuitively.

(g). Increase pore pressure, lateral stress, and decrease axial stress with same rate back to initial assumed 50% stage, as lateral stress reaches 18.75MPa, pore pressure reaches 4.5MPa, and axial stress reaches 12MPa, then keep stress state constant until deformation is stable.

(h). Keep pore pressure constant, decrease axial stress and increase lateral stress with same rate to assumed 75% stage, then keep stress state constant until deformation is stable, and repeat steps(c)–(g).

(i). Keep pore pressure constant, decrease axial stress and increase lateral stress with same rate to assumed 90% stage, then keep stress state constant until deformation is stable, and repeat steps(c)–(g).

(j). Keep pore pressure constant, decrease axial stress and increase lateral stress with same rate until sample broken.

4.2.2 Axial extension test results

For axial extension test, samples C10 and C11 are used, for first axial extension test with sample C10, during test process, the sample undergoes ductile failure after second stress level loaded. As shown in FigureV .9, the peak strength is σ_a=7.5MPa,σ_r=21MPa,P_i=4.5MPa, as effective axial stress reaches 3MPa and effective lateral stress reaches 16.5MPa. The

result indicates that water content weaken for sample strength under axial extension condition could not be ignored. Therefore, sample C11 is selected for second axial extension test. In second axial extension test, the assumed 100% stage refers to the peak strength for first experiment, and on this basis, the 50%, 75% and 90% stages are re-determined.

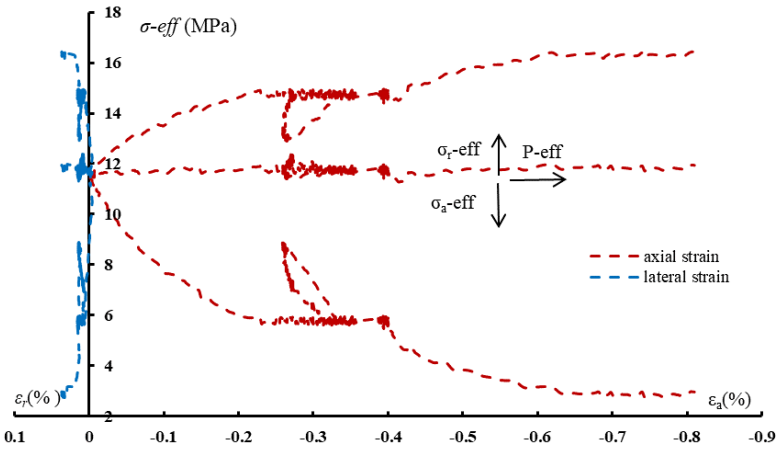

Figure V .9: Effective Stress-strain evolution in first axial extension test

Therefore, second axial extension test is proposed on the base of former test. FigureV .10 shows the experimental procedure flowcharts of second axial extension test, from this figure the evolution of lateral stress, axial stress and pore pressure with time are shown. Just like decompression test, it starts from a reference state(point 1) in plastic domain, first decrease axial stress and increase lateral stress to point 2 and keep pore pressure constant, then increase the axial stress and decrease lateral stress to point 3. From this point, keep lateral stress constant and decrease axial stress and pore pressure to point 4. For the test, the effective stress is respectively determined at points 2 and 4. The axial stress, lateral stress and pore pressure values are different between these two points. Point 4 and point 2 are on same plastic loading surface. These two points have same effective stress value, but are obtained through two stress loading paths.

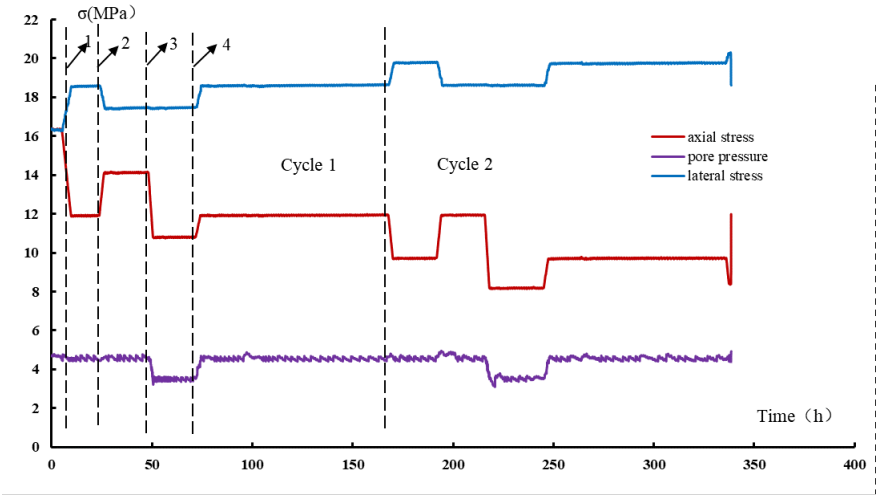

Figure V .10: Stress evolution with time in second axial extension test

FigureV .11 reflects the relationship between effective stress and strain in axial extension test. The sample turns to be broken at 90% degree. The peak strength is σ_a=8.4Pa,σ_r=20.55MPa,P_i=4.5MPa, as effective axial stress reaches 3.9MPa and effective lateral stress reaches 16.05MPa. The peak strength is lower than predicted value, and this may attribute to structural difference and the water weaken, so the stress degree at each level is also re-corrected.

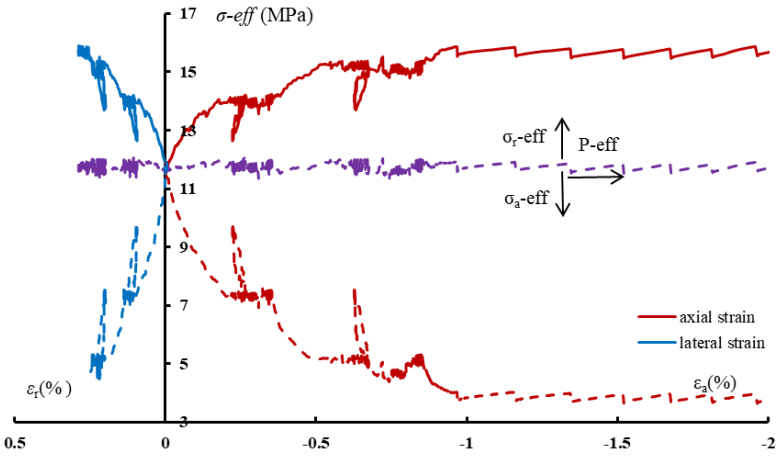

Figure V .11: Effective Stress-strain evolution in second axial extension test

4.3 Analysis of decompression and extension tests

FigureV .12 is a partial enlarged view of FigureV .8 for lateral decompression test. In this figure, poromechanical cycle at three stress levels can be more intuitively shown. Through the process, with effective axial stress increases, effective lateral stress decreases, sample is compressed in axial direction and dilated in lateral direction. Process corresponding to Step(c)–(g) in the test is shown in this figure.

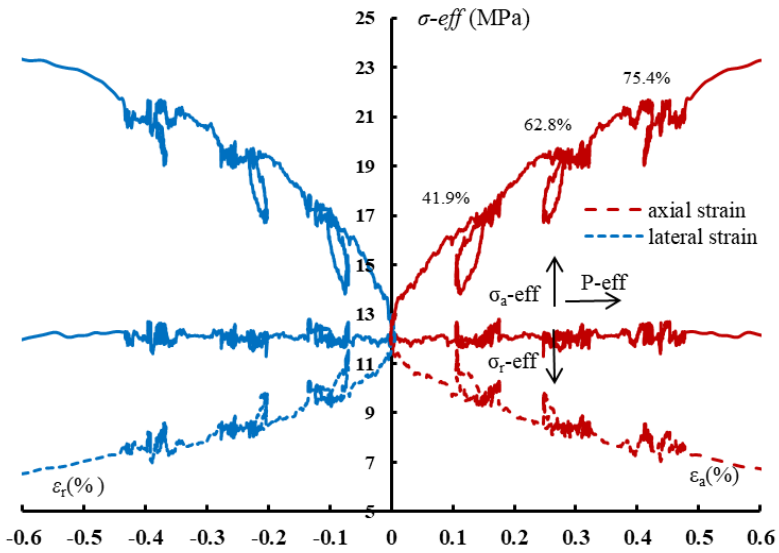

Figure V .12: Enlarged version of effective Stress-strain evolution in lateral decompression test

FigureV .13 shows deviatoric stress evolution with strain. As shown in the figure, points 1–4 are marked as well. In this test, peak deviatoric stress q is 17.91MPa, the value is smaller, compared with unsaturated sample result as q=20.1MPa (Liu et al., 2019a), due to water content weaken effect. From volume strain trend we could find sample is delated through the process.

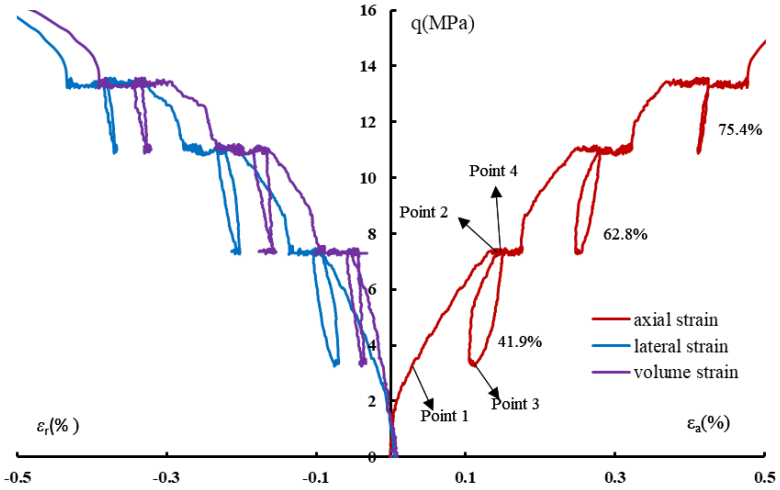

Figure V .13: Deviator stress evolution with strain in lateral decompression test with mean stress of 12MPa

FigureV .14 is a partial enlarged view of FigureV .11 for axial extension test. Through the path, with effective axial stress decreases, effective lateral stress increases, sample is dilated in axial direction and compressed in lateral direction. Process corresponding to Step(c)–(g) in the test is shown in this figure.

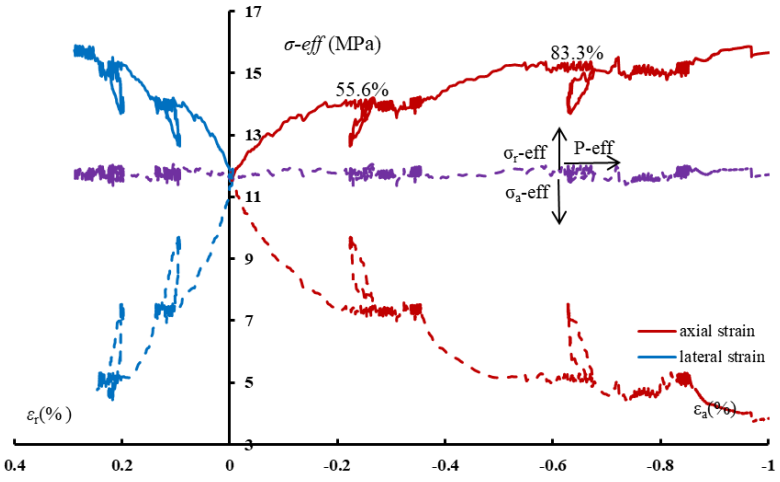

Figure V .14: Enlarged version of effective Stress-strain evolution in second axial extension test

FigureV .15 shows deviatoric stress evolution with strain. As shown in the figure, points 1–4 are marked as well. From volume strain trend we could find sample is delated through the whole process. From the axial extension creep test mentioned in ChapterIII ,

peak deviatoric stress of 90° sample q is -21.57MPa. In this test the two peak deviatoric stresses for two extension tests are respectively -14.08 and -11.8MPa, the results also shows water content weaken effect.

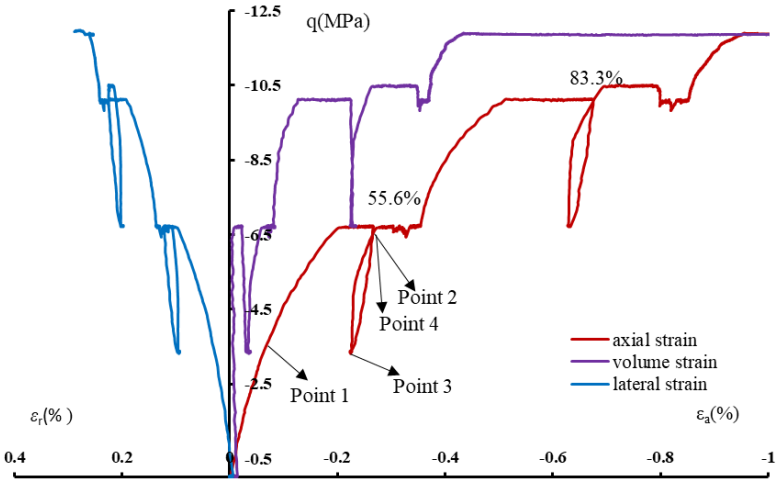

Figure V .15: Deviatoric stress evolution with strain in second axial extension test with mean stress of 12MPa

By analysing poroplastic coupling tests with two loading paths we can see that the all peak strengths are weakened by water effect. For each poroplastic cycle, point 4 and point 2 are on same effective stress loading degree. The two points have almost the same effective stress value, but they are obtained through different stress loading paths, and the deformations for two points are almost the same. The results indicate that effective concept is applicable in plastic domain under axial extension and lateral decompression loading paths.

5 Oedometric test under drained and undrained conditions

5.1 Test Method

For oedometric test, both deviatoric pressure and confining pressure should increase simultaneously. The confining pressure should be increased to contain lateral deformation of sample as zero accompanied with increasing deviatoric stress. The deviatoric stress is chosen to play a dominant controlled role in loading process, then through matching lateral deformation stablization, the confining pressure is then adjusted.

The testing procedure for oedometric test is given as follows. The deviatoric pressure is piloted by a computer-controlled pressure generator with the given flow rate(0.01MPa/min).

The confining pressure is simultaneously readjusted to make sure that the change of lateral deformation keeps zero. Also, through oedometric tests under different drainage condition, the multistage loading-unloading cycles are carried out.

The test steps are as below:

(a). Load sample and perform saturation step, then load the confining pressure to 14MPa and pore pressure to 4.5MPa;

(b). When deformation is stable, select and note the strain value as starting point. For test under drained condition, keep pore pressure injection pipe open, increase devialotric stress with the rate of 0.01MPa/min, and keep confining pressure increased in order to keep lateral deformation constant, the loading-unloading cycles are respectively taken when confining pressure increased to 25, 30, 40 and 47MPa, each loading-unloading cycle is last for 8 hours, time between each cycle should be last for one day for deformation stabilization.

(c). For test under undrained condition, close pore pressure injection pipe before formal test. And increase devialotric stress and confining pressure in order to keep lateral deformation constant, as in undrained path, pore pressure changes as well. the loading-unloading cycles are respectively taken when confining pressure increased to 20, 30, 40 and 48MPa, each loading-unloading cycle is last for 8 hours, time between each cycle should be last for one day for deformation stabilization.

5.2 Test results of oedometric test

For sample C12 under drained condition, at initial stage, lateral stress is 14MPa, axial stress is 15MPa and pore pressure is 4.7MPa. FigureV .16 shows stress, strain and time evolution. From the figure we can see four loading-reloading cycles are proposed, when lateral stress is respectively loaded to 25,30,40 and 47MPa in which axial stress is loaded to 30,37,52 and 62MPa, respectively.

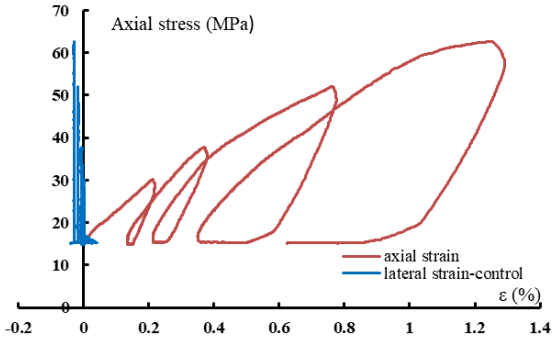

(a) the axial stress-strain evolution of sample C12

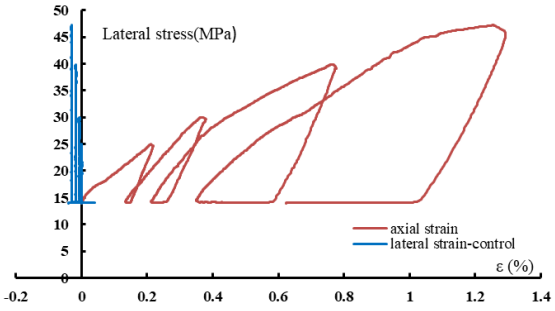

(b) the lateral stress-strain evolution of sample C12

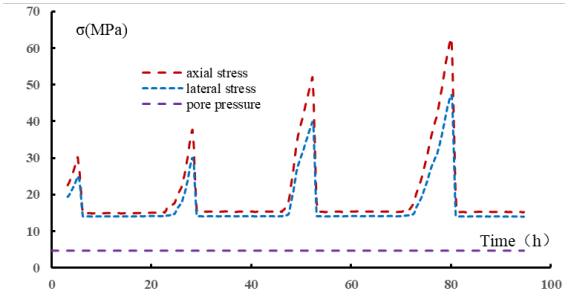

(c) stress-time evolution of sample C12

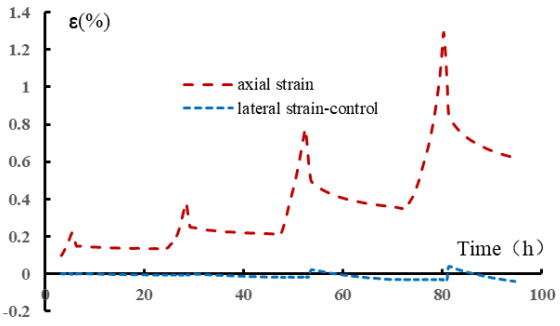

(d) strain-time evolution of sample C12

Figure V .16: The stress,strain and time evolution for sample C12 under drained condion

From FigureV .16(a) and FigureV .16(b) we can see in each cycle, lateral stress varies with axial stress to keep lateral deformation constant, and pore pressure keeps unchanged. For oedometric process, the lateral deformation is kept stable while the axial deformation is compressed. And the axial deformation that can be increased with axial stress and weakened with lateral stress could easily be measured.

For sample C13 under undrained condition, at initial stage, lateral stress is 14MPa, axial stress is 15MPa and pore pressure is 4.7MPa. FigureV .17 shows stress, strain and time evolution. From the figure we can see four loading-reloading cycles are proposed when lateral stress is respectively loaded to 20,30,40 and 48MPa in which axial stress is loaded to 30,37,52 and 62MPa, respectively. There are two interrupts during test process due to sensor failure, but the pause does not affect experimental results, which are noted in the FigureV .17.

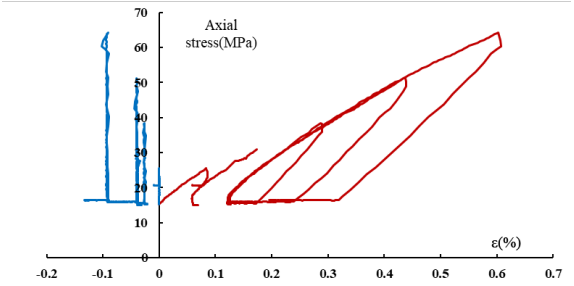

(a) the axial stress-strain evolution of sample C13

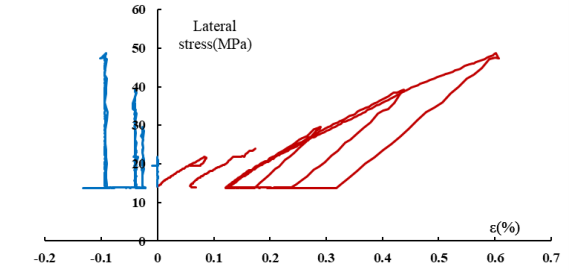

(b) the lateral stress-strain evolution of sample C13

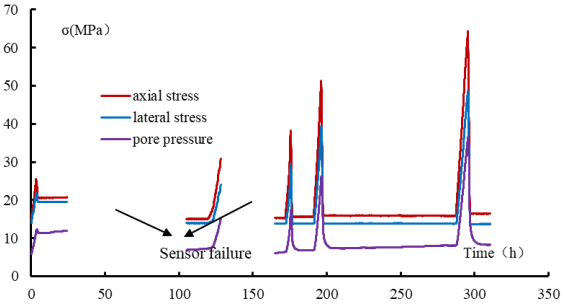

(c) stress-time evolution of sample C13

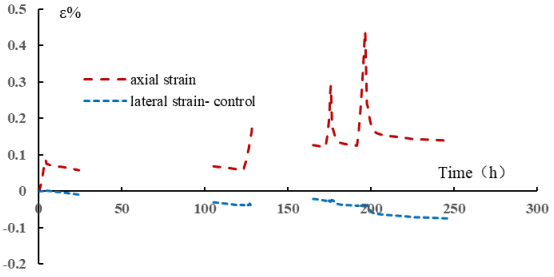

(d) strain-time evolution of sample C13

Figure V .17: The stresses and strains evolutions for sample C13 under undrained condition

Oedometric test under undrained condition is more complicated, when stress loaded,

the sample is compressed, and this induces pore pressure increase and effective stress change. After loading and unloading cycles, as plastic deformation occurs, the axial strain as well as pore pressure could not return to initial level.

FigureV .18 shows effective axial stress with axial strain evolution under different drainage conditions under logarithmic coordinate system.

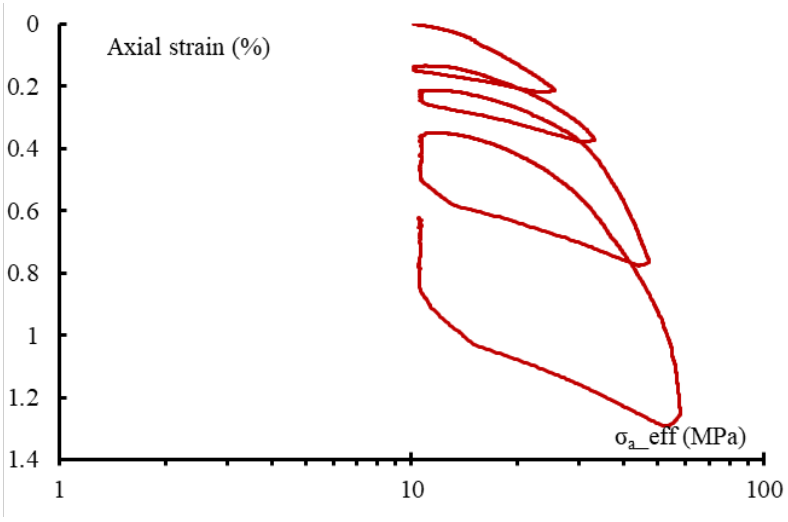

(a) drained condition of C12

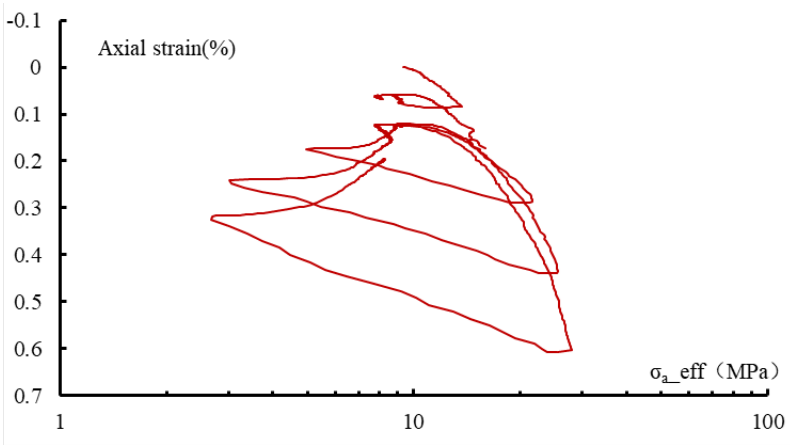

(b) undrained condition of C13

Figure V .18: Effective axial stress versus strain curve of oedometric test

5.3 Analysis of oedometric test

FigureV .19(a) shows effective axial stress versus axial strain evolution and FigureV .19(b) shows effective lateral stress versus axial strain evolution, both for two tests.

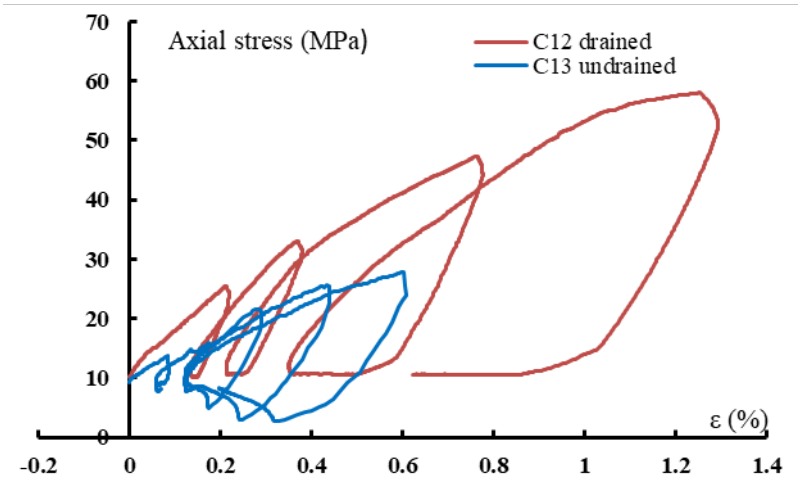

(a) effective axial stress versus axial strain evolution

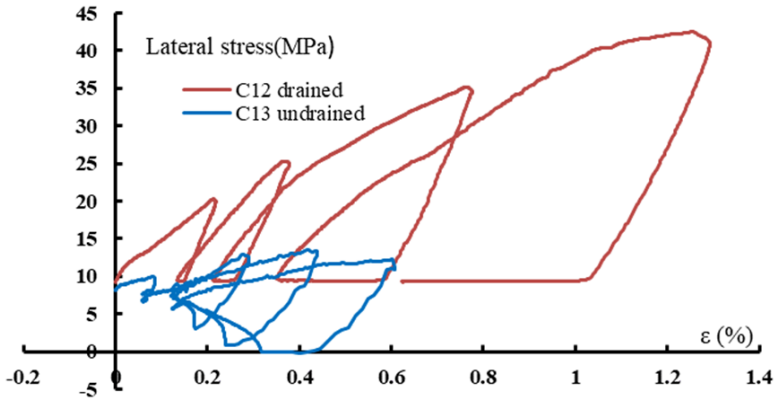

(b) effective lateral stress versus axial strain evolution

Figure V .19: Effective stress versus strain curve of oedometric test under different drainage condition

The basic mechanical response of the COx claystone under oedometric compression can be divided into three phases. In first phase when loading stage begins, there exists a short nonlinear concave upward curve, this attributes to plastic compaction of weakness pores as well as plastic shear slip. In second phase, a linear elastic phase is obtained, this is shown clearly in first two cycles, this is because the effective axial stress is less than pore collapse yield stress, then sample occurs elastic deformation. In third phrase, when effective axial stress reaches pore collapse yield stress, plastic deformation occurs, which attributes to inner pores collapse under high stress. And an accelerated increase of contact

surface between particles is produced. This is due to further plastic pore collapse, and it leads to a plastic strengthening phase with a decreasing axial strain rate, this is shown clearly in the third and fourth cycles.

From FigureV .19 we can see effective axial and lateral stresses at each level under undrained condition is lower than those under drained condition. This is because under undrained condition, as deviatoric stress increases, the corresponding confining pressure increases which causes pore pressure increases, and it would induce the decrease of effective confining pressure and deviatoric stress. The evolution of deviatoric stress with effective mean stress is drawn in FigureV .20.

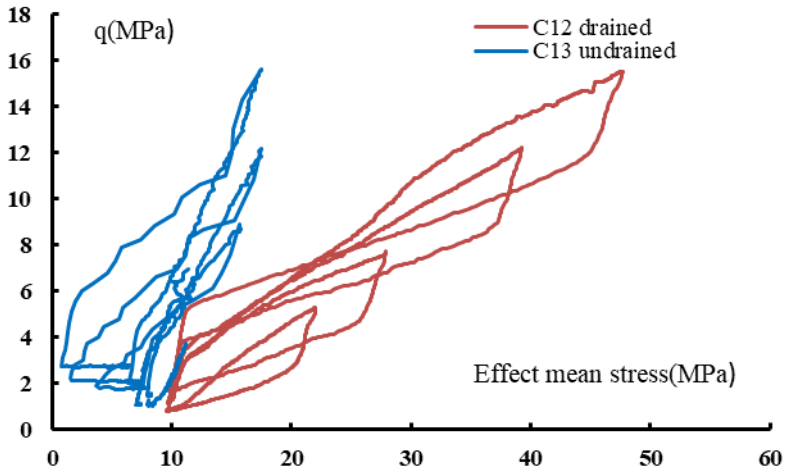

Figure V .20: deviatoric stress-effective mean stress curve

The figure shows that for oedometric test under drained condition, the deviatoric stress augments monotonically with the effective mean stress increases. The whole experiment is a consolidation process through compression, which produces plastic deformation of sample. And for test under undrained condition, with deviatoric stress increases, the effective mean stress is kept as a low value ranged from 0–15MPa, due to pore pressure increasing. The result indicates that the sample is at superporous state and damaged by expansion, and its compression deformation is partially offset by expansion damage, so the test shows a lower axial strain value.

The elastic oedometric modulus could be obtained through the slope of effective axial stress-strain linear curve from unloading stage. And the calculated oedometric modulus for each cycle are plotted in FigureV .21. From FigureV .21 we can see that the oedometric modulus decreases with stress state level increases. For test under drained condition, the experimental result reflects that the oedometric modulus only shows a s-

light decrease, mainly because the sample is in the consolidated compression state. For test under undrained condition, the oedometric modulus shows a significant decrease with oedometric loading, this is mainly because with pore pressure increases, the effective confining pressure decreases and it causes superporous delated damage. Accordingly, the oedometric modulus decreases with the oedometric loading.

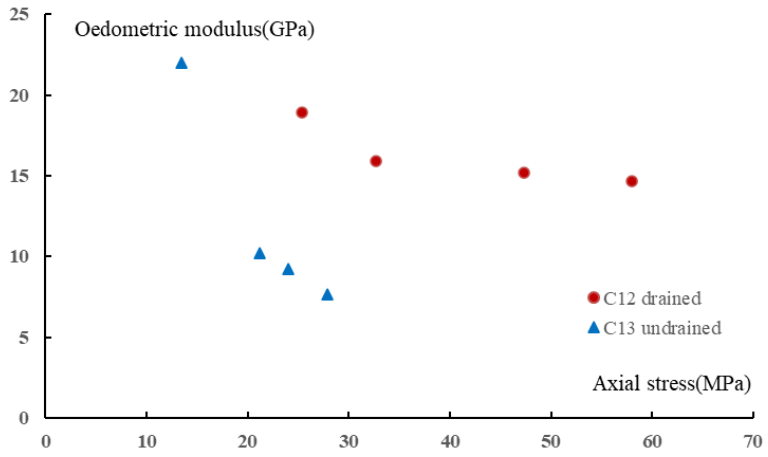

Figure V .21: Stress dependency of oedometric modulus

6 Concluding remarks

In this chapter, three groups of new tests were performed to investigate the poromechanical coupling properties of COx claystone. Based on the obtained experimental data, the following conclusions were drawn:

(1). Biot's coefficient of COx claystone determined under hydrostatic pressure was close to 1; therefore, the effective stress concept was applicable during the elastic stage. Biot's coefficient value decreased slightly as the confining pressure increased because stress increase caused pores and micro-cracks to close, and decreased Biot's coefficient. Skempton coefficient of COx claystone under 14-22MPa hydrostatic pressure was between 0.72 and 0.86.

(2). For the lateral decompression poromechanical test, the saturated sample failed at effective lateral stress of 6.14MPa and effective axial stress of 24.05MPa. For the axial extension poromechanical test, two samples failed at effective lateral stress of 16.5 and 16.05MPa and effective axial stress of 3.0 and 3.9MPa. The effective stress concept was verified in the plastic domain under poroplastic cycles.

(3). For the oedometric tests, the mechanical responses under drained and undrained

oedometric conditions were different. Under drained conditions, the samples in the entire experiment were in a consolidation process by compression as the sample producing plastic deformation by compression. Under undrained conditions, except compression plastic deformation, sample had irreversible expansion deformation at the superporous state. Under the drained loading path, the results showed that even if the sample entered the plastic deformation state, the oedometric modulus only showed a slight decrease, mainly because the sample was in the consolidated compression state. In contrast, under the undrained loading path, the oedometric modulus showed a significant decrease, mainly because as the pore pressure increased, the effective confining pressure decreased and caused superporous delated damage. Accordingly, the undrained oedometric modulus decreased with the oedometric loading.

Chapter VI

Conclusions and Perspectives

1 Conclusions

In this thesis, laboratory tests with new loading conditions were performed and analyzed. Axial extension creep tests with five loading angles were performed, gas permeability evolution was investigated in fractured samples, and different loading cycles to measure Biot's and Skempton coefficients were proposed. In addition, the effect of pore pressure on plastic or strength criteria was investigated. The main results obtained are summarized below:

- In Chapter III , the axial extension creep tests first showed that the sample was compressed in the lateral direction and dilated in the axial one. For the 50% stress stage, the creep strains (axial and radial) were within a small range and became stable quickly. For the 90% stress stage, the creep rate was accelerated, and the time to reach strain stabilization was longer than that for the 50% stress stage. By comparing the strain increases between the two stages, for the axial creep strain, the increase in the 90% stress stage was larger than that in the 50% stress stage, whereas for the lateral creep strain, the increase in the 90% stress stage was smaller than that in the 50% stress stage.

  Second, by comparing the creep strains between the different loading angles, the axial and lateral strains of the 30° and 60° samples were significantly larger than those of the 0°, 45° and 90° samples because the strains came from the shear slip of the discontinuous surfaces inside the sample. Depending on the direction of 30° and 60°, the shear slip was more conducive and showed a more apparent trend. For the 90° sample, because its axial direction was perpendicular to the bedding planes, its axial strain was greater than its lateral strain, and it was also greater than the axial

strains of the other angles. For the 0° sample, the axial and lateral strains were smaller, which was because its axial direction was parallel to the bedding planes, and the sample was compacted in the confining loading stage.

Third, by analyzing the volume deformation characteristics, at the 50% stress stage, the volumetric strains of the 0°, 30°, 45°, and 90° samples were compressed; however, for the 60° sample, the volumetric strain was dilated. At the 90% stress stage, the volume strains of the 0°, 30° and 45° samples were still in the compression zone and stabilized over time. Therefore, at the 90% stress stage, the volumetric strains with small angles were almost unchanged. For samples with large angles, the volumetric strains showed significant creep expansion.

- In Chapter IV , first, for rock mechanical properties, when shear stress increased, the rock compressed axially and dilated laterally, and the sample deformation (axial and lateral) increased with shear stress increase and confining pressure decrease. For intact samples, due to the low levels of applied shear stress, all samples showed a stable creep tendency. For fractured samples, no significant creep strains (axial and lateral) were observed on fractured samples when the applied shear stress was approximately 50% of peak shear strength. However, when the shear stress was increased to 70% of peak strength, large and unstable shear creep deformation occurred. The shear failure strength was enhanced as the confining pressure increased. When the shear stress was kept constant, the decrease of confining pressure caused plastic shear deformation. The strength of the C16 sample was slightly lower than the fitted line; therefore, C16 had relatively lower shear strength among the three samples. It was also observed that C16 had abnormal compression in the lateral deformation during shear failure. This phenomenon was difficult to provide a convincing explanation, and requires further experimental observations.

  Second, gas permeability evolution was related to the applied shear stress, confining pressure, and gas injection pressure; however, its characteristics were more complex than the evolution of deformation, and it exhibited greater dispersion. For gas permeability evolution with intact samples, as the internal pores and cracks of the sample were closed under high confining pressure, it was harder for the gas to break through the sample. The gas permeability decreased as the confining pressure increased. For samples with obvious internal micro-cracks, the increase in shear stress led to a larger gas permeability trend. For denser samples, the increase in shear stress led to a smaller gas permeability trend. The reason for this phenomenon

might be caused by the microstructure of the two samples themselves. However, the experimental results do not fully support this hypothesis. For gas permeability evolution with fractured samples, the gas permeability evolution after shear failure stage were consistent with their lateral deformation changes. For the permeability of fractured claystone damaged by shearing under extremely low confining pressures, the increase in permeability caused by the increase in confining pressure was more significant than the decrease in permeability caused by the increase in shear stress. Through the gas permeability evolution with confining pressure under hydrostatic stress state with fractured sample, we found that as the effective confining pressure increased, gas permeability decreased as the cracks became more compressed and closed, leading to partial closure or decrease in gas permeation channels. The decrease of the confining pressure caused the cracks to dilate and open, leading to the partial connection of gas permeation channels, and an increase in the permeability of fractured claystone. The relationship between gas permeability and effective confining pressure was not linear. Under higher confining pressure, the permeability increased s-lightly with a decrease in the confining pressure, whereas under lower confining pressure, the permeability increased, and the lateral deformation was in good agreement with the permeability evolution. Therefore, the permeability change was mainly affected by the lateral deformation.

Further studies are required to expand on these preliminary results.

- In Chapter V , a series of laboratory tests were undertaken to study the poroelastic parameters of the COx claystone under saturated conditions and the pore mechanical properties under different loading paths.

  First, Biot's coefficient of COx claystone was determined as 0.96 under 14MPa confining pressure and 4.5MPa pore pressure, and 0.91 under 22MPa confining pressure and 4.5MPa pore pressure. The results showed that the effective stress concept proposed by Terzaghi was suitable for saturated COx claystone in the elastic domain. The determined Biot's coefficient decreased slightly as the confining pressure increased, which was explained by the fact that the hydrostatic stress increase led to the closure of pores and micro-cracks and reduced Biot's coefficient. Skempton coefficient of COx claystone under hydrostatic state was determined as 0.72 in the loading process and 0.86 in the unloading path.

  Second, for lateral decompression test with poromechanical cycles, the saturated sample failed on an effective confining pressure of 6.14MPa and an effective axial

stress of 24.05MPa. For the axial extension tests with poromechanical cycles, two samples failed on the effective confining pressures of 16.5 and 16.05MPa, and the effective axial stress of 3.0 and 3.9MPa. The objective was to verify the existence and validity of effective stress concept in the plastic domain for the saturated COx claystone.

Third, for the oedometric test under the drained loading path, the sample in the entire experiment was in the compression consolidation process because the sample exhibited compressive plastic deformation. The experimental results showed that even if the sample entered the plastic deformation state, the oedometric modulus showed a slight decrease, mainly because the sample was in the consolidated compression state. For the oedometric test under the undrained loading path, except for the compression plastic deformation sample that showed irreversible expansion in the highly porous state, its oedometric modulus showed a significant decrease. This was mainly due to the increase in the pore pressure, leading to a decrease in the effective confining pressure and caused structural damage. Accordingly, the oedometric modulus decreased with the oedometric loading.

2 Perspectives

Based on the results obtained in the present study, several options for further experimental and theoretical studies are suggested below:

- Chapter III showed that the influence of the loading path on the mechanical behavior of COx claystone is extremely important and, based on the extension time-dependent research, the experimental study of decompression creep deformation requires further investigation.
- The confining pressure greatly influenced gas permeability as shown in Chapter IV ; therefore, future work should be undertaken on gas permeability evolution under low confining pressure, and the structure anisotropy considered.
- Based on the study in Chapter V , the poromechanical behavior of COx claystone should be investigated in the future as discrete experimental results are caused by low permeability of COx claystone.

Bibliography

ANDRA, S. (2005). Dossier 2005 argile: Synthesis: Evaluation of the feasibility of a geological repository in an argillaceous formation, meuse/haute-marne site.

Armand, G., Bumbieler, F., Conil, N., de la Vaissière, R., Bosgiraud, J.-M., and Vu, M.-N. (2017a). Main outcomes from in situ thermo-hydro-mechanical experiments programme to demonstrate feasibility of radioactive high-level waste disposal in the callovo-oxfordian claystone. *Journal of Rock Mechanics and Geotechnical Engineering*, 9(3):415–427.

Armand, G., Conil, N., Talandier, J., and Seyedi, D. M. (2017b). Fundamental aspects of the hydromechanical behaviour of callovo-oxfordian claystone: from experimental studies to model calibration and validation. *Computers and Geotechnics*, 85:277–286.

Auvray, C., Arnold, G., and Armand, G. (2015a). Experimental study of elastic properties of different constituents of partially saturated argillite using nano-indentation tests. *Engineering Geology*, 191:61–70.

Auvray, C., Morlot, C., Fourreau, E., Talandier, J., et al. (2015b). X-ray tomography applied to self-healing experiments on argillites. In *13th ISRM International Congress of Rock Mechanics*. International Society for Rock Mechanics and Rock Engineering.

Bellwald, P. (1993). A contribution to the design of tunnels in argillaceous rock.

Belmokhtar, M., Delage, P., Ghabezloo, S., and Conil, N. (2018). Drained triaxial tests in low-permeability shales: application to the callovo-oxfordian claystone. *Rock Mechanics and Rock Engineering*, 51(7):1979–1993.

Belmokhtar, M., Delage, P., Ghabezloo, S., Tang, A.-M., Menaceur, H., and Conil, N. (2017). Poroelasticity of the callovo–oxfordian claystone. *Rock Mechanics and Rock Engineering*, 50(4):871–889.

Bemer, E., Longuemare, P., and Vincké, O. (2004). Poroelastic parameters of meuse/haute marne argillites: effect of loading and saturation states. *Applied Clay Science*, 26(1-4):359–366.

Bérest, P. (1987). Viscoplasticité en mécanique des roches. *Manuel de rhéologie des géomatériaux*, pages 235–257.

Bérest, P., Charpentier, J., and Vales, F. (2001). Creep of argillite under small mechanical loading. In *Kiwir Conference, Paris*.

Billiotte, J., Yang, D., and Su, K. (2008). Experimental study on gas permeability of mudstones. *Physics and Chemistry of the Earth, Parts A/B/C*, 33:S231–S236.

Biot, M. A. (1941). General theory of three-dimensional consolidation. *Journal of applied physics*, 12(2):155–164.

Biot, M. A. (1956). Theory of deformation of a porous viscoelastic anisotropic solid. *Journal of Applied physics*, 27(5):459–467.

Biot, M. A. (1962). Mechanics of deformation and acoustic propagation in porous media. *Journal of applied physics*, 33(4):1482–1498.

Biot, M. A. (1973). Nonlinear and semilinear rheology of porous solids. *Journal of Geophysical Research*, 78(23):4924–4937.

Bishop, A. W. (1959). The principle of effective stress. *Teknisk ukeblad*, 39:859–863.

Bishop, A. W. and Blight, G. (1963). Some aspects of effective stress in saturated and partly saturated soils. *Geotechnique*, 13(3):177–197.

Blaise, T., Barbarand, J., Kars, M., Ploquin, F., Aubourg, C., Brigaud, B., Cathelineau, M., El Albani, A., Gautheron, C., Izart, A., et al. (2014). Reconstruction of low temperature (¡ 100 c) burial in sedimentary basins: a comparison of geothermometer in the intracontinental paris basin. *Marine and Petroleum Geology*, 53:71–87.

Bornert, M., Vales, F., Gharbi, H., and Nguyen Minh, D. (2010). Multiscale full-field strain measurements for micromechanical investigations of the hydromechanical behaviour of clayey rocks. *Strain*, 46(1):33–46.

Cariou, S., Duan, Z., Davy, C., Skoczylas, F., and Dormieux, L. (2012). Poromechanics of partially saturated cox argillite. *Applied clay science*, 56:36–47.

Charlez, P. A. and Heugas, O. (1992). Measurement of thermoporoelastic properties of rocks: theory and applications. In *Rock Characterization: ISRM Symposium, Eurock'92, Chester, UK, 14–17 September 1992*, pages 42–46. Thomas Telford Publishing.

Charlier, R., Collin, F., Pardoen, B., Talandier, J., Radu, J.-P., and Gerard, P. (2013). An unsaturated hydro-mechanical modelling of two in-situ experiments in callovo-oxfordian argillite. *Engineering geology*, 165:46–63.

Cheng, A.-D. (1997). Material coefficients of anisotropic poroelasticity. *International journal of rock mechanics and mining sciences*, 34(2):199–205.

Chiarelli, A., Shao, J., Ledesert, B., and Hoteit, N. (2001). Experimental study of mechanical behaviour of a clay-stone: application to nuclear waste disposals; etude experimentale du comportement mecanique d'argiles raides: application au stockage de dechets radio-actifs.

Chiarelli, A.-S. (2000). *Etude expérimentale et modélisation du comportement mécanique de l'argilité de l'Est: influence de la profondeur et de la teneur en eau*. PhD thesis, Lille 1.

Chiarelli, A.-S., Shao, J.-F., and Hoteit, N. (2003). Modeling of elastoplastic damage behavior of a claystone. *International Journal of plasticity*, 19(1):23–45.

Conil, N. (2012). Expérimentation ted, bilan de la deuxième anneé de chauffe. report d. rp. Technical report, AMFS.

Conil, N., Armand, G., Garitte, B., Jobmann, M., Jellouli, M., Filippi, M., De La Vaissière, R., and Morel, J. (2012). In situ heating test in callovo-oxfordian claystone, measurement and interpretation. In *5th International Meeting on Clays and Engineered Barriers for Radioactive Waste Confinement, Montpellier*, pages 22–25.

Coussy, O. (1995). *Mechanics of porous continua*. Wiley.

Coussy, O. (2004). *Poromechanics*. John Wiley & Sons.

Davy, C. A., Skoczylas, F., Barnichon, J.-D., and Lebon, P. (2007). Permeability of macro-cracked argillite under confinement: gas and water testing. *Physics and Chemistry of the Earth, Parts A/B/C*, 32(8-14):667–680.

De Buhan, P. and Dormieux, L. (1996). On the validity of the effective stress concept for assessing the strength of saturated porous materials: a homogenization approach. *Journal of the Mechanics and Physics of Solids*, 44(10):1649–1667.

De Buhan, P. and Dormieux, L. (1999). A micromechanics-based approach to the failure of saturated porous media. In *Porous Media: Theory and Experiments*, pages 47–62. Springer.

De La Vaissière, R., Conil, N., and Talandier, J. (2017). Synthèse des paramètres hydrogéologiques des argilites du callovo-oxfordien: perméabilité à l'eau et emmagasinement spécifique. Technical report, Andra report.

Delage, P., Menaceur, H., Tang, A. M., and Talandier, J. (2014). Suction effects in deep callovo-oxfordian claystone. *Géotechnique Letters*, 4(4):267–271.

Desbois, G., Höhne, N., Urai, J. L., Bésuelle, P., and Viggiani, G. (2017). Deformation in cemented mudrock (callovo-oxfordian clay) by microcracking, granular flow and phyllosilicate plasticity: insights from triaxial deformation, broad ion beam polishing and scanning electron microscopy. *Solid Earth*, 8(2):291.

Escoffier, S. (2002). *Caractérisation expérimentale du comportement hydromécanique des argilites de Meuse/Haute-Marne*. PhD thesis.

Eseme, E., Littke, R., and Krooss, B. (2006). Factors controlling the thermo-mechanical deformation of oil shales: Implications for compaction of mudstones and exploitation. *Marine and petroleum geology*, 23(7):715–734.

Fabre, G. and Pellet, F. (2006). Creep and time-dependent damage in argillaceous rocks. *International Journal of Rock Mechanics and Mining Sciences*, 43(6):950–960.

Fityus, S. and Buzzi, O. (2009). The place of expansive clays in the framework of unsaturated soil mechanics. *Applied Clay Science*, 43(2):150–155.

Gasc-Barbier, M., Chanchole, S., and Bérest, P. (2004). Creep behavior of bure clayey rock. *Applied Clay Science*, 26(1-4):449–458.

Giot, R., Auvray, C., Conil, N., and de La Vaissière, R. (2018). Multi-stage water permeability measurements on claystone by steady and transient flow methods. *Engineering Geology*, 247:27–37.

Guéry, A. A.-C., Cormery, F., Shao, J.-F., and Kondo, D. (2008). A micromechanical model of elastoplastic and damage behavior of a cohesive geomaterial. *International Journal of Solids and structures*, 45(5):1406–1429.

Han, B., Shen, W., Xie, S., and Shao, J.-F. (2019). Influence of pore pressure on plastic deformation and strength of limestone under compressive stress. *Acta Geotechnica*, 14(2):535–545.

Han, B., Xie, S., and Shao, J. (2016). Experimental investigation on mechanical behavior and permeability evolution of a porous limestone under compression. *Rock Mechanics and Rock Engineering*, 49(9):3425–3435.

Harrington, J. F., Cuss, R. J., and Talandier, J. (2017). Gas transport properties through intact and fractured callovo-oxfordian mudstones. *Geological Society, London, Special Publications*, 454(1):131–154.

Hassanzadegan, A., Blöcher, G., Zimmermann, G., and Milsch, H. (2012). Thermoporoelastic properties of flechtinger sandstone. *International Journal of Rock Mechanics and Mining Sciences*, 49:94–104.

Hellmann, R., Renders, P. J., Gratier, J.-P., and Guiguet, R. (2002). Experimental pressure solution compaction of chalk in aqueous solutions. part 1. deformation behavior and chemistry. *Water-rock interactions, ore deposits, and environmental geochemistry: A tribute to David A. Crerar*, 7:129–152.

Homand, F. (2000). Essais géomécaniques sondages est204 et est205. *Report ANDRA–LAEGO, N LG-FH. GFE. PSI. RPRE. 00.0145*.

Homand, F., Giraud, A., Escoffier, S., Koriche, A., and Hoxha, D. (2004). Permeability determination of a deep argillite in saturated and partially saturated conditions. *International Journal of Heat and Mass Transfer*, 47(14-16):3517–3531.

Homand, F., Shao, J.-F., Giraud, A., Auvray, C., and Hoxha, D. (2006). Pétrofabrique et propriétés mécaniques des argilites. *Comptes Rendus Geoscience*, 338(12-13):882–891.

Hoxha, D., Giraud, A., Homand, F., and Auvray, C. (2007). Saturated and unsaturated behaviour modelling of meuse–haute/marne argillite. *International Journal of Plasticity*, 23(5):733–766.

Hu, D., Zhang, F., Shao, J.-F., and Gatmiri, B. (2014). Influences of mineralogy and water content on the mechanical properties of argillite. *Rock mechanics and rock engineering*, 47(1):157–166.

Hu, D.-w., Zhou, H., Xie, S.-y., Zhang, K., Shao, J., and Feng, X. (2009). Study of biot's coefficients of marble during plastic deformation phase. *Rock Soil Mech*, 30(12):3727–3734.

Kherbouche, R., Shao, J., Skoczylas, F., and Henry, J. (1995). On the poroplastic behaviour of porous rocks. *EUROPEAN JOURNAL OF MECHANICS SERIES A SOLIDS*, 14:577–577.

Liu, T. (2016). *Étude expérimentale et interprétation micro-mécanique du comportement mécanique des argiles synthétiques*. PhD thesis, Lille 1.

Liu, Z., Shao, J., Liu, T., Xie, S., and Conil, N. (2016). Gas permeability evolution mechanism during creep of a low permeable claystone. *Applied Clay Science*, 129:47–53.

Liu, Z., Shao, J., Xie, S., and Conil, N. (2017). Triaxial creep induced gas permeability change and elastic modulus variation in callovo-oxfordian argillite. In *Poromechanics VI*, pages 1037–1044.

Liu, Z., Shao, J., Xie, S., Conil, N., and Talandier, J. (2019a). Mechanical behavior of claystone in lateral decompression test and thermal effect. *Rock Mechanics and Rock Engineering*, 52(2):321–334.

Liu, Z., Shao, J., Xie, S., Conil, N., and Zha, W. (2018a). Effects of relative humidity and mineral compositions on creep deformation and failure of a claystone under compression. *International Journal of Rock Mechanics and Mining Sciences*, 103:68–76.

Liu, Z., Shao, J., Xie, S., and Secq, J. (2015a). Gas permeability evolution of clayey rocks in process of compressive creep test. *Materials Letters*, 139:422–425.

Liu, Z., Xie, S., Shao, J., and Conil, N. (2018b). Multi-step triaxial compressive creep behaviour and induced gas permeability change of clay-rich rock. *Géotechnique*, 68(4):281–289.

Liu, Z., Xie, S., Shao, J.-F., and Conil, N. (2015b). Effects of deviatoric stress and structural anisotropy on compressive creep behavior of a clayey rock. *Applied Clay Science*, 114:491–496.

Liu, Z., Zhou, H., Zhang, W., Xie, S., and Shao, J. (2019b). A new experimental method for tensile property study of quartz sandstone under confining pressure. *International Journal of Rock Mechanics and Mining Sciences*, 123:104091.

Lydzba, D. and Shao, J. (2000). Study of poroelasticity material coefficients as response of microstructure. *Mechanics of Cohesive-frictional Materials: An International Journal on Experiments, Modelling and Computation of Materials and Structures*, 5(2):149–171.

Lydzba, D. and Shao, J.-F. (2002). Stress equivalence principle for saturated porous media. *Comptes Rendus Mecanique*, 330(4):297–303.

Masri, M., Sibai, M., Shao, J.-F., and Mainguy, M. (2014). Experimental investigation of the effect of temperature on the mechanical behavior of tournemire shale. *International Journal of Rock Mechanics and Mining Sciences*, 70:185–191.

Menaceur, H., Delage, P., Tang, A.-M., and Conil, N. (2015). The thermo-mechanical behaviour of the callovo-oxfordian claystone. *International Journal of Rock Mechanics and Mining Sciences*, 78:290–303.

Mohajerani, M., Delage, P., Monfared, M., Tang, A. M., Sulem, J., and Gatmiri, B. (2011). Oedometric compression and swelling behaviour of the callovo-oxfordian argillite. *International Journal of Rock Mechanics and Mining Sciences*, 48(4):606–615.

Mohajerani, M., Delage, P., Sulem, J., Monfared, M., Tang, A. M., and Gatmiri, B. (2012). A laboratory investigation of thermally induced pore pressures in the callovo-oxfordian claystone. *International Journal of Rock Mechanics and Mining Sciences*, 52:112–121.

Mohajerani, M., Delage, P., Sulem, J., Monfared, M., Tang, A. M., and Gatmiri, B. (2014). The thermal volume changes of the callovo–oxfordian claystone. *Rock mechanics and rock engineering*, 47(1):131–142.

Murphy, W., Reischer, A., and Hsu, K. (1993). Modulus decomposition of compressional and shear velocities in sand bodies. *Geophysics*, 58(2):227–239.

Nur, A. and Byerlee, J. (1971). An exact effective stress law for elastic deformation of rock with fluids. *Journal of geophysical research*, 76(26):6414–6419.

Robinet, J. (2008). *Minéralogie, porosité et diffusion dans l'argilite du Callovo-Oxfordien de Bure (Meuse/Haute-Marne, France) de l'échelle centimétriquea micrométrique*. PhD thesis, PhD thesis, Université de Poitiers, 2008.[Cited on page iii, 3, 4, 5, 153].

Robinet, J., Sardini, P., Siitari-Kauppi, M., Prêt, D., and Yven, B. (2015). Upscaling the porosity of the callovo-oxfordian mudstone from the pore scale to the formation scale; insights from the 3h-pmma autoradiography technique and sem bse imaging. *Sedimentary Geology*, 321:1–10.

Robinet, J.-C., Sardini, P., Coelho, D., Parneix, J.-C., Prêt, D., Sammartino, S., Boller, E., and Altmann, S. (2012). Effects of mineral distribution at mesoscopic scale on solute diffusion in a clay-rich rock: Example of the callovo-oxfordian mudstone (bure, france). *Water Resources Research*, 48(5).

Schroeder, C. (2007). Du coccolithe au réservoir pétrolier-approche phénoménologique du comportement mécanique de la craie en vue de sa modélisation à différentes échelles.

Shao, J. (1998). Poroelastic behaviour of brittle rock materials with anisotropic damage. *Mechanics of materials*, 30(1):41–53.

Shao, J.-F., Ata, N., and Ozanam, O. (2005). Study of desaturation and resaturation in brittle rock with anisotropic damage. *Engineering geology*, 81(3):341–352.

Shi, H., Hosdez, J., Rougelot, T., Xie, S., Shao, J., Talandier, J., and Lacidogna, G. (2020). Digital volume correlation applied to x-ray micro-tomography images in uniaxial creep tests on anisotropic clayey rock. *Applied Sciences*, 10(14):4898.

Sibai, M. (1990). *Étude de l'interaction fluide-squelette dans les roches: méthodes expérimentales et modélisation*. PhD thesis, Lille 1.

Skempton, A. (1954). The pore-pressure coefficients a and b: Geotechnique. *Institutions of Civil Engineers, Great Britain*, 4:143–147.

Skempton, A. (1984). Effective stress in soils, concrete and rocks. *Selected papers on soil mechanics*, 1032:4–16.

Soe, A. K. K., Osada, M., and Win, T. T. N. (2010). Drying-induced deformation behaviour of shirahama sandstone in no loading regime. *Engineering geology*, 114(3-4):423–432.

Song, Y., Davy, C. A., and Troadec, D. (2016). Gas breakthrough pressure (gbp) through claystones: correlation with fib/sem imaging of the pore volume. *Oil & Gas Science and Technology–Revue d'IFP Energies nouvelles*, 71(4):51.

Tennis, P. D. and Jennings, H. M. (2000). A model for two types of calcium silicate hydrate in the microstructure of portland cement pastes. *Cement and concrete research*, 30(6):855–863.

Vales, F., Berest, P., and Gharbi, H. (2002). Interaction between creep, swelling and pressure-solution during indentation tests.

Valès, F., Minh, D. N., Gharbi, H., and Rejeb, A. (2004). Experimental study of the influence of the degree of saturation on physical and mechanical properties in tournemire shale (france). *Applied Clay Science*, 26(1-4):197–207.

Vincké, O., Longuemare, P., Boutéca, M., Deflandre, J., et al. (1998). Investigation of the poromechanical behavior of shales in the elastic domain. In *SPE/ISRM Rock Mechanics in Petroleum Engineering*. Society of Petroleum Engineers.

Voinis, S., Gago, J., and Muller, W. (1992). Modelling of gas generation (pegasus project). In *Proc. Prog. Meeting of Pegasus Project, CEC, preprint volume, Brussels*, volume 11, page 12.

Wileveau, Y., Cornet, F., Desroches, J., and Blumling, P. (2007a). Complete in situ stress determination in an argillite sedimentary formation. *Physics and Chemistry of the Earth, Parts A/B/C*, 32(8-14):866–878.

Wileveau, Y., Su, K., and Ghoreychi, M. (2007b). A heating experiment in the argillites in the meuse/haute-marne underground research laboratory. In *International Conference on Radioactive Waste Management and Environmental Remediation*, volume 43390, pages 939–944.

Xie, S. and Shao, J.-F. (2006). Elastoplastic deformation of a porous rock and water interaction. *International Journal of Plasticity*, 22(12):2195–2225.

Yang, D., Billiotte, J., and Su, K. (2010). Characterization of the hydromechanical behavior of argillaceous rocks with effective gas permeability under deviatoric stress. *Engineering Geology*, 114(3-4):116–122.

Yang, D., Bornert, M., Chanchole, S., Wang, L., Valli, P., and Gatmiri, B. (2011). Experimental investigation of the delayed behavior of unsaturated argillaceous rocks by means of digital image correlation techniques. *Applied clay science*, 54(1):53–62.

Yang, H., Xie, S.-y., Secq, J., and Shao, J.-f. (2017). Experimental study and modeling of hydromechanical behavior of concrete fracture. *Water Science and Engineering*, 10(2):97–106.

Yuan, H., Agostini, F., Duan, Z., Skoczylas, F., and Talandier, J. (2017). Measurement of biot's coefficient for cox argillite using gas pressure technique. *International Journal of Rock Mechanics and Mining Sciences*, 92:72–80.

Yven, B., Sammartino, S., Geraud, Y., Homand, F., and Villieras, F. (2007). Mineralogy, texture and porosity of callovo-oxfordian argillites of the meuse/haute-marne region (eastern paris basin). *Mémoires de la Société géologique de France*, 178(1):73–90.

Zhang, C. and Rothfuchs, T. (2004). Experimental study of the hydro-mechanical behaviour of the callovo-oxfordian argillite. *Applied Clay Science*, 26(1-4):325–336.

Zhang, C.-L. (2013). Sealing of fractures in claystone. *Journal of Rock Mechanics and Geotechnical Engineering*, 5(3):214–220.

Zhang, C.-L., Conil, N., and Armand, G. (2017). Thermal effects on clay rocks for deep disposal of high-level radioactive waste. *Journal of Rock Mechanics and Geotechnical Engineering*, 9(3):463–478.

Zhang, C.-L. and Rothfuchs, T. (2007). Experimental study on self-sealing capacity of clay rocks. *Clays in Natural & Engineered Barriers for Radiactive Waste Confinement. ANDRA, Lille*, pages 539–540.

Zhang, C.-L. and Rothfuchs, T. (2008). Damage and sealing of clay rocks detected by measurements of gas permeability. *Physics and Chemistry of the Earth, Parts A/B/C*, 33:S363–S373.

Zhang, F. (2011). *Comportement mécanique des argilites de MHM: influences de la saturation, de la composition minéralogique et de la température*. PhD thesis, Lille 1.

Zhang, F., Hu, D., Xie, S., and Shao, J.-F. (2014a). Influences of temperature and water content on mechanical property of argillite. *European journal of environmental and civil engineering*, 18(2):173–189.

Zhang, F., Shao, J. F., et al. (2014b). Experimental study of poromechanical behavior of saturated claystone under triaxial compression. *Acta Geotechnica*, 9(2):207–214.

Zhang, F., Xie, S., Hu, D., Shao, J.-F., and Gatmiri, B. (2012). Effect of water content and structural anisotropy on mechanical property of claystone. *Applied Clay Science*, 69:79–86.